CREATION AND ANALYSIS OF A HIGH RESOLUTION DIGITAL ELEVATION MODEL OF NORTHERN CHILE

by Jennifer S-ih Yu

The thesis/dissertation document has been electronically approved by the following individuals:

Bryan Isacks (Chairperson)

Matthew Pritchard (Minor Member)

Richard Allmendinger (Minor Member)

Donald Campbell (Minor Member)

CREATION AND ANALYSIS OF A HIGH RESOLUTION DIGITAL ELEVATION MODEL OF NORTHERN CHILE

A Dissertation

Presented to the Faculty of the Graduate School

of Cornell University

In Partial Fulfillment of the Requirements for the Degree of

Doctor of Philosophy

by

Jennifer S-ih Yu

August 2010

© 2010 Jennifer S-ih Yu

CREATION AND ANALYSIS OF A HIGH RESOLUTION DIGITAL ELEVATION MODEL OF NORTHERN CHILE

Jennifer S-ih Yu, Ph. D.
Cornell University 2010

This dissertation presents a digital elevation model (DEM) of the north Chilean forearc derived from interferometric synthetic aperture radar (INSAR). The DEM spans the Andean forearc from 18º S to 26º S latitude and is 99.1% complete. The coherence over the dataset is good to excellent, largely because of the ideal hyper-arid climate of the region for repeat-pass INSAR processing. The horizontal resolution of the data is 20 meters and the vertical resolution is 2-3 meters with an absolute vertical accuracy of 32 meters. We analyze a composite DEM from our 20-meter DEM and the 90-meter Cornell digital topography to create a fault scarp map based on scarps with youthful-looking profiles to examine Cenozoic faulting patterns in the forearc. Two fault patterns are evident in the fault map: 1) dominant N-S trending fault scarps controlled by pre-existing structures of the Atacama Fault System (AFS) south of 21º S and 2) a spatially-limited distribution of E-W trending fault scarps between 19º S and 21.5º S. We consider several regional factors that could be responsible for the E-W faults: climate, the AFS, aseismic ridge subduction, proximity to the Bolivian Orocline, and segment boundaries at the Nazca-South America subduction interface. We conclude that the influence of oroclinal bending and a possible asperity on the plate interface acting as a segment boundary could explain the presence and containment of these

anomalous structures. Finally, we validate the DEM with field-measured scarp profiles and find agreement to within the vertical errors of the DEM. Applying inverse scarp diffusion modeling to both field and DEM profiles, we are able to quantitatively identify two populations of scarp morphologies that correspond to proximity to the coast. Scarps closer to the coast have a steeper scarp face than those further inland. We hypothesize that coastal fog creates an erosion-resistant gypcrete layer from the colluvium, which preserves fault scarp faces against diffusion, thus maintaining a younger morphology. These studies demonstrate a range of applications made possible by an accurate, high resolution, wide coverage digital dataset derived from INSAR.

BIOGRAPHICAL SKETCH

Born in Hampton, Virginia on September 23, 1971, Jennifer S-ih Yu was destined for math camp while other girls in the Tidewater area passed their summers at field hockey camp. Math camp led to a sophomore year at the Thomas Jefferson High School for Science and Technology in Alexandria during the family's one year stint in northern Virginia. For the next two years, Jennifer straddled coursework at the local high school and the College of William and Mary in Williamsburg. In 1989, she graduated from Lafayette High School, packed two suitcases, and flew west to the California Institute of Technology (Caltech) to drink from the fire hose of knowledge. There she met a shy, kind, and bright young man who would become her life partner, Jeremy Darling. Upon earning a B.S. in Engineering and Applied Science in 1993, Jennifer went to work for NASA Jet Propulsion Laboratory in Pasadena, California. In 1996, Jennifer and Jeremy moved to Ithaca, New York where they both entered graduate programs at Cornell University.

Jennifer returned to Pasadena with Jeremy in 2002 where she took a remote sensing and geographical information system position with the Department of Geological and Planetary Sciences at her alma mater. In 2005, a year following the tragic death of her only sibling, Jennifer and Jeremy decided to settle in the Colorado Rockies. Jennifer spent a year working at UNAVCO, Inc. in Boulder, Colorado before returning to Ithaca and defending her dissertation in May 2007. After her cancer diagnosis in late 2007 and subsequent treatment, Jennifer made a career change and has now completed her dissertation.

“Hay rutas!”

-- Gregory D. Hoke

ACKNOWLEDGMENTS

I have a long list of people I must thank for their support during my graduate school years in Snee and beyond. Please do not mistake my brevity for lack of gratitude.

First, I want to thank Bryan Isacks, my advisor. Bryan is the epitome of scientific curiosity and it was my privilege to witness his enthusiasm for science and the greater questions of the world. My thanks to Rick Allmendinger for countless hours of his time and for making my field season in Chile a reality; to Kerry Cook – a role model and friend; to Don Campbell for the astronomer's (witty) perspective. I can never thank Matt Pritchard enough for his unwavering support and encouragement. Matt was instrumental in seeing this dissertation to completion.

I am grateful to fellow graduate students Gregory Hoke, Paco Gomez, and Ben Brooks for teaching me the ways of geomorphology, field work, and remote sensing. Special thanks go to Terry Jordan who rarely had time, but always set some aside to offer her wisdom and guidance; to Arthur Bloom who gave me a semester of geomorphology in exchange for a sushi lunch; and to Muawia Barazangi for keeping all of us in line.

I am indebted to Steve Gallow for his maintenance of our computers and networks to meet our demanding needs. You will never find a more kind and patient individual.

Many thanks to these fine people for their contributions to my research: Joan Ramage, Andrew Klein, Sarah Das, Larry Smith, Chris Duncan, Jeff Masek, Kirk Evans, Doug Alsdorf, Charlie Werner, Karen Frey, Eric Fielding, Ian Joughin, Gabriel Gonzalez, Cocho Mpodozis, Andy Tomlinson, Nicholas Blanco, Moyra Gardeweg, Alejandro Macci, Daniel Carrizo, Paula Cornejo, Art Bloom, Ramon Arrowsmith, Tom Hanks, Sue Kay, John Gephart, Nestor Cardozo, Mike Bevis, Bob Smalley, Rebecca Knight, Matt Patrick, Chris Harig, Jonathan Barton, Joe Aliperti, Adrian Hovey, Claire Burns (formerly McCorkle), Aaron Wade, Dogan Seber, Christine Sandvol (formerly Orgren), Carrie Brindisi, Dan Danowski, Dave Steer, Muawia Barazangi, Larry Brown, and Jack Loveless.

Thank you to all Snee faculty and staff for their kindness, help, love, and practical jokes throughout the many years.

Friends provide the moral support for and sometimes the diversion from the task at hand, but they make life rich. From the bottom of my heart, I thank: Joan Ramage, Mom and Dad Ramage, Sande and the late Roger Burr, Claire and Matt Burns, Carrie Brindisi and Mike Plotkin, Matt Pritchard and Rowena Lohman, Art and Donna Bloom, Bryan Isacks and Marjorie Olds, Rick Allmendinger and Terry Jordan and Carrie Allmendinger, Muawia and Nimat Barazangi, Kerry Cook and her family, Martha Haynes and Riccardo Giovanelli, Don Campbell, Phil Nicholson, Don Banfield, Julie Rathbun and Tyler Nordgren, George Hade, Ben Brooks, Mary Parke, Paco Gomez, Sarah Das, Matt Evans, Karen Frey, Greg Hoke, Graham Brew, Alex Calvert, Alex Erendi, Chris Achong, Pat Carr, Megan Herz, Dan Danowski, Karen Fisher,

Bruce Monger, Amy Kwiatkowski, Nate Fisher, Ali Al-Lazki, Khaled Al-Damegh, Cocho Mpodozis and his beautiful family, Gabriel Gonzalez, Alejandro Macci, Andy Tomlinson, Jack Prater, Melinda and Aaron Kiely, Elisabeth Nadin, Samantha Daly, Nicole Smith Downey, Mark Simons, Joann Stock, Ken Farley and so many others.

Special thanks to Marjorie Olds, who shows us all that no project is too large or too small for our attentions. She lends heart and spirit to a world in need of both.

Xie-xie to my parents, the Darlings, Elena Yang and David Thorn, my maternal grandmother, and my late sister and best friend Kristin Yu. An extra dog treat goes to my beloved Kaweah who provided companionship and comfort in the darkest hours.

Finally, I want to acknowledge the one person who has stood by my side through all of my agonies as well as my joys. There is no better man than you, Jeremy Darling.

This research was funded by NASA grants NAG5-11424, NAG5-30126, NAGW-2638, NGT5-30126, NAG5-11424 and NSF grants EAR-9706427 and EAR-0087431.

TABLE OF CONTENTS

LIST OF FIGURES

LIST OF TABLES

CHAPTER 1

INTRODUCTION

Convergence over millions of years as the Nazca plate subducted beneath the South American plate has resulted in great earthquakes, explosive volcanic eruptions, and the rise of the Andes – the second highest mountain range in the world. The morphology of this long north-south trending range mimics the shape of South America's west coast. The convergent margin of the central Andes provides a unique laboratory for tectonic studies. The striking parallelism of the trench, the coast, the volcanism and the Andean plateau, has inspired researchers to ask how these features have come to be in this setting. Understanding these fundamental processes gives us greater insight into the dynamic processes shaping the Earth.

The work in this dissertation focuses on the central Andean forearc of northern Chile. On the surface, we see a complex and intriguing pattern of faulting that is intimately tied to the equally intriguing morphology. At depth, this part of the South American plate contacts the Nazca plate at the subduction interface. Subduction processes play a primary role in the deformation and evolution of the forearc and surrounding environment. Crustal faults archive past and ongoing activity of the earthquake cycle, which is driven by subduction. The record is a long one, thanks to a climate that has preserved landforms for millions of years.

A complete story of the forearc's Cenozoic deformation history has yet to be synthesized. Interest in understanding the evolution of the region has

increased over the past several decades. Researchers have approached studies in the forearc from a broad spectrum of disciplines at scales ranging from microscopic to continental. Some of the outstanding questions include: What is the relationship between subduction and faulting in the forearc? What is the overall history of faulting in the forearc? What is responsible for the uplift and formation of the Coastal Cordillera?

1.1 *Tectonic Setting of the Coastal Cordillera of Northern Chile*

The Coastal Cordillera of the Central Andes trends north-south along the western edge of northern Chile, parallel to the Peru-Chile trench which lies approximately 100 km offshore to the west. The Longitudinal Valley (Pampa del Tamarugal) borders the eastern boundary of the Cordillera and transitions into the western flanks of the Central Andean plateau. The modern convergence rate of the subducting Nazca plate with respect to the overriding South American plate is ~ 65 mm/a with a direction of N80E (Kendrick et al., 2003). The dip of the subducting plate in this region is 30° down to the east (Cahill and Isacks, 1992), part of the Andean steep-slab subduction, although in the interplate seismic zone, the dip is closer to 20º (Buske et al., 2002). Toward the southern end of the Coastal Cordillera, the dip of the slab begins to flatten. The two plates are seismically coupled to between a depth of 20-50 km (Tichelaar and Ruff, 1991) due to the strong frictional resistance exerted on the Nazca plate at the subduction interface (Ruff and Kanamori, 1980). Great interplate thrust earthquakes periodically rupture segments of this plate boundary, resulting in permanent deformation in the coastal region of the upper plate in the form of coseismic cracks and ground displacement. The

two most recent events with Mw=8.4 off of southern Peru in 2001 and the Mw=8.0 in northern Chile in 1995, spatially bracket a region known as the Arica seismic gap which hasn't had a major event since 1877 and 1869 (both estimated to be Mw=9.0). Based on recurrence intervals of 90-120 years (Comte and Pardo, 1991), this segment is considered overdue for a significant seismic event.

Strongly coupled plates in a convergent setting commonly exhibit evidence of subduction erosion. Rutland (1971) estimated the continental margin of South America has lost ~200 km of forearc material to subduction erosion processes based on differences in distance between the current Andean magmatic arc to the trench (~300 km) and the distance from the Jurassic magmatic arc (today's Coastal Cordillera) to the modern trench (~100 km). Scheuber and Reutter (1992) summarize the eastward migration of the magmatic arc through four phases beginning with the Jurassic-Early Cretaceous position, where today's Coastal Cordillera stands, up to the Neogene-Present Western Cordillera at the edge of the modern Andean plateau. The Coastal Cordillera has experienced uplift and east-west extension since the mid-Miocene (Niemeyer et al., 1996). Normal faults exist near the Mejillones Peninsula and to a lesser extent around the Salar Grande (Neimeyer et al., 1996; Armijo and Thiele, 1990; Gonzàlez et al., 2003). Subduction erosion is believed to cause uplift in the forearc through underplating at the base of the upper plate (Armijo and Thiele, 1990; Delouis et al. 1998, Fig. 32c). In contrast, to the north of the Coastal Cordillera, basal erosion of the upper plate off the coast of Arica has resulted in subsidence (von Huene and Lallemand, 1990).

Nearly normal convergence of the Nazca plate with respect to the northern Chile margin has endured since 49.5 Ma (Pardo-Casas and Molnar, 1987). The most recent episode of rapid convergence (> 100 mm/a) in the early Miocene and an earlier episode ~40 Ma (Elger et al., 2005) formed the modern Andes through crustal shortening and thickening.

1.2 *Morphology*

The Coastal Cordillera averages 40 km in width and 1000 meters in elevation with the highest peaks topping 2500 meters over a subdued relief. To the east, the Longitudinal Valley parallels the range, collecting sediments off of the Andes. The Coastal Cordillera extends from 18° 30′ S to 25° S where it runs into an anomalous topographic high that closes the southern end of the Longitudinal Valley (Figure 1.1). South of this high, the topography of the coastal range becomes indistinguishable from the western slopes ramping down from the Andes. For the purposes of this study, we include the coast down to 30° S as part of the Coastal Cordillera. At the northern end of the Coastal Cordillera, the range tapers and diminishes in elevation until it disappears at Arica (~18° 30′ S). It continues offshore as a submarine bench on the continental shelf having been subsided an estimated 4-5 km since 20 Ma (von Huene and Lallemand, 1990). The northern end of the Longitudinal Valley is pinched out at 19° 30′ S, overtaken by the flanks of the Altiplano leading down to the Pacific. Li (1995) describes the bathymetry of the Nazca Plate around the Arica Bight – Iquique area as a NE-SW trending low point up to 1000 meters deeper than surrounding areas. The corresponding

Figure 1.1 Overview of the Central Andean margin and study area. Bathymetry (ETOPO5) and topography (GTOPO30) emphasize the parallelism of the major geomorphic features (from west to east): the trench, Coastal Cordillera, Central Depression and Altiplano-Puna plateau.

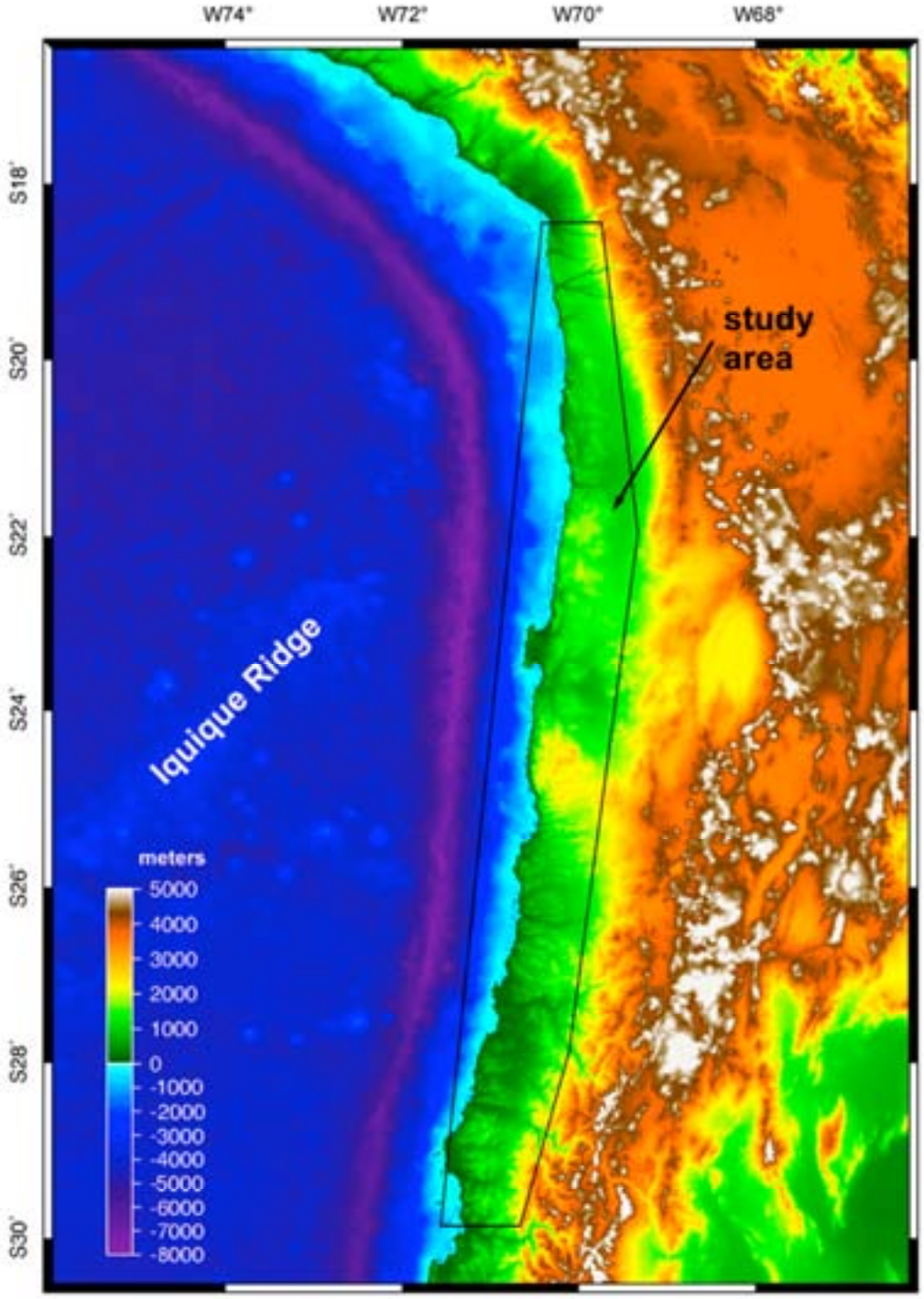
W74°
W72°
W70°
W68°
S18°
S20°
S22°
S24°
S26°
S28°
S30°
study
area
Iquique Ridge
meters
5000
4000
3000
2000
1000
0
-1000
-2000
-3000
-4000
-5000
-6000
-7000
-8000

continental shelf and onshore forearc show drainages and channels that radially converge toward the trench.

The two most prominent features within the Coastal Cordillera are the Coastal Scarp (Cantilado) and the Atacama Fault System. The Coastal Scarp delimits the western boundary of the Coastal Cordillera in the form of a remarkable high angle cliff. It averages 1000 meters in height above the littoral and peaks near Tocopilla (22° S) at 1600 meters. Although the Coastal Scarp has been described as an extensive extensional fault scarp (Armijo and Thiele, 1990), field work (Hartley and Jolley, 1995) supports Miocene-Pliocene uplift of the coast and retreat of the coastal escarpment. The Atacama Fault System (AFS) strikes parallel to and lies within the Coastal Cordillera and extends for over 1000 kilometers from 21°S (Iquique) to 30°S (La Serena). Three main arcuate segments comprise this originally left-lateral strike-slip fault system, from north to south: Salar del Carmen, Paposo, and El Salado (Figure 1.2). Block faulting and localized reactivation of the AFS have dominated the landscape morphology north of 25° S since the end of the Paleogene (Mortimer, 1980; Randall et al., 1996; Delouis et al., 1998; González et al., 2006). To the south of 25° S, the influence of climate in the morphology increases as evidenced by more frequent drainages across the coast range to the ocean. Two of the most anomalous features occur at the latitude of 23° 30′ S: the Mejillones Peninsula, an anvil shaped deviation in the otherwise

Figure 1.2 Map of the Atacama Fault System (AFS) in northern Chile. After Brown et al., 1993.

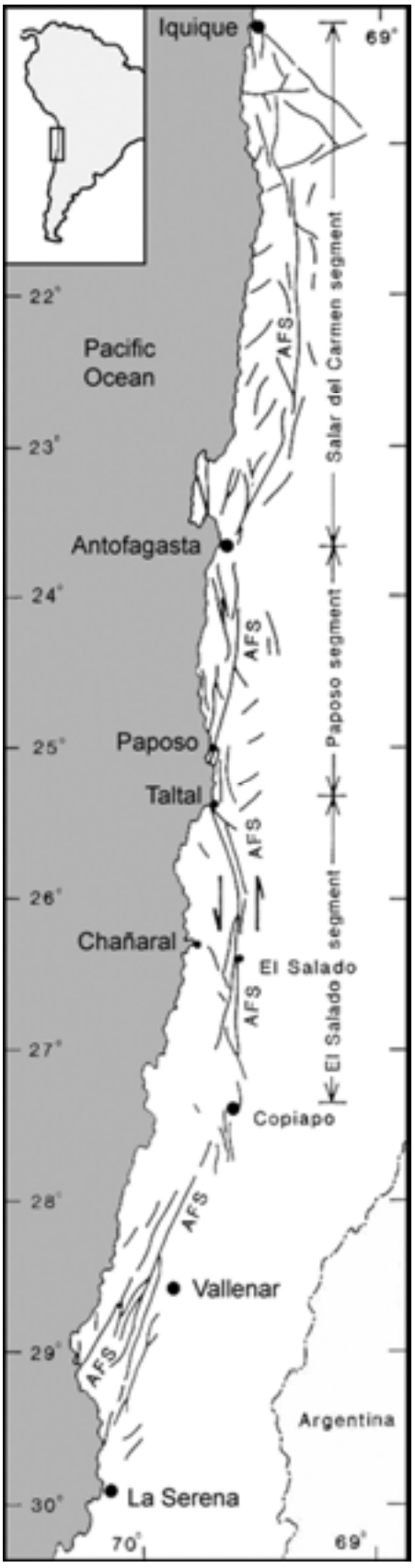
Iquique
69°
22°
Pacific
Ocean
AFS
Salar del Carmen segment
23°
Antofagasta
24°
AFS
Paposo segment
25°
Paposo
Taltal
AFS
26°
Chañaral
El Salado
AFS
El Salado segment
27°
Copiapo
28°
AFS
Vallenar
29°
AFS
Argentina
30°
La Serena
70°
69°

linear coastline, and further inland, the Salar de Atacama, a large basin interrupting the Western Cordillera. The magmatic arc skirts the eastern boundary of the Salar de Atacama.

1.3 *Convergence, Uplift, and Faulting History*

The Coastal Cordillera has a complex history dating back to the late Jurassic-early Cretaceous when the Mesozoic magmatic arc occupied the present position of the Coastal Cordillera. The magmatic arc was abandoned in the mid-Cretaceous (Brown et al., 1993), migrating eastward to the position of the Central Depression. The Coast Range is predominantly Jurassic - early Cretaceous volcanic rock. Episodes of fast convergence (greater than 100 mm/a) may correlate with uplift, and slower convergence with peneplanation. Pardo-Casas and Molnar (1987) determined there was rapid convergence for the early Eocene between 50 and 42 Ma. Denudation surfaces, formed in the Oligocene-early Miocene, correspond to a period of reduced convergence rates and tectonic quiescence. There are two surfaces in the north of our study area: the Tarapaca Pediplain, which lies beneath lower Miocene deposits (Mortimer, 1974; Mortimer and Saric, 1975), and the Choja Pediplain (Galli-Olivier, 1967), which lies under the eastern portion of the Pampa del Tamarugal.

The convergence rate increased since 26 Ma (Pardo-Casas and Molnar, 1987). By the end of the Oligocene, the Coastal Cordillera experienced uplift relative to the Pampa del Tamarugal to the east (Mortimer and Saric, 1972), resulting in faulting of the pediplain. In northern Chile between 19° S and 20°

30′ S, Mortimer et al. (1974) based the timing of uplift on the dates of the Rhyolite formation (K-Ar ages: 16 and 21 Ma), which lies across the Longitudinal Valley and the Coastal Cordillera, and the Andesite formation (K-Ar ages: 9 Ma) which only exists in the Pampa del Tamarugal. They infer that the uplift of the Coastal Cordillera first blocked the valley during the Oligocene-Miocene boundary based on the age of sediments in the Pampa del Tamarugal.

Faulting in the Coastal Cordillera started before the Pliocene formation of the marine terraces along the coast due to coastal recession (Mortimer and Saric, 1975). As the convergence rate decreased by half since 15 Ma (Kendrick et al., 2003) another erosional episode took place in the late Miocene to early Pliocene (González et al., 2003). This time period corresponds to the Atacama Pediplain, which ceased to develop at the end of the Miocene in the southern Atacama Desert (Mortimer, 1973; Dunai et al., 2005; Carrizo et al., 2006). The modern topography is a result of more than 1 km of uplift in the Coastal Cordillera since the late Miocene (Armijo and Thiele, 1990; Hoke et al., 2007).

1.4 *The Atacama Fault System*

The Atacama Fault System (AFS) developed as a north-south trending intra-arc shear zone in the Mesozoic magmatic arc during the late Jurrasic (Brown et al., 1993). Oblique convergence at the plate boundary resulted in partitioning of strain into two components: margin-parallel and margin-normal. During this time, the AFS was a major sinistral strike-slip system in a sinistral

transtensional setting to accommodate the deformation (Scheuber and Reutter, 1992; McCaffrey, 1996; Scheuber and González, 1999). Arabasz (1971) estimated lateral displacements on the order of tens of kilometers along the AFS and Hervé (1987b) later measured 34 km of sinistral displacement along the Izcuña fault system dated between 131 and 144 Ma. Pardo-Casas and Molnar (1987) reported the arc normal component of deformation changed from extensional in the Jurassic to early Cretaceous to compressional after a significant change in the convergence vector due to a tectonic reorganization. All major activity on the AFS occurred during the Late Mesozoic. Only minor localized reactivations have taken place since. The AFS has not been considered an active strike-slip system in the Cenozoic (Hervé 1987a; Armijo and Thiele, 1990).

The majority of Cenozoic fault activity on the AFS involves normal faulting (Arabasz, 1971; Okada, 1971; Armijo and Thiele, 1990; Neimeyer et al., 1996; Delouis et al., 1998; González et al., 2003), reflecting that the Coastal Cordillera has been under arc-normal extension since 50 Ma. The displacements have magnitudes considerably less than the motions in the Mesozoic and are typically reactivations of the pre-existing AFS structure. Several researchers conducted local field investigations along the AFS in search of evidence for Neogene to Recent tectonic activity. These studies are categorized by segments from south to north: the El Salado, the Paposo, and the Salar del Carmen (Figure 1.2).

On the El Salado segment of the southern AFS, late Miocene normal displacements exist near Taltal (Arabasz, 1971; Cooke and Mortimer, 1971;

Naranjo, 1987). Riquelme et al. (2003) give geomorphological evidence for normal faulting roughly between 10-18 Ma, when the AFS cut off a drainage valley. The NW trending Taltal fault offsets the AFS left-laterally by 10 km (Arabasz 1971).

Miocene normal reactivation of the Paposo segment (23° 30′ to 25° 30′ S) has been documented by Hervé (1987a) who constrained fault motion between 19 and 5.5 Ma based on the age of a pyroclastic flow on both sides of the fault and an ash deposit within an alluvial fan produced by the scarp. The southern end of the fault is truncated by the coastal cliff, which developed before the upper Miocene (Naranjo, 1987). After the 1995 Antofagasta (Mw=8.0) earthquake, Delouis et al. (1998) observed fresh breaks (up to 20 cm) in an alluvial surface along the Paposo segment. Other researchers were unable to find these scarps in 2005 and 2006, although they did find a prominent scarp along part of the Paposo segment across which older alluvial fan segments are offset (Allmendinger, pers. comm. 2007).

The largest and northernmost part of the AFS is the Salar del Carmen segment, stretching from Iquique (20° S) to Antofagasta (23° 30′ S). Similar to the two southern sections of the AFS, this segment experienced vertical motions in the Miocene (Delouis et al., 1998). At the southern end, researchers have found evidence for Pliocene to Pliestocene normal faulting in several locations along the Mejillones Peninsula (Arabasz, 1971; Okada, 1971; Armijo and Thiele, 1990, González et al., 2003; González et al., 2006), which is not technically part of the AFS, and near the Salar del Carmen (Armijo and Thiele, 1990; Naranjo, 1987; González et al., 2003). Field work

conducted after the 1995 Antofagasta rupture revealed fresh vertical offsets on the order 20 cm (Delouis et al., 1997; Delouis et al., 1998; Klotz, 1999). Near its northern onshore terminus at the Salar Grande, the AFS trends from north-south into a north-northwest – south-southeast direction across the salar. González et al. (1997) identified three sets of faults in this region based on trend: N-S, NW-SE, and E-W and concluded that the E-W faults were normal, the oldest, and pre-dated the Pliocene. Subsequent work by Allmendinger et al. (2005) found these and other E-W faults to the north to be reverse and that much of the deformation occurred before the middle Pliocene. Dextral motions on the Salar Grande fault are estimated to be Pliocene-Quaternary in age (González et al., 2003). Very recent activity in the form of ground ruptures in alluvium have been identified by Reijs and McClay (1998) and have been given more thorough treatment in Loveless et al. (2005).

1.5 *Climate*

From Arica (18° 30′ S) to La Serena (30° S), the Coastal Cordillera lies completely within the Atacama Desert, which is the driest in the world (Fuenzalida, 1966). Three natural phenomena combine to create these hyper-arid conditions along the north Chilean coast. The Peruvian current is a north-flowing ocean current with cold waters and cool air temperatures that inhibit coastal precipitation, creating arid conditions. The persistent high pressure at the southern end of the Hadley circulation aids in maintaining the desert climate. Any moisture traveling from the Amazon Basin must cross two high orographic fronts: the Eastern and Western Cordilleras that bound the Andean plateau. The Eastern Cordillera forces out most of the moisture in the form of

precipitation and what little remains may fall on the upper western slopes of the Altiplano, but rarely below 3500 m (Hoke et al., 2004). The combination of the cold ocean current and the high pressure region results in fog along the coast that occasionally penetrates inland, delivering limited moisture to the surface.

The first-order geomorphology of the Coastal Cordillera suggests a change in climate along-strike. The Atacama Desert exerts the greatest influence in the north (18° S to 25° S) and is largely responsible for the excellent preservation of late Cenozoic fault scarps due to extremely low erosion rates. Mean annual precipitation is less than 50 mm per year increasing southward to less than 250 mm around 31°S (Miller, 1976) because of the increasing intensity of the westerlies. Lack of sediment accumulation in the Peru-Chile trench corresponds to the driest parts of the forearc. As precipitation levels increase to the south, the forearc delivers more sediment to the trench. Current hyper-arid conditions in the Atacama Desert have persisted at the very least, since the Pliocene (Hartley and Chong, 2002), although other studies support a longer duration since 10 Ma (Hoke et al., 2004) and 14 Ma (Alpers and Brimhall, 1998). Evidence for periods of increased precipitation exists in terrestrial records (LaTorre et al., 2002; Rech et al., 2002), but the overall climate was still considered arid.

1.6 *Overview*

This dissertation examines a DEM of the north Chilean forearc to better understand how subduction and surface processes influence the observed morphology of the region. Chapter 2 reviews DEM generation from raw SAR scenes to the final dataset, including INSAR processing, ground-truthing, and mosaicking. We assess the quality of the DEM and describe artifacts and sources of error in the data.

In Chapter 3, we create a fault map based on our examination of the DEM and identify faulting patterns in the forearc. Certain patterns raise questions about the evolution of the region. We explore potential factors that could explain the presence of the anomalous faulting.

Chapter 4 compares scarp profile measurements from the field with profile measurements in the DEM to quantify the validity of the DEM for scarp profile analysis. We apply an inverse diffusion model to a sampling of scarp profiles to quantitatively characterize scarp morphology and determine if the method can identify different populations among the scarps in the forearc.

REFERENCES

Allmendinger, R. W., González, G., Yu, J., Hoke, G., Isacks, B., 2005, Trench-parallel shortening in the Northern Chilean Forearc: Tectonic and climatic implications, Geological Society of America Bulletin, 117, 89-104.

Alpers, C. N., and Brimhall. G. H., 1988, Middle Miocene climatic change in the Atacama Desert, northern Chile: Evidence from supergene mineralization at La Escondida, Geological Society of America Bulletin, 100, 1640-1656.

Arabasz, W. J., Jr., 1971, Geological and geophysical studies of the Atacama fault zone in northern Chile, Ph.D. thesis, California Institute of Technology, Pasadena, California, pp. 275.

Armijo, R., and Thiele, R., 1990, Active faulting in northern Chile: ramp stacking and lateral decoupling along a subduction plate boundary? Earth and Planetary Science Letters, 98, 40-61.

Brown, M., Diáz, F., and Grocott, J., 1993, Displacement history of the Atacama fault system 25° S - 27° S, northern Chile, Geological Society of America Bulletin, 105, 1165-1174.

Buske, S., Lüth, S., Meyer, H., Patzig, R., Reichert, C., Shapiro, S., Wigger, P., Yoon, M., 2002, Broad depth range seismic imaging of the subducted Nazca Slab, North Chile, Tectonophysics, 350, 273-282.

Cahill, T., and Isacks, B., 1992, Seismicity and shape of the subducted Nazca plate, Journal of Geophysical Research, 97, 17,503-517,529.

Carrizo, D., et al., 2006, Relación entre los cambios climáticos globales post-24ma y el proceso de desecación del desierto de atacama., XI Congreso Geológico Chileno Actas 2, 171-174.

Comte, D., and Pardo, M., 1991, Reappraisal of great historical earthquakes in the northern Chile and southern Peru seismic gaps, Natural Hazards, 4, 23-44.

Cooke, R., and Mortimer, C., 1971, Geomorphological Evidence of Faulting in the Southern Atacama Desert, Chile, Revue de Geomorphologie Dynamique, 20, 71-78.

Delouis, B., Monfret, T., Dorbath, L., Pardo, M., Rivera, L., Comte, D., Haessler, H., Caminade, J. P., Ponce, L., Kausel, E., Cisternas, A., 1997, The Mw=8.0 Antofagasta (northern Chile) earthquake of 30 July 1995: A precursor to the end of the large 1877 gap, Bulletin of the Seismological Society of America, 87, 427-445.

Delouis, B., Philip, H., Dorbath, L., Cisternas, A., 1998, Recent crustal deformation in the Antofagasta region (northern Chile) and the subduction process, Geophysical Journal International, 132, 302-338.

Dewey, J. F., and Lamb, S. H., 1992, Active Tectonics of the Andes, Tectonophysics, 205, 79-95.

Dunai, T. J., González López, G. A., Juez-Larré, J., 2005, Oligocene–Miocene age of aridity in the Atacama Desert revealed by exposure dating of erosion-sensitive landforms, Geology, 33, 321-324.

Elger, K., Oncken, O., and Glodny, J., 2005, Plateau-style accumulation of deformation: Southern Altiplano., Tectonics, 24, doi:10.1029/2004TC001675.

Fuenzalida, H., 1966, Clima, in Geografía económica de Chile., edited, pp. 98-152, CORFO, Santiago.

Galli-Olivier, C., 1967, Pediplain in Northern Chile and the Andean Uplift, Science, 158, 653-655.

González, G., Cembrano, J., Carrizo, D., Macci, A., Schneider, H., 2003, The link between forearc tectonics and Pliocene-Quarternary deformation of the Coastal Cordillera, northern Chile, Journal of South American Earth Sciences, 16, 321-342.

González, G., Dunai, T., Carrizo, D., Allmendinger, R., 2006, Young displacements on the Atacama Fault System, northern Chile from field observations and cosmogenic 21Ne concentrations., Tectonics, 25, doi:10.1029/2005TC001846.

González, G., Jensen, A., Schneider, H., 1997, Deformaciones recientes en la terminacion norte de la zona de falla de Atacama; Salar Grande, Norte de Chile: Particion de la deformacion por efecto de bloqueamiento del oroclinal andino, VIII Congreso Geologico Chileno, Universidad Catolica Del Norte, 1, 80-84.

Hartley, A. J., and Chong, G., 2002, Late Pliocene age for the Atacama Desert: Implications for the desertification of western South America, Geology, 30, 43-46.

Hartley, A. J., and Jolley, E. J., 1995, Tectonic implications of Late Cenozoic sedimentation from the Coastal Cordillera of northern Chile (22°-24° S), Journal of the Geological Society, London, 152, 51-63.

Hervé, M., 1987a, Movimiento Normal de la Falla Paposo, Zona de Falla Atacama, En El Mioceno, Chile, Revista Geologica de Chile, 31, 31-36.

Hervé, M., 1987b, Movimiento Sinistral en el Cretacico inferior de la Zona de Falla Atacama Al Norte de Paposo (24° S), Chile, Revista Geologica de Chile, 31, 37-42.

Hoke, G. D., Isacks, B. L., Jordan, T. E., Tomlinson, A. J., Blanco Pavez, N., and Razmezani, J., 2007, Geomorphic evidence for post-10 Ma uplift of the western flank of the central Andes 18°30'-22°S, Tectonics, 26 doi:/10.1029/2006TC002082.

Hoke, G. D., Isacks, B. L., Jordan, T. E., and Yu, J. S., 2004, Groundwater-sapping origin for the giant quebradas of northern Chile, Geology, 32, 605-608.

Kendrick, E., Bevis, M., Smalley, R. Jr., Brooks, B., Vargas, R. B., Lauría, E., Fortes, L. P. S., 2003, The Nazca-South America Euler vector and its rate of change, Journal of South American Earth Sciences, 16.

Klotz, J., Angermann, D., Michel, G., Porth, R., Reigber, C., Reinking, J., Viramonte, J., Perdomo, R., Rios, V., Barrientos, S., Barriga, R., Cifuentes, O., 1999, GPS-derived deformation of the Central Andes including the 1995 Antofagasta M(w)=8.0 earthquake, Pure and Applied Geophysics, 154, 709-730.

Latorre, C., Betancourt, J. L., Rylander, K. A., Quade, J., 2002, Vegetation invasions into absolute desert: A 45,000 yr rodent midden record from the Calama-Salar de Atacama basins, northern Chile (lat 22° - 24° S), Geological Society of America Bulletin, 114, 349-366.

Li, C., 1995, Forearc Structures and Tectonics in the Southern Peru-Northern Chile Continental Margin, Marine Geophysical Researches, 17, 97-113.

Loveless, J. P., Hoke, G. D., Allmendinger, R. W., González, G., Isacks, B. L., Carrizo, D. A., 2005, Pervasive cracking of the northern Chilean Coastal Cordillera: New evidence of forearc extension., Geology, 33, 973-976.

McCaffrey, R., 1996, Estimates of modern arc-parallel strain rates in fore arcs, Geology, 24, 27-30.

Miller, A., 1976, The Climate of Chile, in Climates of Central and South America, edited by W. Schwerdtfeger, pp. 532.

Mortimer, C., 1973, The Cenozoic history of the southern Atacama Desert, Chile, Journal of the Geological Society, London, 129, 505-526.

Mortimer, C., 1980, Drainage Evolution in the Atacama Desert of Northernmost Chile, Revista Geologica de Chile, 11, 3-28.

Mortimer, C., Farrar, E., Saric, N., 1974, K-Ar ages from Tertiary lavas of the northernmost Chilean Andes, Geologische Rundschau, 63, 484-490.

Mortimer, C., and Saric, N. R., 1972, Landform evolution in the coastal region of Tarapaca province Chile, Revue de Geomorphologie Dynamique, 4, 162-170.

Mortimer, C., and Saric, N., 1975, Cenozoic studies in northernmost Chile, Geologische Rundschau, 64, 395-400.

Naranjo, J., 1987, Interpretacion de la Actividad Cenozoica Superior a Lo Largo de la Zona de Falla Atacama, Norte de Chile, Revista Geologica de Chile, 31, 43-55.

Niemeyer, H., González, G., Martinez-De Los Rios, E., 1996, Evolución tectónica cenozoica del margen continental activo de Antofagasta, norte de Chile., Revista Geológica de Chile, 23, 165-186.

Okada, A., 1971, On the neotectonics of the Atacama fault zone region: Preliminary notes on Late Cenozoic faulting and geomorphic development of the Coast Range of northern Chile., Bulletin of the Department of Geography University of Tokyo, 47-65.

Pardo-Casas, F., and Molnar, P., 1987, Relative motion of the Nazca (Farallon) and South American plates since Late Cretaceous time, Tectonics, 6, 233-248.

Randall, D. E., Taylor, G., Grocott, J., 1996, Major crustal rotations in the Andean margin: Paleomagnetic results from the Coastal Cordillera of northern Chile, Journal of Geophysical Research, 101, 15,783-715,798.

Rech, J. A., Quade, J., Betancourt, J. L., 2002, Late Quaternary paleohydrology of the central Atacama Desert (lat 22-24S), Chile, Geological Society of America Bulletin, 114, 334-348.

Reijs, J., and McClay, K., 1998, Salar Grande pull-apart basin, Atacama Fault System, northern Chile, in Continental Transpressional and Transtensional Tectonics, edited by R. E. Holdsworth, et al., pp. 127-141, Geological Society Special Publications, London.

Riquelme, R., Martinod, J., Hérail, G., Darrozes, J., Charrier, R., 2003, A geomorphological approach to determining the Neogene to Recent tectonic deformation in the Coastal Cordillera of northern Chile (Atacama), Tectonophysics, 361, 255-275.

Ruff, L. J., and Kanamori, H., 1980, Seismicity and the subduction process, Physics of the Earth and Planetary Interiors, 23, 240-252.

Rutland, R. W. R., 1971, Andean Orogeny and Ocean Floor Spreading, Nature, 233, 252-255.

Scheuber, E., and González, G., 1999, Tectonics of the Jurassic-early Cretaceous magmatic arc of the north Chilean Coastal Cordillera (22°-26°S): a story of crustal deformation along a convergent plate boundary, Tectonics, 18, 895-910.

Scheuber, E., and Reutter, K.-J., 1992, Magmatic arc tectonics in the Central Andes between 21° and 25° S, Tectonophysics, 205, 127-140.

Tichelaar, B. W., and Ruff, L. J., 1991, Seismic coupling along the Chilean subduction zone, Journal of Geophysical Research, 96, 11997-12022.

von Huene, R., and Lallemand, S. E., 1990, Tectonic erosion along the Japan and Peru convergent margins, Geological Society of America Bulletin, 102, 704-720.

CHAPTER 2

A DIGITAL ELEVATION MODEL OF THE NORTH CHILEAN FOREARC DERIVED FROM INTERFEROMETRIC SYNTHETIC APERTURE RADAR

Remote sensing platforms image the Earth in nearly every transparent atmospheric window in the electromagnetic spectrum. Some of these data are transformed into digital elevation models (DEM) with resolutions as low as 1 meter or coverage spanning a continent. The availability of DEMs combined with advances in computing have greatly influenced research in fields such as climate modeling, tectonics, and geomorphology. DEMs have allowed researchers to broaden the scope of their work to a regional and sometimes global perspective, making quantitative analyses possible.

The research in this dissertation is largely based on a 20-meter digital elevation model (DEM) that we generated from raw pairs of synthetic aperture radar (SAR) data that imaged the Central Andean forearc from 18° S to 26° S latitude. The data were acquired from the European Space Agency's (ESA) Earth Remote Sensing (ERS) -1 and -2 C-band (5.6 cm) active microwave SAR platforms. We applied the technique of SAR interferometry (INSAR) (Zebker and Goldstein 1986, Zebker et al. 1994) to the data to produce a nearly complete digital topographic map of the study area. This chapter reviews the steps involved with processing the raw SAR scenes to the final DEM product. We describe the general properties of the DEM, criteria for SAR scene selection, INSAR processing of SAR data into interferograms, ground-truthing and generation of height maps, and geocoding and mosaicking the

individual DEMs into a continuous dataset. We also address the errors and inherent limitations of the DEM, and finally describe the additional by-products from INSAR processing.

The digital topography referred to in Chapter 3 is a compilation of two different datasets: an interferometrically-derived 20-meter DEM and the Cornell 90-meter Digital Terrain Elevation Data (DTED). The former, which comprises two-thirds of the data composite, is the principal focus of this chapter, although mosaicking with the 90-meter topography is addressed under the section Geocoding and Mosaicking below. Chapter 4 makes use of the DEM only.

2.1 *Data Description*

The complete interferometrically-derived DEM maps the northwest portion of the Central Andes which includes the forearc, the monocline – a broad slope connecting the forearc to the plateau, and the western edge of the Altiplano plateau (Figure 2.1). The digital topography has a horizontal resolution of 20 meters and a relative vertical resolution of 2-3 meters. A lack of reliable ground truth data on the Andean plateau is responsible for the absolute vertical accuracy of the entire dataset averaging 82 meters. However when considering solely the better-constrained forearc portion of the DEM, the vertical accuracy reduces to 32 meters. The 20-meter DEM is a compilation of 24 pairs of raw ERS-1 and ERS-2 SAR scenes. Each SAR footprint from ESA is approximately 100 km by 100 km of the Earth's surface with overlap on laterally adjacent tracks (Figure 2.2). All scenes are ascending which means the right-looking SAR images to the east. In general, this produced excellent

Figure 2.1 DEM coverage. Complete 20-meter DEM (color) overlain on GTOPO30 (grayscale) showing the extent of the DEM and the features of the Central Andean forearc.

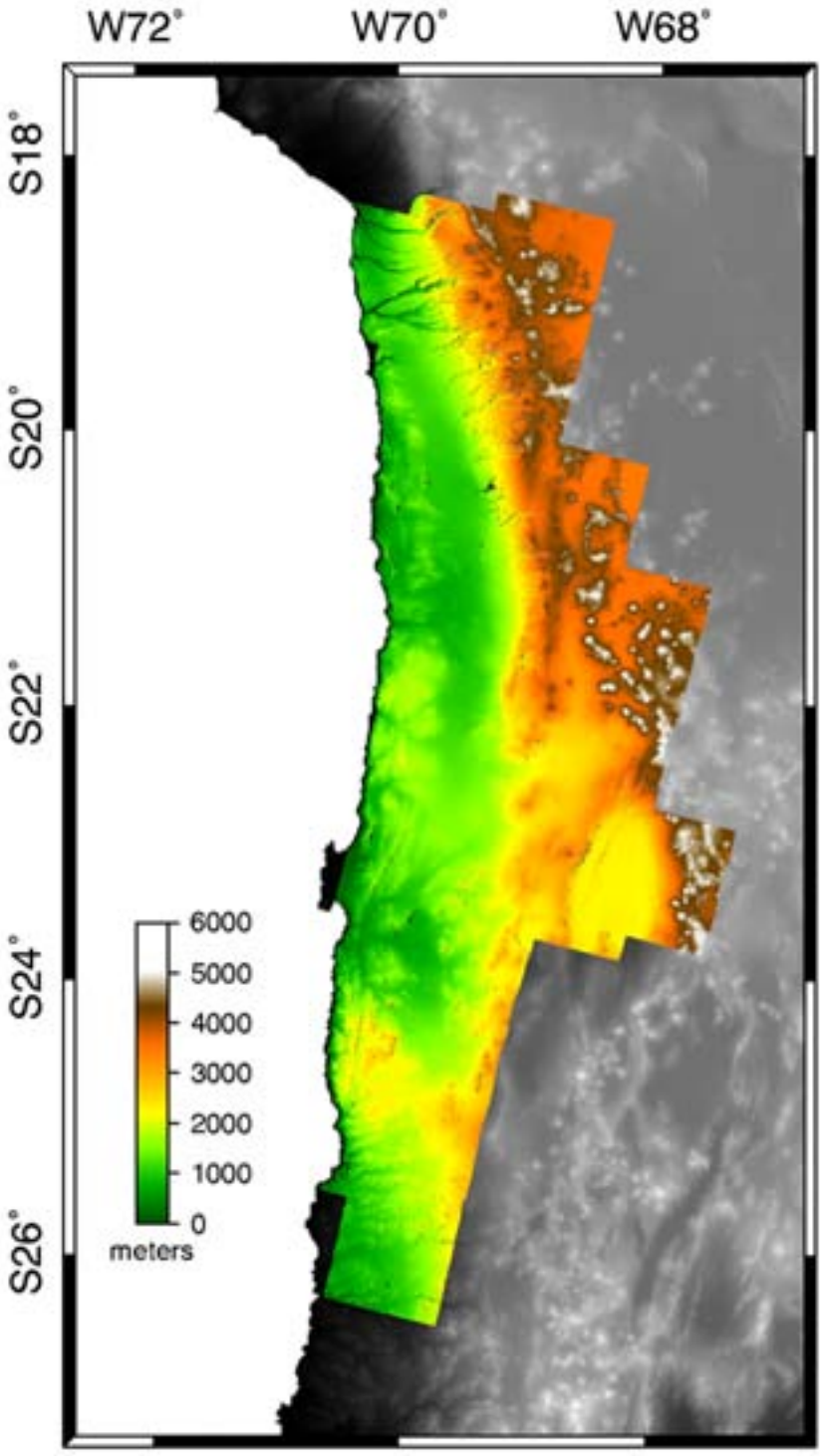
W72°
W70°
W68°
S18°
S20°
S22°
S24°
S26°
6000
5000
4000
3000
2000
1000
0
meters

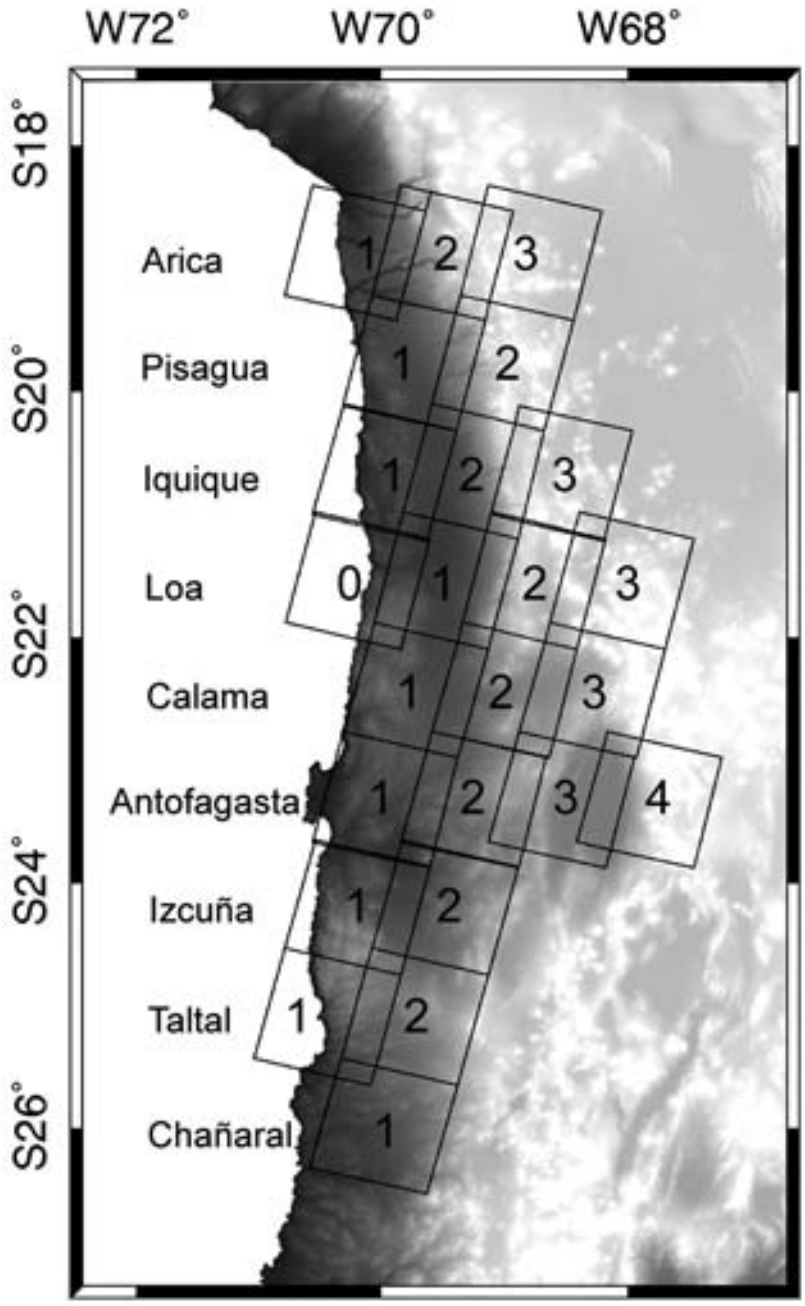

Figure 2.2 Total SAR coverage. Labels and scene numbers correspond with scene parameters in Table 2.1.

results due to the aridity and lack of vegetation on the imaged surfaces. The total area of the INSAR DEM is 170,000 km^2. Overall, the dataset is 99.1% complete; the missing 0.9% falls within zones of radar shadow or decorrelation. The datum for the DEM is WGS84, and the dataset exists in two projections: SUTM19 and the custom projection, TMAndes.

2.2 *Data Selection*

The DEM was generated from unprocessed (raw) SAR products obtained from ESA. Before processing began, we searched the ESA archives for qualified candidates to select SAR acquisitions that best matched the following criteria: 1) the data were already archived at ESA to reduce cost and expedite delivery; 2) at least two scenes existed for a given location as required for interferometry; 3) the spatial baseline was within the accepted theoretical range; 4) a sufficiently short temporal baseline could be found to minimize decorrelation; and 5) minimal or no weather systems were present over the imaged area during the satellite pass. ESA provides an excellent search software package for SAR and some visible and near infrared (VNIR) missions, called Descw, which can be downloaded free of charge from their website.

The first criterion is self-explanatory. The need for a pair of scenes is fundamental to interferometry. The signal for every pixel within a SAR scene has two components, the amplitude and phase. In this context, the phases of the two acquisitions are differenced to produce an interferogram, which is a representation of the topography of the imaged surface that ultimately

becomes a DEM. The spatial baseline refers to the distance separating the two antennae, which can vary for different pairings of SAR acquisitions in the case of repeat-pass interferometry. Theoretical limits dictate that baselines exceeding 1115 meters for ERS-1 systems over flat terrain result in complete loss of coherence (Zebker et al., 1994). On the other hand, a balance must exist between a baseline long enough to reduce height errors and a baseline small enough to avoid decorrelation. Topographic mapping from repeat-pass interferometry ideally requires the shortest possible temporal baseline because of the sensitivity to changes on the surface that may occur over time. The ERS-1 and ERS-2 satellites have individual repeat times of 35 days, however ESA ran the two missions in tandem for several orbits with one day temporal baselines. We took the precautionary step of checking GOES-8 infrared weather satellite data at the location and time of acquisition for the presence of weather systems because atmospheric water vapor can introduce significant errors into interferometrically-derived DEMs. In the event that multiple choices of SAR pairs existed, and all other factors were more or less equal, the GOES-8 imagery determined the final choice of interferometic pairs. Note that the region was generally clear of major systems for the majority of dates and locations examined.

Despite thorough screening for the best possible SAR data, some scenes were unusable. ESA's investigation determined the data were faulty due to errors during downlink from satellite to receiving station. The scenes ultimately processed to create the DEM are listed with SAR parameters in Table 2.1. All scenes are ascending which means the right-looking SAR images to the east.

Table 2.1 SAR Scene Parameters

Name	Track	Frame	Orbit	Mission	Date	Time	Ctr Lat	Ctr Lon
Antofagasta 1	096	4077	21126	ERS-1	30-Jul-1995	14:43:25	23.330	70.076
Antofagasta 1	096	4077	22128	ERS-1	8-Oct-1995	14:43:25	23.327	70.079
Antofagasta 2	325	4077	24862	ERS-1	16-Apr-1996	14:40:32	23.329	69.363
Antofagasta 2	325	4077	5189	ERS-2	17-Apr-1996	14:40:31	23.329	69.362
Antofagasta 3	053	4077	25091	ERS-1	2-May-1996	14:37:41	23.330	68.646
Antofagasta 3	053	4077	5418	ERS-2	3-May-1996	14:37:40	23.330	68.645
Antofagasta 4	282	4077	25320	ERS-1	18-May-1996	14:34:45	23.236	67.896
Antofagasta 4	282	4077	5647	ERS-2	19-May-1996	14:34:47	23.333	67.938
Arica 1	139	3987	25177	ERS-1	8-May-1996	14:47:55	18.883	70.346
Arica 1	139	3987	5504	ERS-2	9-May-1996	14:47:54	18.883	70.345
Arica 2	368	3987	25406	ERS-1	24-May-1996	14:44:59	18.793	69.597
Arica 2	368	3987	5733	ERS-2	25-May-1996	14:45:00	18.884	69.618
Arica 3	096	3987	17986	ERS-2	28-Sep-1998	14:42:02	18.867	68.767
Arica 3	096	3987	18487	ERS-2	2-Nov-1998	14:41:58	18.867	68.767
Calama 1	096	4059	17986	ERS-2	28-Sep-1998	14:43:02	22.433	69.717
Calama 1	096	4059	18487	ERS-2	2-Nov-1998	14:42:58	22.433	69.717
Calama 2	325	4058	25363	ERS-1	21-May-1996	14:40:15	22.350	69.099
Calama 2	325	4059	5690	ERS-2	22-May-1996	14:40:16	22.441	69.122
Calama 3	053	4059	24590	ERS-1	28-Mar-1996	14:37:19	22.439	68.398
Calama 3	053	4059	4917	ERS-2	29-Mar-1996	14:37:20	22.439	68.399
Chañaral 1	325	4131	20854	ERS-1	11-Jul-1995	14:41:00	25.980	69.980
Chañaral 1	325	4131	21355	ERS-1	15-Aug-1995	14:41:00	25.980	69.980
Iquique 1	368	4023	24905	ERS-1	19-Apr-1996	14:45:32	20.661	70.093
Iquique 1	368	4023	5232	ERS-2	20-Apr-1996	14:45:31	20.662	70.092
Iquique 2	096	4023	17986	ERS-2	28-Sep-1998	14:42:32	20.661	69.365
Iquique 2	096	4023	18487	ERS-2	2-Nov-1998	14:42:28	20.661	69.365
Iquique 3	325	4023	24862	ERS-1	16-Apr-1996	14:39:47	20.661	68.656
Iquique 3	325	4023	5189	ERS-2	17-Apr-1996	14:39:46	20.661	68.654
Izcuña 1	096	4095	24633	ERS-1	31-Mar-1996	14:43:36	24.214	70.325
Izcuña 1	096	4095	4960	ERS-2	1-Apr-1996	14:43:35	24.215	70.324
Izcuña 2	325	4094	25363	ERS-1	21-May-1996	14:40:45	24.126	69.584
Izcuña 2	325	4095	5690	ERS-2	22-May-1996	14:40:46	24.217	69.607
Loa 0	368	4040	25406	ERS-1	24-May-1996	14:45:44	21.463	70.288
Loa 0	368	4041	5733	ERS-2	25-May-1996	14:45:45	21.554	70.310

Table 2.1 (Continued)

Name	Track	Frame	Orbit	Mission	Date	Time	Ctr Lat	Ctr Lon
Loa 1	096	4041	17986	ERS-2	28-Sep-1998	14:42:47	21.533	69.467
Loa 1	096	4041	18487	ERS-2	2-Nov-1998	14:42:43	21.533	69.467
Loa 2	325	4040	25363	ERS-1	21-May-1996	14:40:00	21.463	68.852
Loa 2	325	4041	5690	ERS-2	22-May-1996	14:40:01	21.554	68.875
Loa 3	053	4041	24590	ERS-1	28-Mar-1996	14:37:04	21.552	68.153
Loa 3	053	4041	4917	ERS-2	29-Mar-1996	14:37:04	21.552	68.152
Pisagua 1	368	4004	25406	ERS-1	24-May-1996	14:45:14	19.684	69.819
Pisagua 1	368	4005	5733	ERS-2	25-May-1996	14:45:15	19.776	69.841
Pisagua 2	096	4005	17986	ERS-2	28-Sep-1998	14:42:17	19.767	69.000
Pisagua 2	096	4005	18487	ERS-2	2-Nov-1998	14:42:13	19.767	69.000
Taltal 1	096	4113	24633	ERS-1	31-Mar-1996	14:43:51	25.104	70.564
Taltal 1	096	4113	4960	ERS-2	1-Apr-1996	14:43:50	25.104	70.563
Taltal 2	325	4112	25363	ERS-1	21-May-1996	14:41:00	25.015	69.823
Taltal 2	325	4113	5690	ERS-2	22-May-1996	14:41:01	25.106	69.846

2.3 *INSAR Processing*

All of the processing involved in producing interferograms from the raw SAR data was performed with the Gamma Remote Sensing AG Modular SAR Processor (MSP) version 10.4 and Interferometric SAR Processor (ISP) version 8.8 software packages. MSP converts each raw SAR image into a single-look complex image (SLC). The ISP suite of programs take a pair of corresponding SLCs as input to produce a height map for the area of coverage. The entire 20-meter DEM was processed at Cornell University in Ithaca, New York and NASA Jet Propulsion Laboratory in Pasadena, California on Sun Ultra 10 and Sun Sparc 20 platforms. We briefly review the steps involved in generating an SLC, the interferogram and eventually the height map. For an overview of SAR processing, we recommend Raney (1998) and Lewis and Henderson (1998). The reader will find thorough treatment of SAR theory and processing in Curlander and McDonough (1991) and Elachi (1987). Madsen and Zebker (1998) deliver a basic review of interferometric topographic mapping. Hanssen (2001) provides a more detailed discussion of INSAR and its applications.

Each raw scene is approximately 300 megabytes in size and was scanned for missing lines of data. Missing lines can render scenes unusable for successful interferometry and were not uncommon in our data. The presence of these errors ranged from a few to as many as 400 in the more problematic scenes. We identified and fixed missing lines by inserting a replication of the preceding full line. Next we determined the Doppler centroid, the zero of the Doppler spectrum for a radar beam moving over a target, to maximize the

signal-to-noise ratio (SNR) and reduce ambiguities in azimuth (along-track direction). Then we calculated the power spectrum in range (across-track direction) from the raw data and applied range compression to recover full range resolution. The along-track velocity of the antenna was estimated from cross correlation of parts of the azimuth Doppler spectrum to focus the data. We applied azimuth compression to the range compressed data and then absolute radiometric calibration to produce the SLC.

An SLC is essentially an array of complex numbers representing the amplitude and phase for each pixel. Each SLC was greater than one gigabyte. Once we obtained two SLCs for the same area, we needed to co-register the images before we could begin interferometric processing. One scene was designated the master or the reference scene and all subsequent calculations were performed in the master geometry. We determined image offset polynomials between the scenes for both azimuth and range in order to resample the slave to the master geometry. Image co-registration was accurate to better than 0.1 pixel, an important prerequisite for interferometry. An upper bound of 0.2 pixel accuracy translates into no more than 5% loss in interferometric correlation. The phase coherence was generally high for all scenes, allowing us to measure offsets based on fringe visibility rather than image intensity. After resampling the slave scene, the complex normalized interferogram was calculated by cross correlation of the master and slave SLCs. Multi-look averaging at 1 look in range for every 5 looks in azimuth was implemented to improve interferometric phase and correlation. For ERS-1 and ERS-2 processing, 1:5 multi-looking yields higher resolution cells (20 meters for 1:5,

40 meters for 2:10) and is typically applied to regions of good to excellent correlation.

The perpendicular baseline is the spatial baseline when the slave orbit passes through the zero-Doppler point of the master path. This component was estimated from precision state vectors for every scene archived by ESA. At this stage in the processing, a phase ramp exists in the interferogram due to the viewing geometry of the SAR platforms. We predicted this phase contribution from the baseline parameters and removed it to isolate the topographic signal for a "flat Earth". Flat-Earth phase removal facilitated filtering and phase unwrapping of the complex interferogram. The phase values of the flat Earth interferogram are all modulo 2π. Phase unwrapping is necessary to resolve this ambiguity. Before unwrapping, we applied an adaptive filter to smooth the interferogram to decrease phase noise and residues, both of which can introduce errors in phase unwrapping. We then identified regions in the interferogram that had low correlation or contained residues and built a structure for phase unwrapping to follow to minimize discontinuities in the phase. Although scenes over high-relief terrain posed the greatest problems, the majority of the interferograms unwrapped without difficulty.

2.4 *Ground-Truthing and Height Map Generation*

The initial spatial baseline calculated from orbital state vectors is not precise enough to generate accurate topography with the unwrapped interferogram. Ground control point (GCP) selection is necessary to improve the baseline

estimate. GCP selection was a combination of both hand-picked and computer-sampled points to accommodate insufficient high-resolution base map coverage of the imaged areas. Hand-picked GCPs were extracted from benchmarks off of the 1:50,000 Chilean Instituto Geográfico Militar topographic maps and 1:100,000 regional topographic maps. Automated GCP selection was run on the limited Cornell 90-meter digital topography and the GTOPO30 1-kilometer digital topography. On average, a single scene had 250 hand-picked points from maps, up to 2000 computer-sampled points from digital topography, or some combination of the two. We attempted to ensure an even spatial distribution of GCPs within each interferogram and culled outliers with errors greater than 3σ from the GCP list. Ideally, GCPs should be located on smooth terrain for better fits. Unfortunately, most of the points identified with greatest confidence from maps were benchmarks on peaks. We fitted GCP coordinates, elevation, and unwrapped phase with a non-linear least squares algorithm to obtain a precision baseline for each scene (Table 2.2). The height map was calculated from the precision baseline and unwrapped phase to determine the elevation and position of each pixel on a spherical earth. Mean square height errors averaged 32 meters for 24 height maps. We resampled the height map from slant range geometry (SAR coordinates) to orthonormal coordinates to produce the orthorectified height map.

Table 2.2 Baseline Estimates and Height Errors

Scene	Perpendicular Baseline (m)	Auto Mean Square Height Error (m)	Auto Minimum (m)	Auto Maximum (m)	Final Mean Square Height Error (m)
Antofagasta 1	343.00462	61.881	-261.164	245.508	15.532
Antofagasta 2	97.6911	20.781	-63.034	62.986	19.578
Antofagasta 3	98.59525	13.134	-48.832	53.201	13.134
Antofagasta 4	74.14367	243.463	-746.263	741.18	243.463
Arica 1	188.32059	110.968	-329.097	328.82	53.282
Arica 2	62.15193	323.582	-968.659	963	28.897
Arica 3	114.12867	23.895	-69.349	68.497	23.658
Calama 1	129.12996	46.226	-225.648	225.556	11.814
Calama 2	60.04036	145.175	-432.588	435.213	29.124
Calama 3	42.14951	25.786	-76.641	75.538	25.786
Chañaral	163.97911	15.572	-45.817	46.082	15.572
Iquique 1	118.81246	25.061	-75.056	73.343	13.625
Iquique 2	114.67781	18.144	-53.866	53.833	18.144
Iquique 3	97.55884	28.232	-83.317	83.951	18.353
Izcuña 1	75.47462	36.328	-108.1	108.656	36.328
Izcuña 2	54.11747	156.844	-460.503	466.782	34.372
Loa 0	90.52357	183.552	-533.997	508.005	16.566
Loa 1	118.48666	19.184	-57.348	57.257	13.903
Loa 2	63.75331	236.513	-703.918	689.992	22.97
Loa 3	65.27372	26.89	-80.221	79.486	26.89
Pisagua 1	84.58521	170.917	-509.561	508.607	15.351
Pisagua 2	116.44436	31.168	-93.096	93.074	31.168
Taltal 1	86.61085	18.096	-53.413	53.674	18.096
Taltal 2	57.90894	151.631	-449.183	434.539	15.53

2.5 *Geocoding and Mosaicking*

It was necessary to geocode the height maps into a common reference projection to relate them to data from other sources. The highest resolution base map available was the Landsat Thematic Mapper (TM) VNIR imagery with a 30 meter pixel spacing. There exists a fundamental flaw with the TM base map itself. Landsat TM scenes were individually registered to a variety

of paper maps and mosaicked together. Because the entire dataset spanned multiple UTM zones, it was necessary to create a unique UTM projection to reduce overall discrepancies in geocoding. The common projection for the data is TMAndes, a custom UTM projection centered on the 70° W meridian with a false northing of 10000000.0 meters and a false easting of 2000000.0 meters.

Ideally, we would mosaic the height maps together and then geocode them to the TM composite to minimize warping. Due to computing limitations, we were forced to co-register the height maps to the TM mosaic before merging them into one dataset. We rectified the height maps using ERMapper software to register points in the DEM with known coordinates for the same points in the TM map. Each DEM had approximately 50 evenly distributed points and was warped by a polynomial equation that best fit the TM map projection. It should be noted that while this was the best solution at the time, it is not an ideal solution. The newer Landsat Enhanced Thematic Mapper (ETM) and SRTM datasets provide a more recent and more accurate basemap for the DEM. Re-registration of the DEM to one or both of these basemaps would greatly improve the overall quality and reliability of the dataset.

Rectifying the DEMs to the TMAndes projection resulted in an excellent match of the two datasets. The DEMs, however, had noticeable offsets from each other at their scene boundaries because of the individual errors in baseline determination and GCP selection during height map calculation. We mosaicked the DEMs together in ARC/INFO to smooth seam mismatches. Once the 20-meter DEM was completed, we merged portions of the 90-meter

digital topography with the DEM to complete missing sections without SAR coverage.

2.6 *Artifacts and Errors*

Inaccurate spatial baseline estimation is the greatest source of error in absolute elevation determination (Zebker et al. 1994b). This is typically the result of poorly constrained orbital parameters of SAR platforms. Additionally, erroneous GCP registration or lack of uniform GCP distribution propagates a mis-fit spatial baseline solution and introduces an artificial tilt into the DEM. This tilt is evident in adjacent, overlapping scenes within our DEM. To avoid abrupt discontinuities in the topography, we mosaicked and smoothed the scenes by applying a weighted average to the overlapping regions according to the proximity of each pixel in the region to the edge of the overlap. Table 2.2 lists the mean square height errors of automatically-selected GCPs for each height map. The minimum and maximum ranges are based on the GCP errors within 3σ. The 90-meter topographic data did not cover all of the SAR extents. Sections of the 1-kilometer GTOPO30 filled in the 90-meter gaps and generally corresponded to the larger errors. We incorporated hand-picked points from 1:50,000 and 1:100,000 topographic maps for most of the height maps. All of the final mean square height errors are quite good, ranging from 12 meters to 53 meters with the noticeable exception of Antofagasta 4 at 243 meters.

Figure 2.3 shows a graphical representation of the height deviations for the computer-selected GCPs for each scene with its corresponding shaded

Figure 2.3 DEM Errors. Graphical representation of errors for automatically selected ground control points (GCP). The range of values for each scene is given in Table 2.2 and has been normalized to the scale shown at the bottom of each page. The scenes are listed alphabetically and follow the naming convention in Figure 2.2, they are: a) Antofagasta 1, b) Antofagasta 2, c) Antofagasta 3, d) Antofagasta 4, e) Arica 1, f) Arica 2, g) Arica 3, h) Calama 1, i) Calama 2, j) Calama 3, k) Chañaral, l) Iquique 1, m) Iquique 2, n) Iquique 3, o) Izcuña 1, p) Izcuña 2, q) Loa 0, r) Loa 1, s) Loa 2, t) Loa3, u) Pisagua 1, v) Pisagua 2, w) Taltal 1, x) Taltal 2. Blue represents the greatest negative error, red indicates greatest positive error and green is a zero error. White points have no GCP selected. Each error map is accompanied by an image of the corresponding sun-shaded topography. A systematic increase in error magnitude occurs in regions of steep and quickly changing topography.

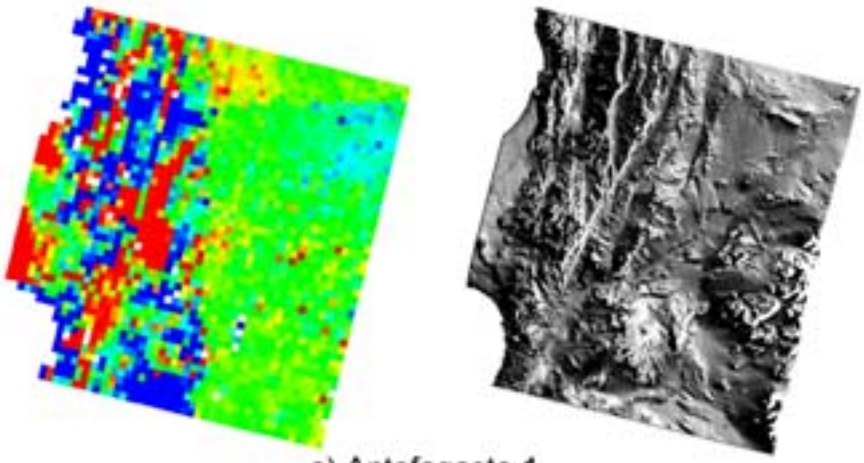

a) Antofagasta 1

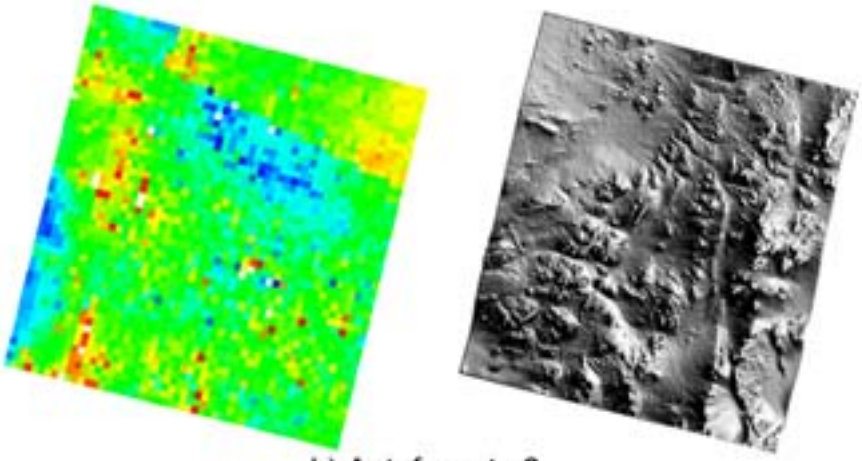

b) Antofagasta 2

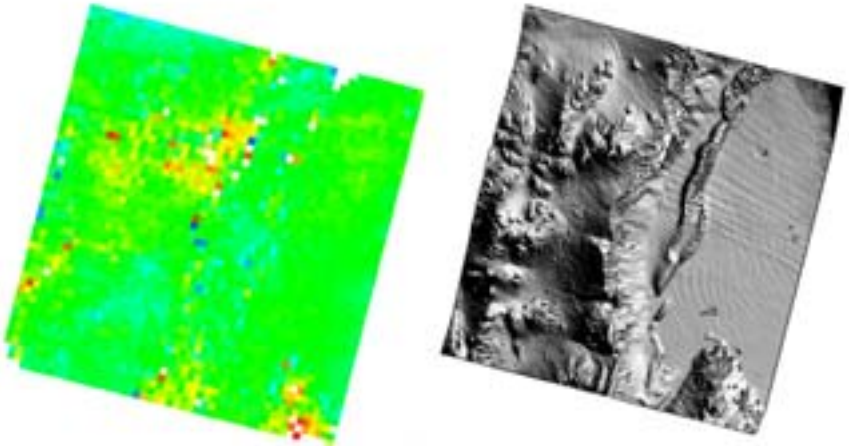

c) Antofagasta 3

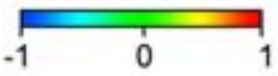

Figure 2.3 (Continued)

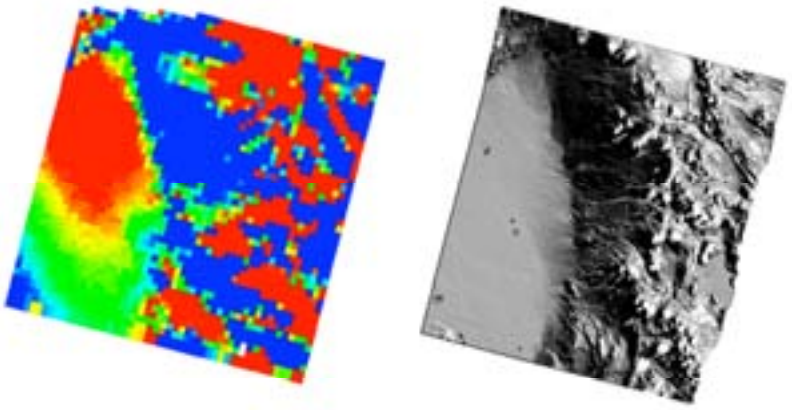

d) Antofagasta 4

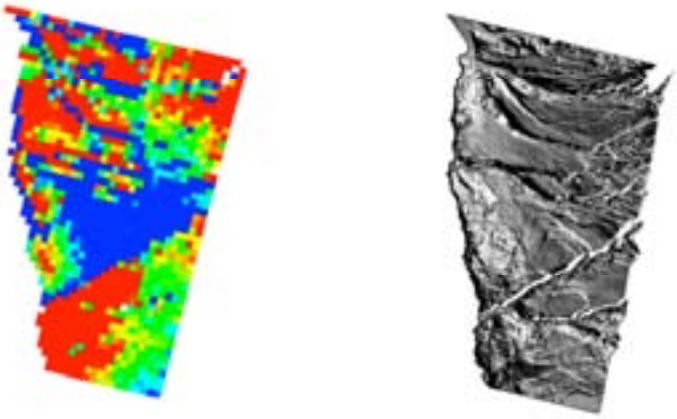

e) Arica 1

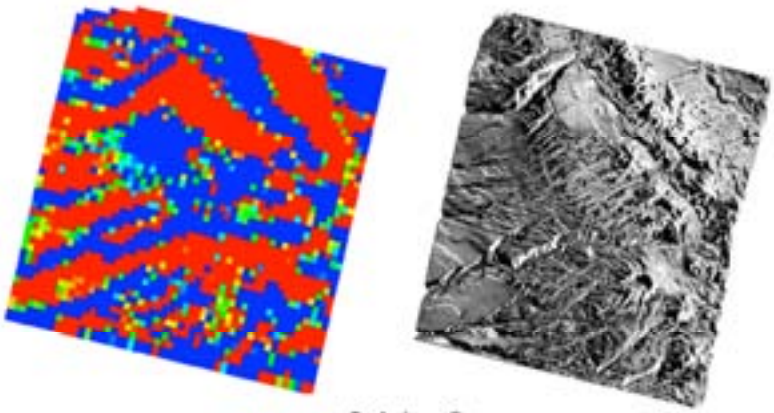

f) Arica 2

Figure 2.3 (Continued)

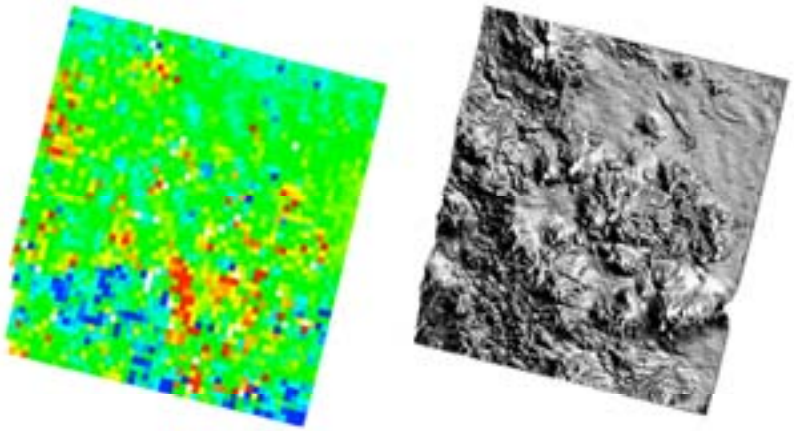

g) Arica 3

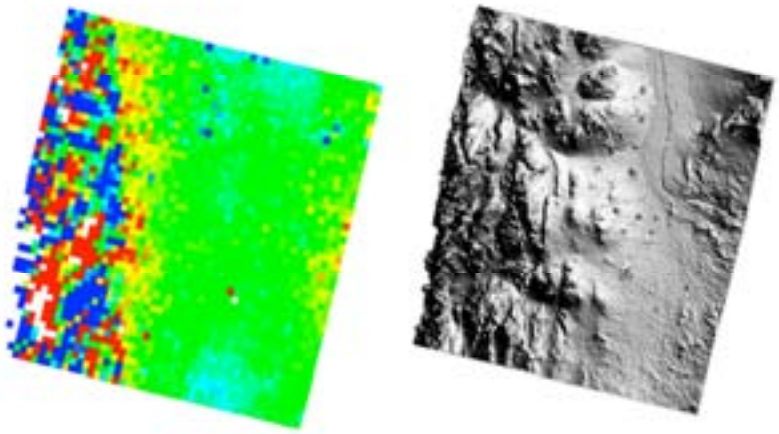

h) Calama 1

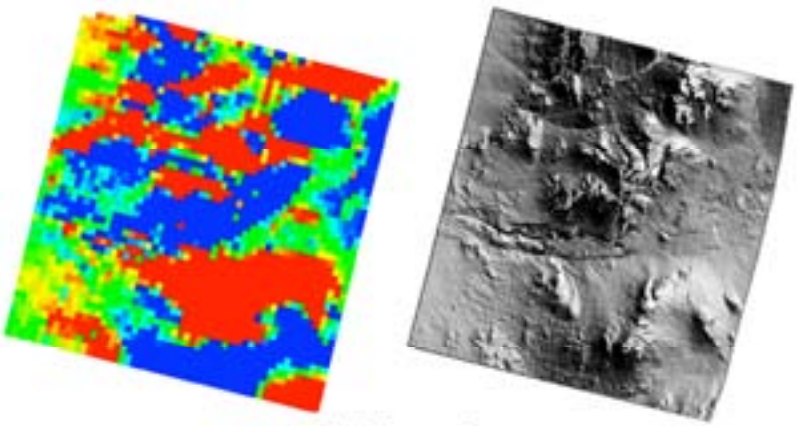

i) Calama 2

Figure 2.3 (Continued)

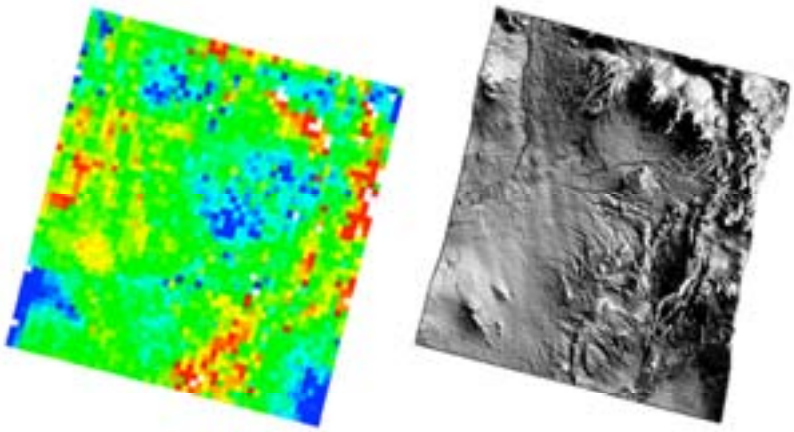

j) Calama 3

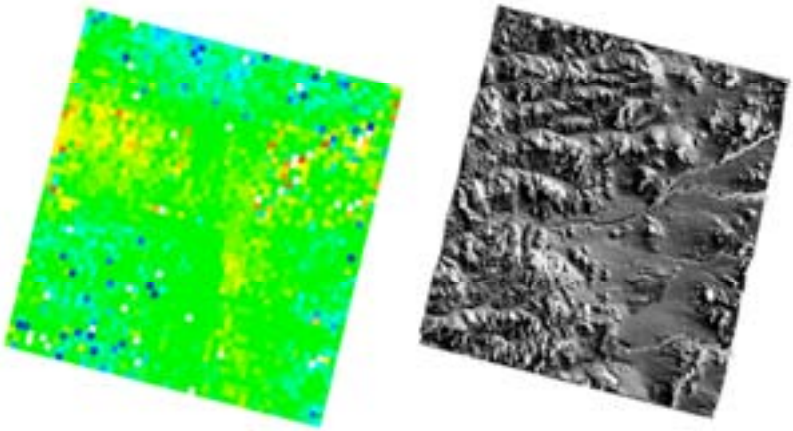

k) Chañaral

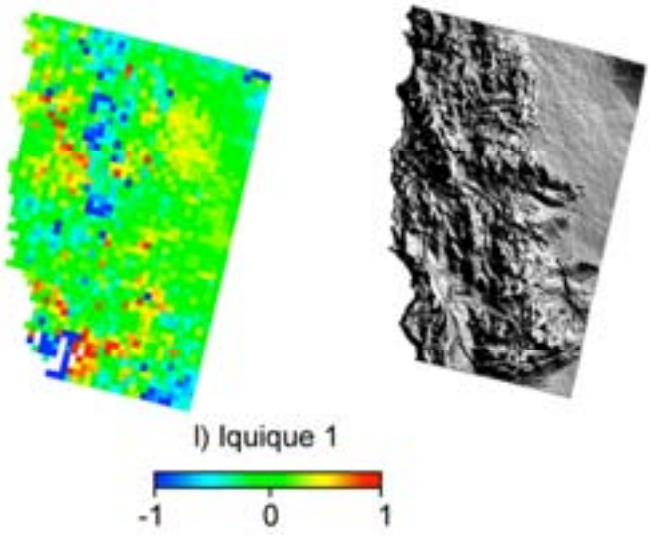

l) Iquique 1

Figure 2.3 (Continued)

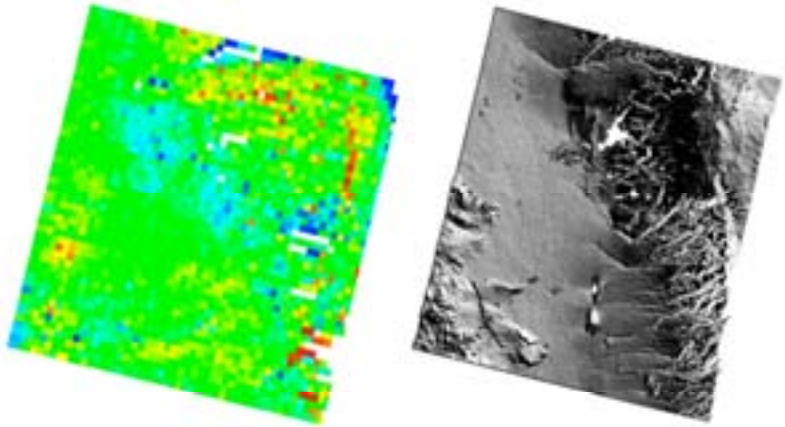

m) Iquique 2

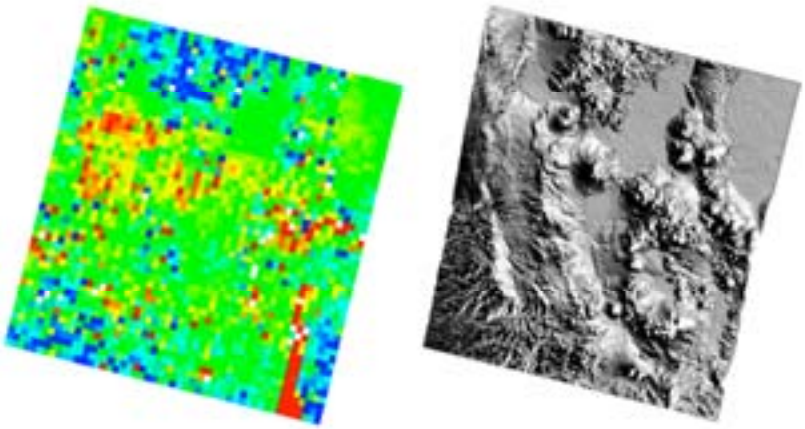

n) Iquique 3

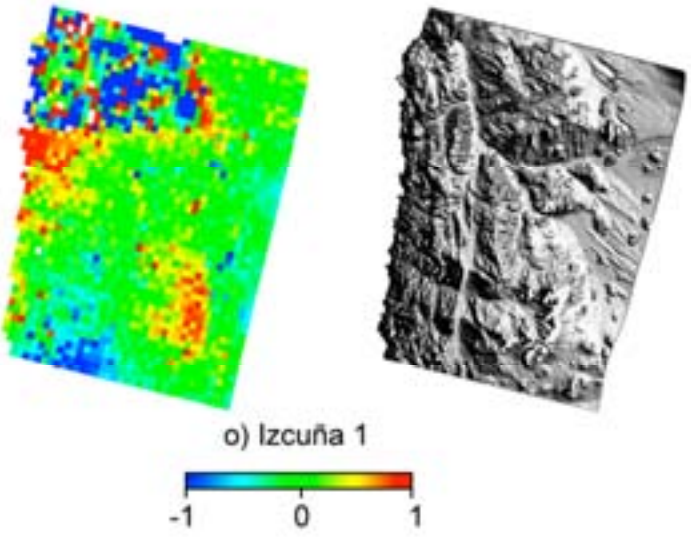

o) Izcuña 1

Figure 2.3 (Continued)

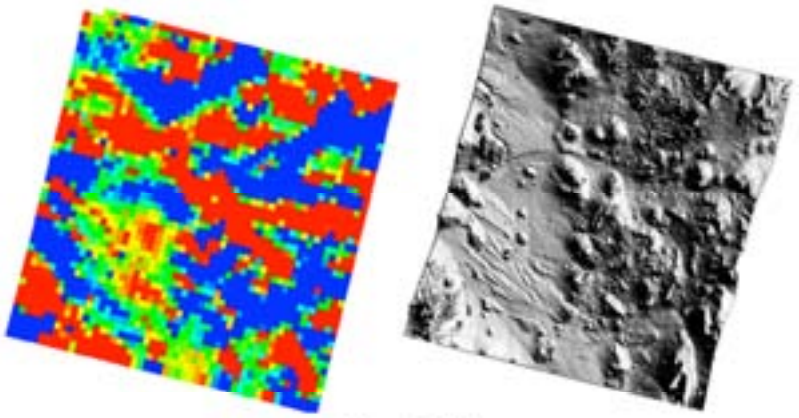

p) Izcuña 2

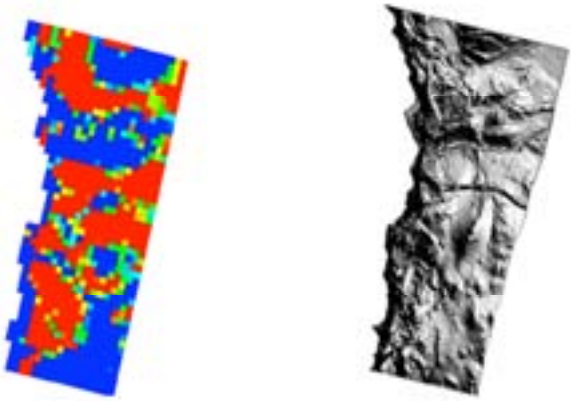

q) Loa 0

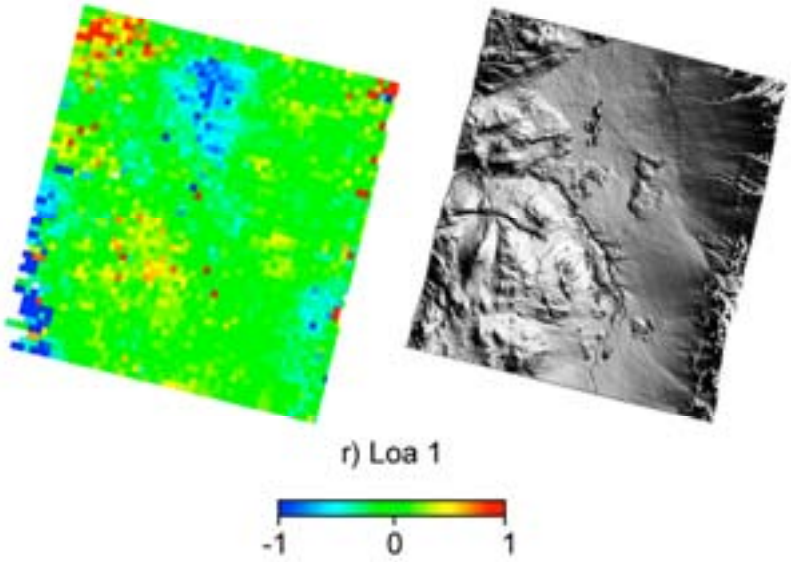

r) Loa 1

Figure 2.3 (Continued)

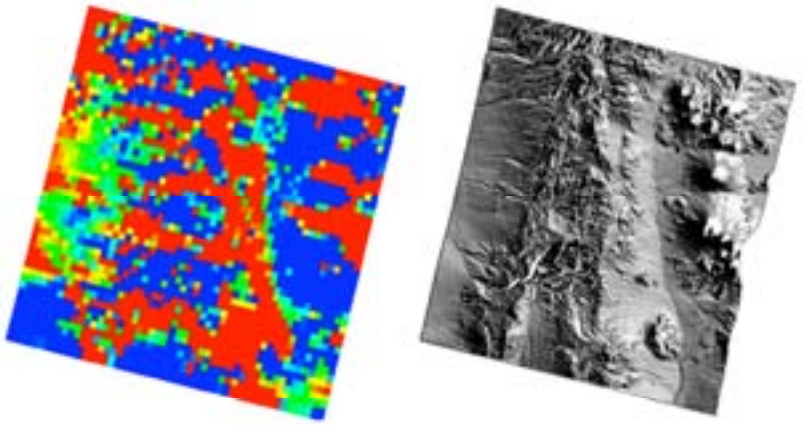

s) Loa 2

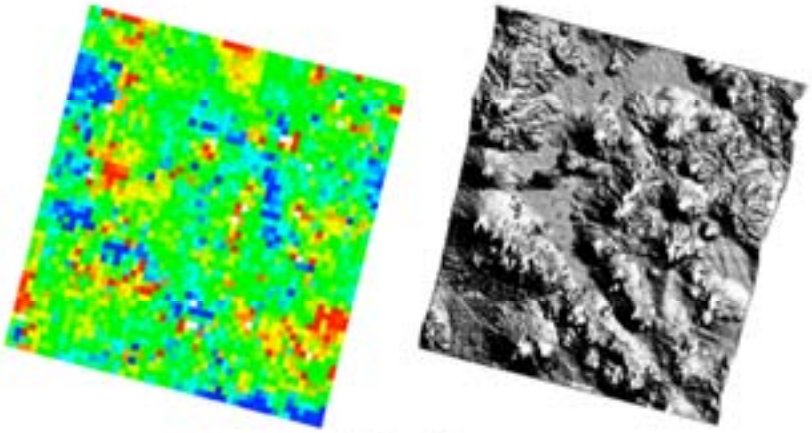

t) Loa 3

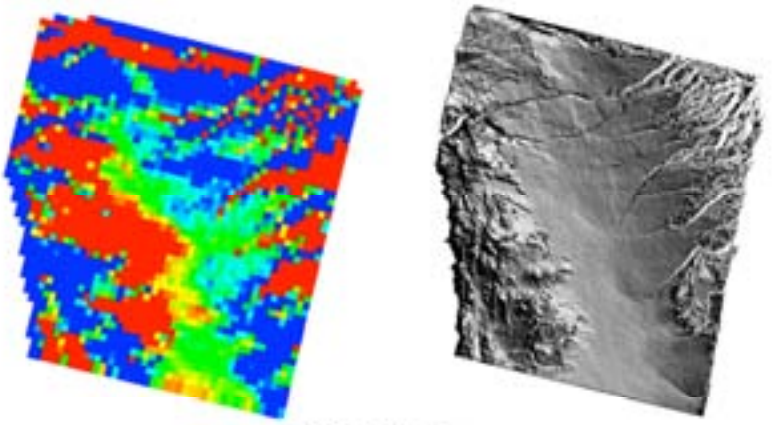

u) Pisagua 1

Figure 2.3 (Continued)

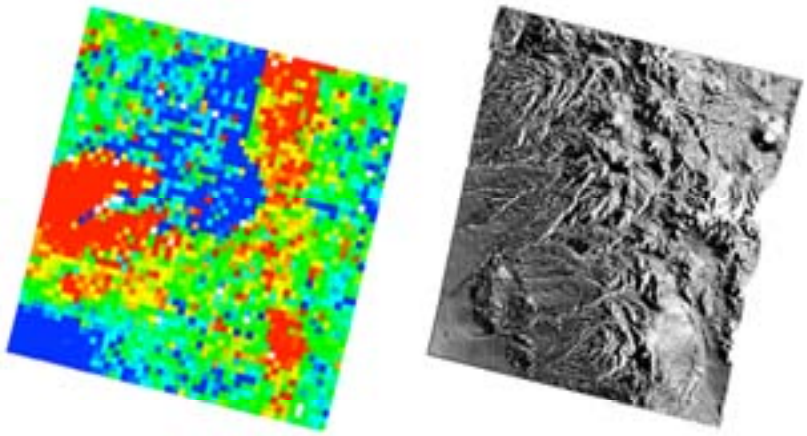

v) Pisagua 2

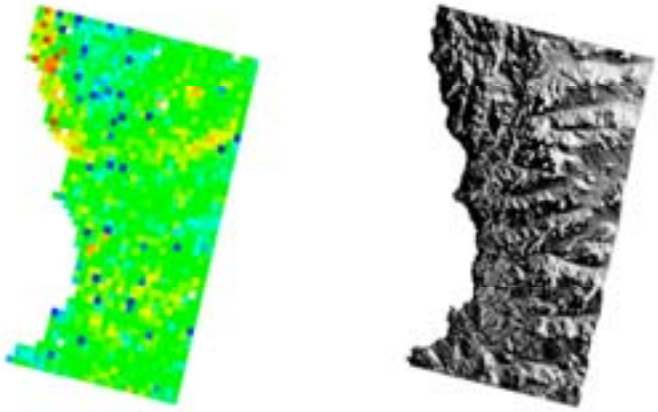

w) Taltal 1

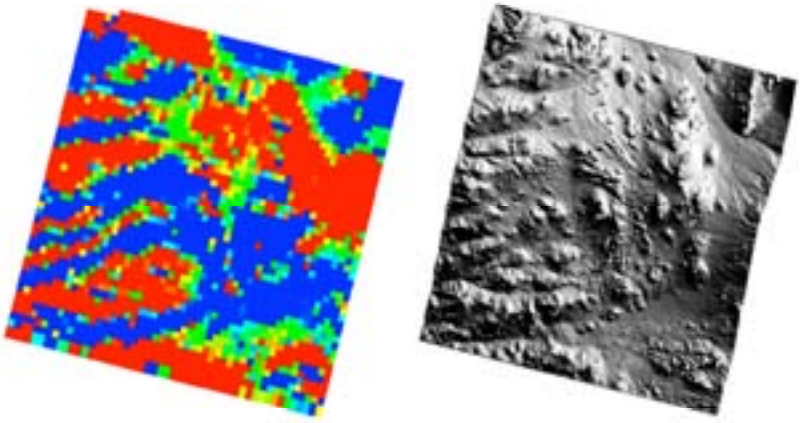

x) Taltal 2

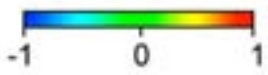

topography for reference. The GCPs are regularly sampled from the digital topography at approximately 2 kilometer spacing and each GCP position is color coded according to a normalized scale from –1 (blue) to 1 (red). Green shading represents zero error, indicating good agreement between the GCP and the interferogram. There is an obvious correlation between scenes with small mean square height errors and predominantly green GCP deviations, sometimes with speckles of red and blue. The error plots for large deviations have high negative and positive errors (blue and red zones) that mimic the features of the topography. The cause for some of these patterns comes from unwrapping errors in the interferogram that could not jump discontinuities such as data dropouts along large canyons (see Figure 2.3e: Arica 1 for an example). In Figures 2.3a and 2.3h, Antofagasta 1 and Calama 1 have distinct transitions from small errors to large errors which are directly related to the change from the 90-meter to the 1-kilometer reference digital topography respectively.

There are small, but noticeable gaps in the 20-meter DEM where data does not exist. The majority of these data dropouts in our DEM correspond to areas of greater topographic relief in radar shadow (typically east-facing slopes) during acquisition because of the side-looking nature of the SAR platform and the fixed radar look direction. Figure 2.4 shows an example of this effect on Volcan Lincancabur and Volcan Juriques, two volcanoes on the Chilean border with Bolivia. The eastern slopes of the high peaks are in radar shadow, as is the inner western edge of the crater on Juriques. Another culprit for lost data comes from decorrelation between scene acquisitions (Zebker and Villasenor 1992), usually from water at the surface or agricultural activity. This

Figure 2.4 Radar shadow zones on eastern flanks of two volcanoes. The side-looking SAR platform of ERS-1 and ERS-2 has an incidence angle of 23.5° from vertical. The leeward side of high relief areas remain in radar shadow and are not imaged. An example of this in the DEM comes from Antofagasta 4. Volcan Lincancabur (west) and Volcan Juriques (east) are missing a significant portion of their eastern slopes. The DEM is shown on the left and the co-registered Landsat TM is on the right with the dropout zone outlined in yellow for reference.

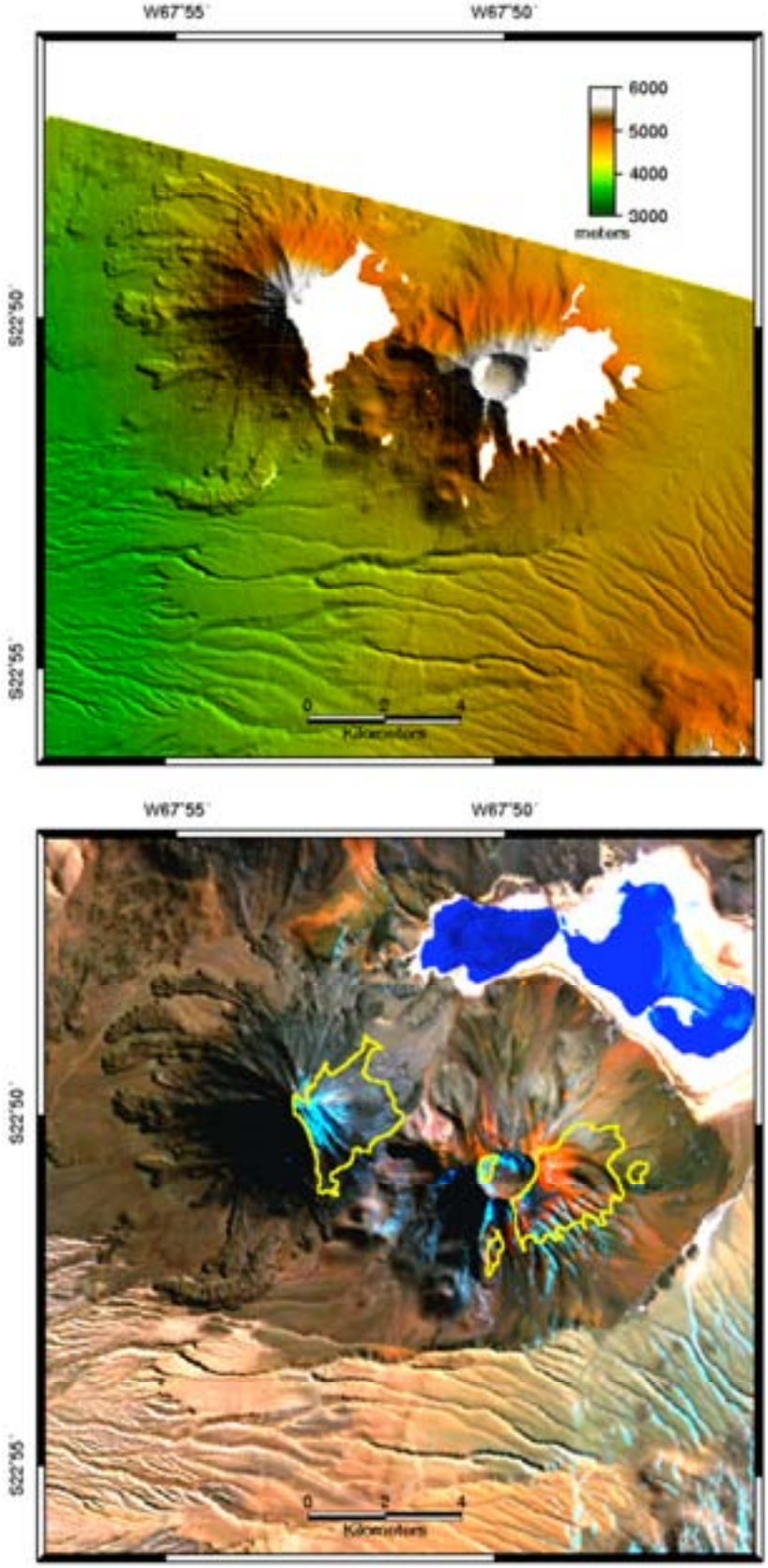
W67°55'
W67°50'
S22°50'
S22°55'
6000
5000
4000
3000
meters
0
2
4
Kilometers
W67°55'
W67°50'
S22°50'
S22°55'
0
2
4
Kilometers

does not tend to pose a major obstacle to our INSAR mapping, due in large part to the aridity of the Atacama Desert. In the case of northern Chile, there are portions of the DEM that decorrelate over a one-day temporal baseline due to sand dunes. Figure 2.5 highlights one of the larger dune fields west of the Coastal Scarp in visible and near-infrared ASTER imagery. The dune field drapes the base of the west-facing slope of the Coastal Scarp such that its geometry should be ideal for imaging, however activity at the surface of the dunes due to winds have resulted in decorrelation over one day from April 19 to April 20 1996.

Although the atmosphere is transparent to microwaves, water vapor can introduce pronounced errors in a DEM (Zebker et al. 1997). Water vapor can delay the propagation of the radar signal resulting in a longer travel time and ultimately an incorrect measure of elevation. Atmospheric signatures can manifest themselves in the topography as ripples, ramps, domes, and depressions. This presents less of a problem in the hyper-arid Atacama Desert, but is nevertheless present in some of the scenes in the study area. One such example is clear in the Salar de Atacama which is imaged by both Antofagasta 3 and Antofagasta 4 (Figure 2.6). Both scenes were acquired with ERS-1 and ERS-2 tandem pairs and have 1 day temporal baselines. Antofagasta 3 was imaged on May 2 and May 3 in 1996, Antofagasta 4 was imaged just over two weeks later on May 18 and May 19.

Ripples are evident on the flat surface of the Salar de Atacama in Antofagasta 3, yet absent from the same area in Antofagasta 4. A profile taken across a

Figure 2.5 Decorrelation due to surface change. In the Iquique 1 DEM, a data dropout region lies on the west-facing slope of the Coastal Scarp. This region is not in radar shadow. The surface has decorrelated over a one-day temporal baseline (April 19 to April 20 1996) because of shifting sand dunes on the slopes of the Coastal Scarp. The DEM is shown on the left and the co-registered ASTER image is shown to the right with the decorrelation zone outlined in black.

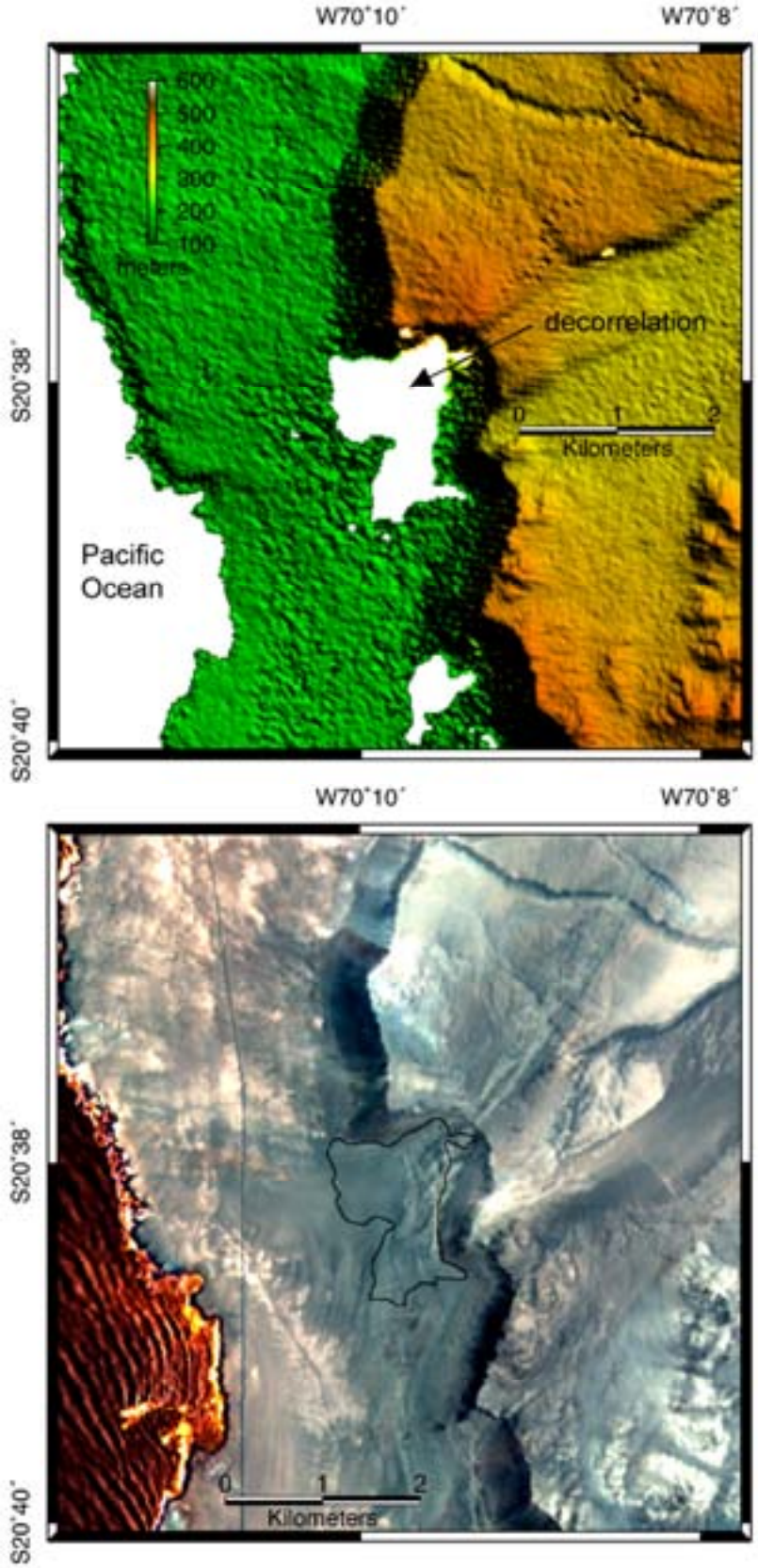
W70°10′
W70°8′
S20°38′
S20°40′
600
500
400
300
200
100
meters
decorrelation
0
1
2
Kilometers
Pacific
Ocean
W70°10′
W70°8′
S20°38′
S20°40′
0
1
2
Kilometers

Figure 2.6 Atmospheric artifact in topography of Salar de Atacama. The ripples on the surface of the Salar de Atacama are a peculiar and transient signal in the Antofagasta 3 DEM (6a), which was acquired on May 2 and May 3 in 1996. A profile across the ripples shows a 5 meter amplitude over a 2-3 kilometer wavelength. The same region was imaged by Antofagasta 4 on May 18 and May 19 of 1996 and the DEM reveals no such pattern in the topography (6b). The ripple effect is absent from the same profile taken from the Antofagasta 4 DEM, a key indicator of an atmospheric error introduced in the data. It is important to note the differing general slope in the profiles of Antofagasta 3 and Antofagasta 4. This discrepancy is a result of poor baseline constraints for Antofagasta 4. However, the overall slope has no influence on the shorter wavelength atmospheric contribution. Both profiles were sampled from the DEM and then smoothed with a hanning window of 5.

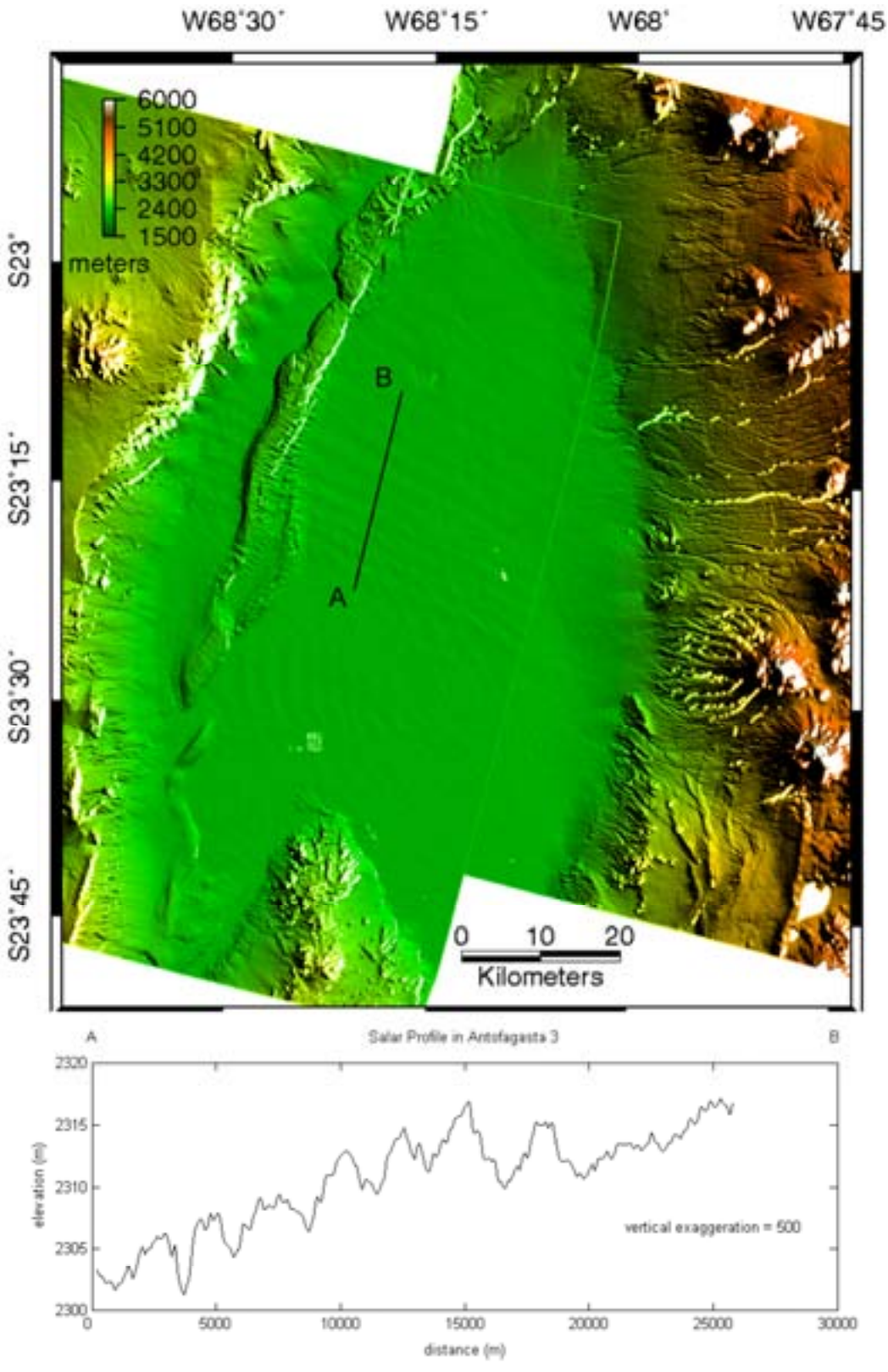
W68°30'
W68°15'
W68°
W67°45
S23°
S23°15'
S23°30'
S23°45'
6000
5100
4200
3300
2400
1500
meters
A
B
0 10 20
Kilometers
A
Salar Profile in Antofagasta 3
B
elevation (m)
2320
2315
2310
2305
2300
vertical exaggeration = 500
0
5000
10000
15000
20000
25000
30000
distance (m)

6a

Figure 2.6 (Continued)

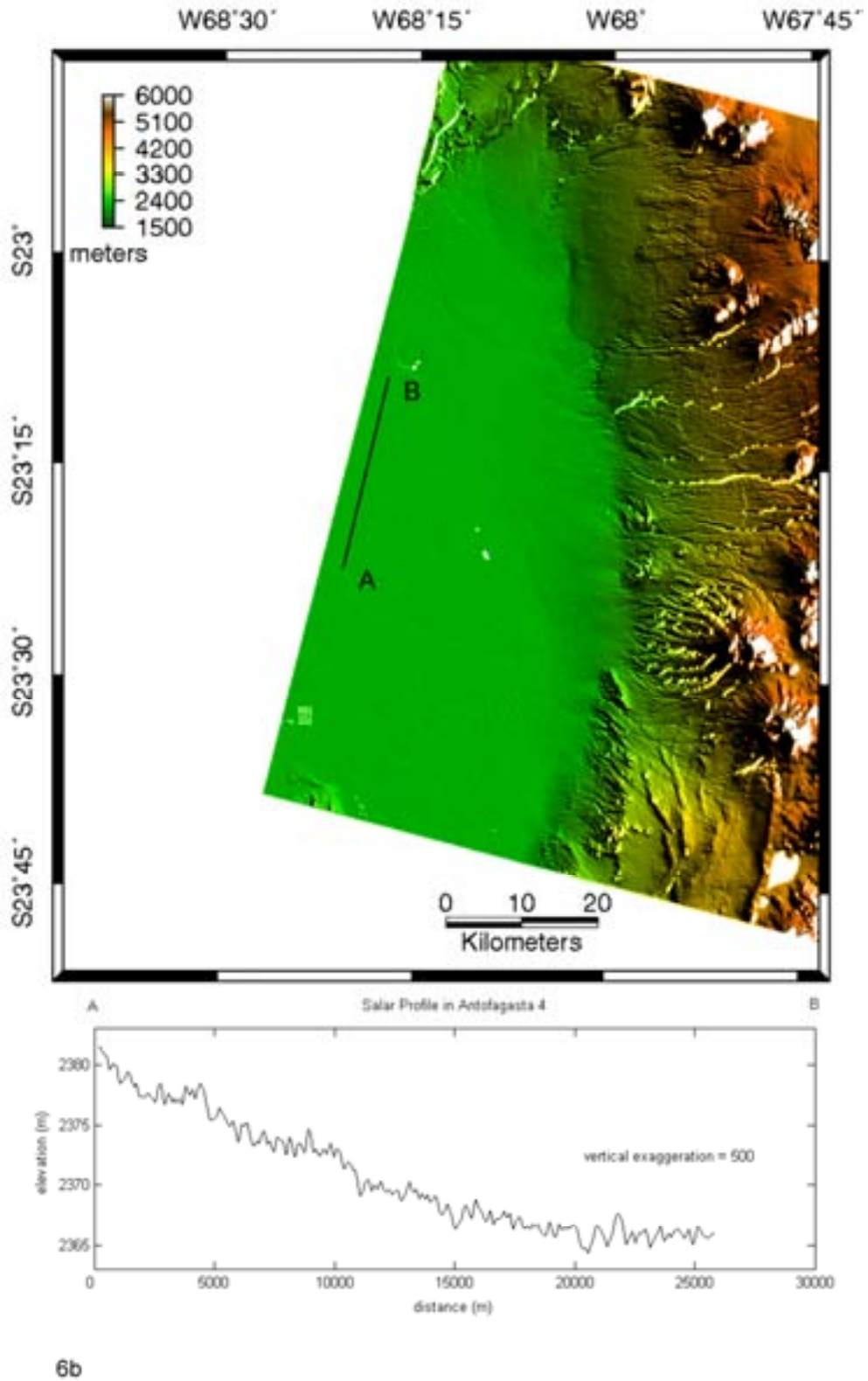

6b

set of ripples in Antofagasta 3 shows a wavelength between 2 and 3 kilometers with amplitudes on the order of 5 meters. In contrast, the signal is absent from the same profile across the Antofagasta 4 coverage, a major indication of an atmospheric effect. It should be noted that the general slopes of the two profiles do not agree and this is attributed to baseline estimation errors (Antofagasta 4 is poorly constrained), however the slope has no bearing on the presence of the ripples. Errors resulting from water vapor are more difficult to detect in zones of greater topographic relief. Stacking multiple interferograms for a study area can aid the detection of anomalous signals.

2.7 *Data By-Products*

The primary goal of using radar interferometry was to map the topography of the study area. Additional data products resulted from the interferometric processing: SAR amplitude imagery and coherence maps. The radar backscatter intensity image for every individual SAR acquisition was produced from its SLC and radiometrically calibrated. The amplitude component of the SLC was multi-looked in the same manner as the interferogram and resampled to the same geometry, resulting in a 20 meter resolution cell. An amplitude image is created for every SAR scene, which means each DEM has two amplitude images for two different times. We processed a total of 48 backscatter intensity images, an example of which is shown in Figure 2.7a for Loa 1. Coherence maps played an important role in the unwrapping phase of INSAR processing. These maps were generated by applying a gaussian weighting function and estimating the degree of coherence for each pixel between two SAR scenes. Generally, the correlation in the study area was

Figure 2.7 Other INSAR products include a) radar backscatter intensity and b) coherence. These images are both derived from the Loa 1 SAR data. The amplitude image shows a darker return from the plains of the Central Depression compared to the Coastal Cordillera to the west and the giant alluvial fans on the flanks of the western edge of the Central Andean plateau to the east. Overall, the coherence image has high correlation for a 34 day temporal baseline, particularly on the Coastal Cordillera and the slopes of the monocline. Decorrelation in the green and blue zones are limited to drainages and steep canyons.

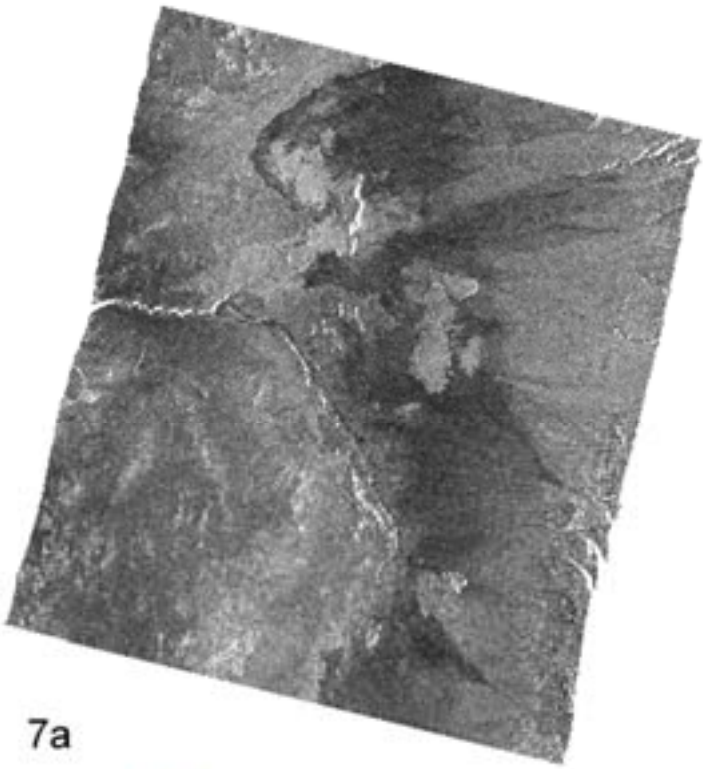

7a

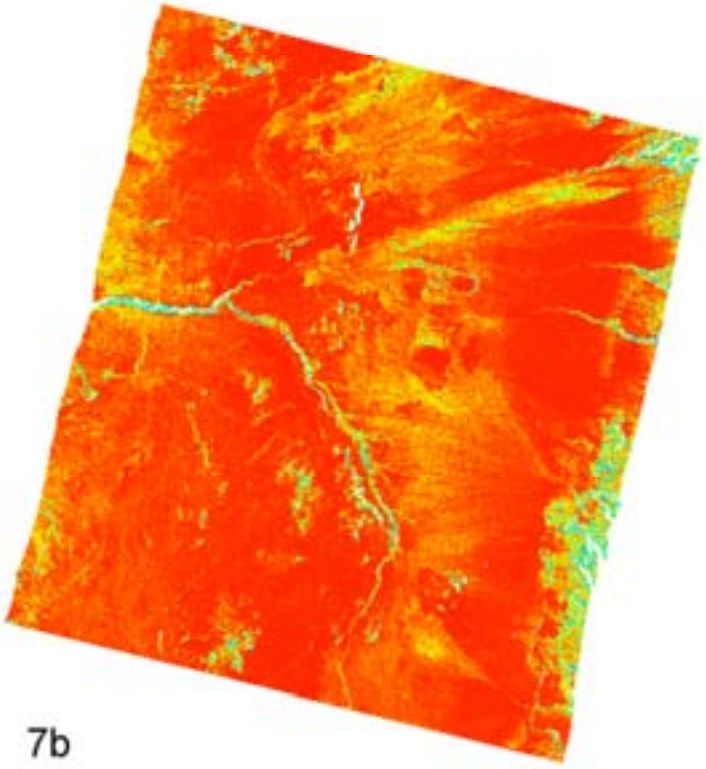

7b

high, although small patches of decorrelation resulted from factors discussed above. Coherence images can help identify surfaces undergoing change within the timespan of the temporal baseline. Two SLCs are required to calculate a coherence map and our study generated 24. The coherence image for Loa 1 is given in Figure 2.7b.

2.8 *Summary*

We have created an interferometrically-derived DEM extending from 18° 30' S to 26° S, from the west coast of Chile to the western edge of the Altiplano plateau of the Central Andes. The horizontal and vertical resolutions are 20 and 2-3 meters, respectively. The absolute vertical resolution of the DEM averages 32 meters for 24 SAR footprints. Coherence over the dataset is good to excellent and the digital topography is 99.1% complete. Data dropout zones result from radar shadow and significant surface change between radar acquisitions. Other data generated as a result of the INSAR processing include radar backscatter intensity images and coherence maps.

REFERENCES

Curlander, J. C. and McDonough, R. N., 1991, Synthetic Aperture Radar: Systems and Signal Processing, New York, John Wiley and Sons, Inc.

Elachi, C., 1987, Introduction to the Physics and Techniques of Remote Sensing, New York, John Wiley and Sons, Inc.

Hanssen, R. F., 2001, Radar Interferometry: Data Interpretation and Error Analysis, Boston, Kluwer Academic Publishers.

Lewis, A. J. and Henderson, F. M., 1998, Radar Fundamentals: The Geoscience Perspective. Principles and Applications of Imaging Radar: Manual of Remote Sensing. F. M. Henderson and A. J. Lewis. New York, John Wiley and Sons, Inc. 2: 131-181.

Madsen, S. N. and Zebker, H. A., 1998, Imaging Radar Interferometry. Principles and Applications of Imaging Radar: Manual of Remote Sensing. F. M. Henderson and A. J. Lewis. New York, John Wiley and Sons, Inc. 2: 359-380.

Raney, R. K., 1998, Radar Fundamentals: Technical Perspective. Principles and Applications of Imaging Radar: Manual of Remote Sensing. F. M. Henderson and A. J. Lewis. New York, John Wiley and Sons, Inc. 2: 9-130.

Zebker, H. A. and Goldstein, R., 1986, Topographic mapping from interferometric synthetic aperture radar observations, Journal of Geophysical Research 91: 4993-5001.

Zebker, H. A. and Villasenor, J., 1992, Decorrelation in interferometric radar echoes, IEEE Transactions on Geoscience and Remote Sensing 30(5), 950-959.

Zebker, H. A., Werner, C. L., Rosen, P. A., Hensley, S., 1994a, Accuracy of topographic maps derived from ERS-1 interferometric radar, IEEE Transactions on Geoscience and Remote Sensing, 32(4), 823-836.

Zebker, H. A., Rosen, P. A., Hensley, S., 1997, Atmospheric effects in interferometric synthetic aperture radar surface deformation and topographic maps, Journal of Geophysical Research 102(B4), 7547-7563.

CHAPTER 3

EXAMINATION OF CENOZOIC SURFACE FAULTING IN THE COASTAL CORDILLERA FROM ARICA (18° 30' S) TO LA SERENA (30° S), NORTHERN CHILE

Surface faulting in the forearc of northern Chile is extensive. This is evident in geologic and topographic maps, satellite imagery, and especially the 20-meter DEM (Chapter 2) of the region. A substantial fraction of the faulting is controlled by the AFS, which spans all but the northern 2 degrees of latitude in our study area. The surface faulting influences the morphology of the Coastal Cordillera, particularly north of 21.5º S where large block faults dominate the landscape. Faulting patterns are clues into the forces that shaped the region. Understanding these forces is a key component of reconstructing the dynamics of the tectonic setting.

In this chapter, we systematically survey the DEM for scarps with a youthful appearance and generate a fault scarp map of the forearc. Only the portion of the DEM overlapping the Coastal Cordillera is used in this study (Figure 3.1). Figure 3.2 gives a more detailed presentation of the area in 2-degree increments of latitude. We examine the scarp map and the statistics of the measured scarp properties for any significant trends.

Figure 3.1. Coverage of the data used for this study (color) superimposed on the GTOPO 30 topography (grayscale). The data is a merge of the 20-meter DEM and the Cornell 90-meter digital topography.

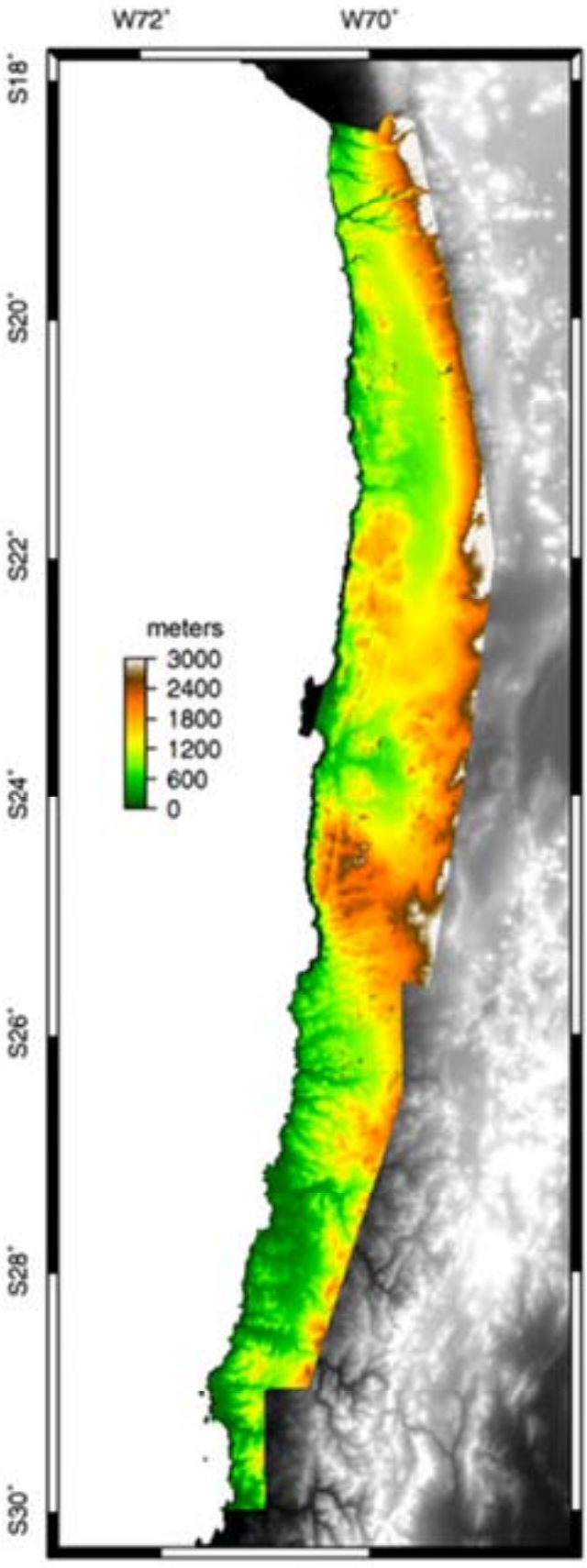
W72°
W70°
S18°
S20°
S22°
S24°
S26°
S28°
S30°
meters
3000
2400
1800
1200
600
0

Figure 3.2. Detailed images of the 20-meter DEM and 90-meter Cornell topography mosaic spanning: a) 18° S to 20° S b) 20° S to 22° S c) 21° 30'S to 23° 30'S d) 23° S to 25° S e) 25° S to 27 °S f) 26° 30'S to 28° 30'S g) 28° S to 30° S. White gaps are data dropout zones and sun shading is from the northeast at a 45° elevation. Datum is WGS84 in TMAndes custom projection. Artifacts from scene boundaries appear in Figures 3.2b and 3.2e (refer to scene boundaries in Figure 2.2).

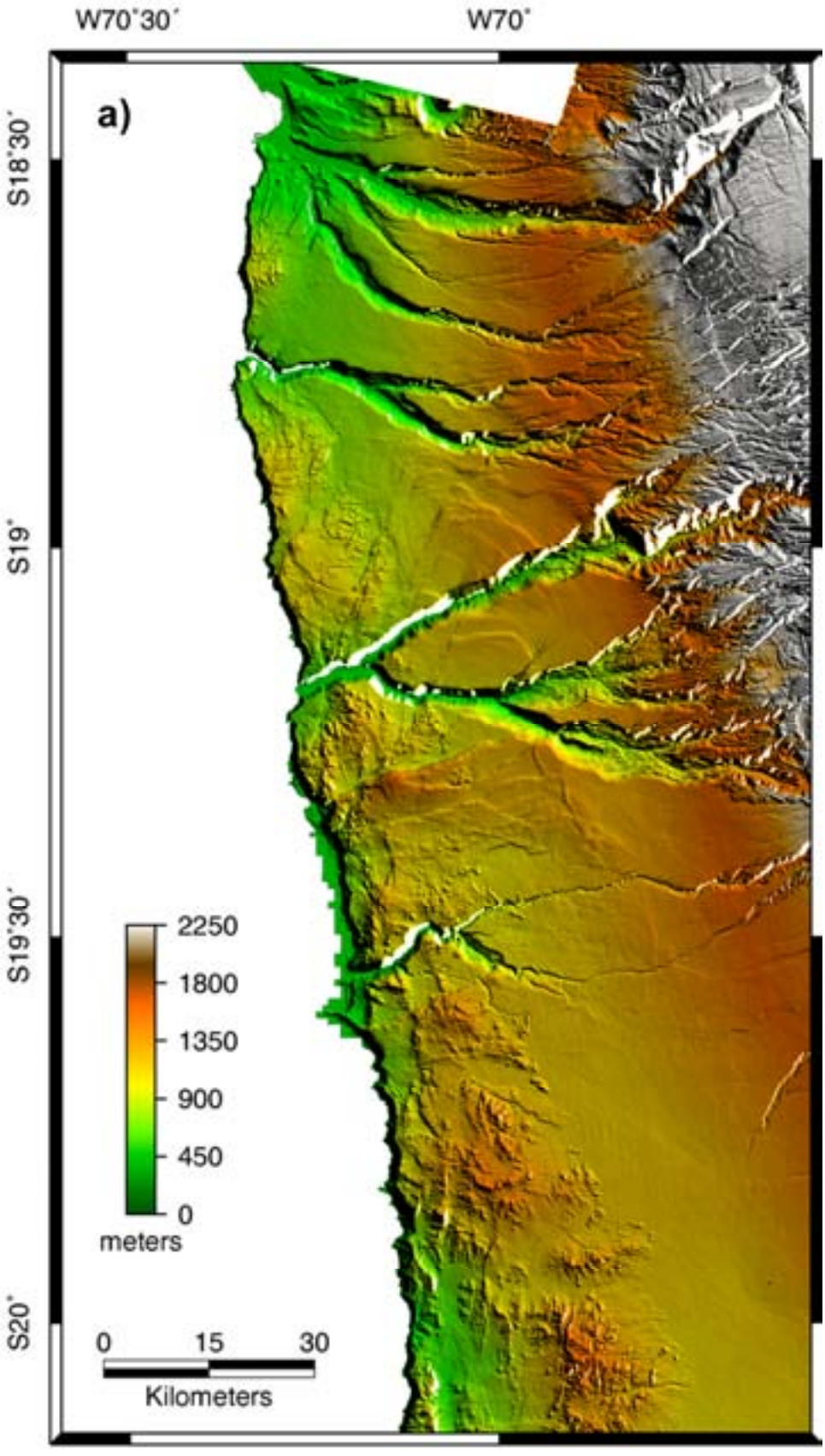
W70°30′
W70°
a)
S18°30′
S19°
S19°30′
S20°
2250
1800
1350
900
450
0
meters
0
15
30
Kilometers

Figure 3.2 (Continued)

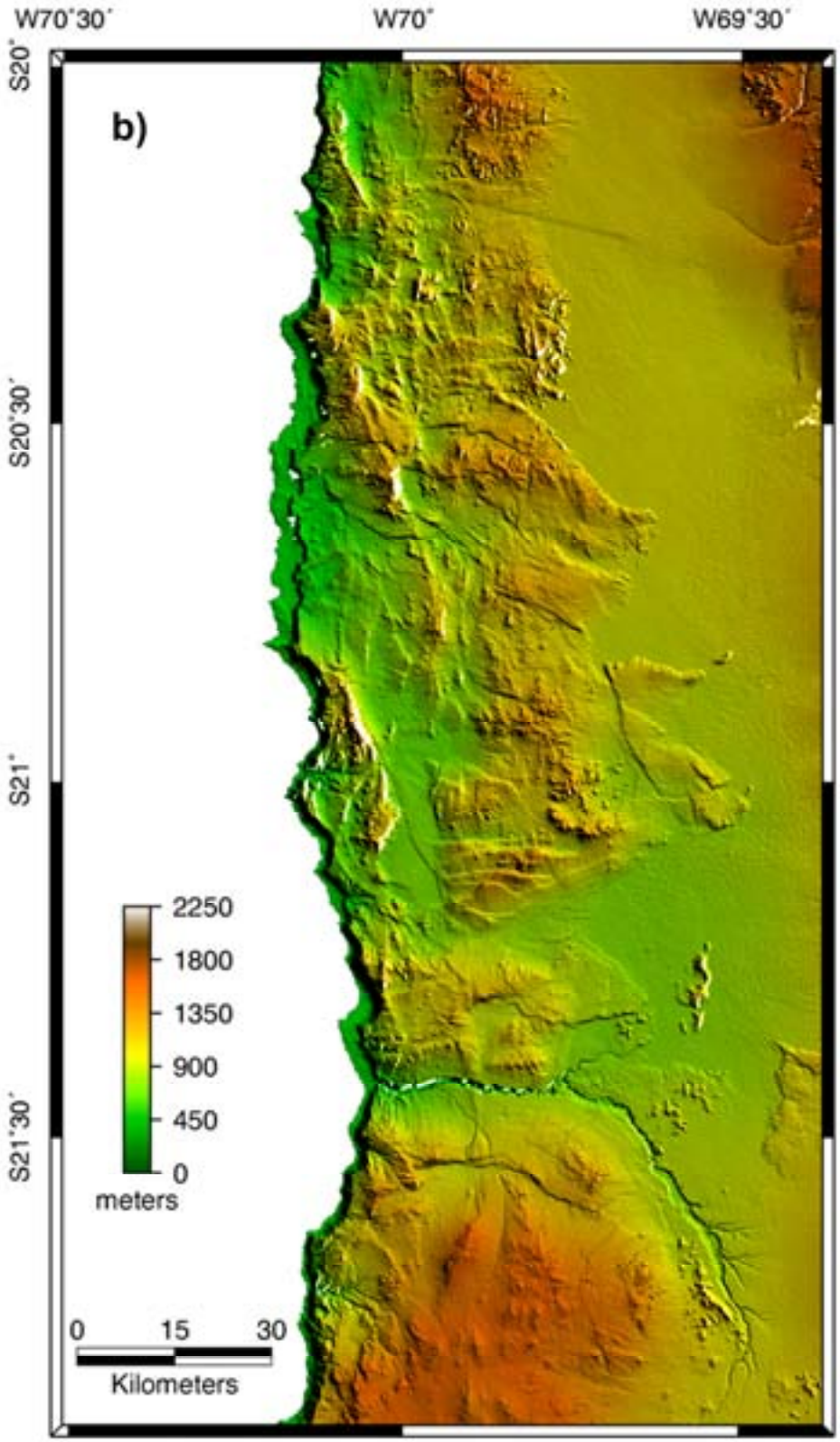

Figure 3.2 (Continued)

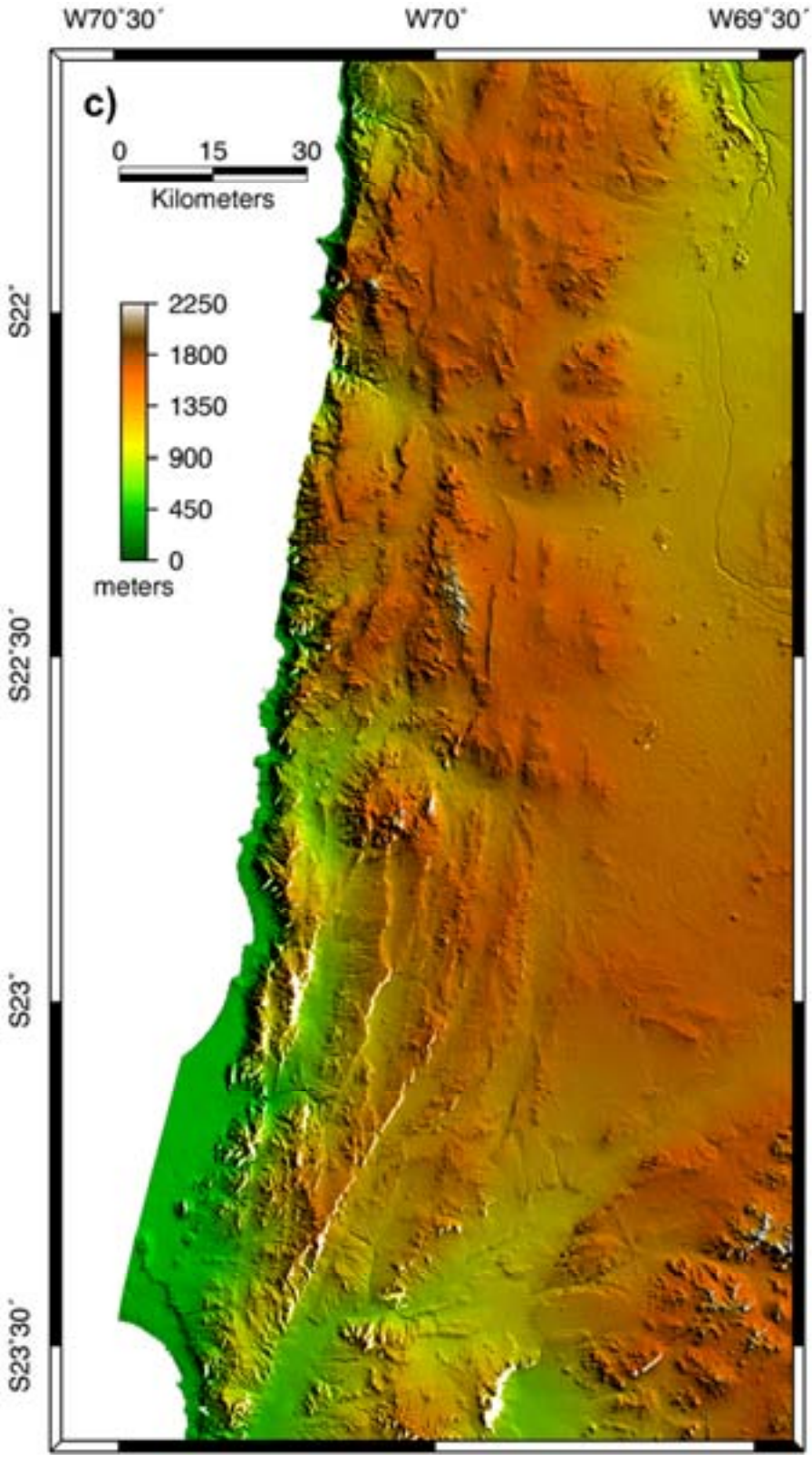

Figure 3.2 (Continued)

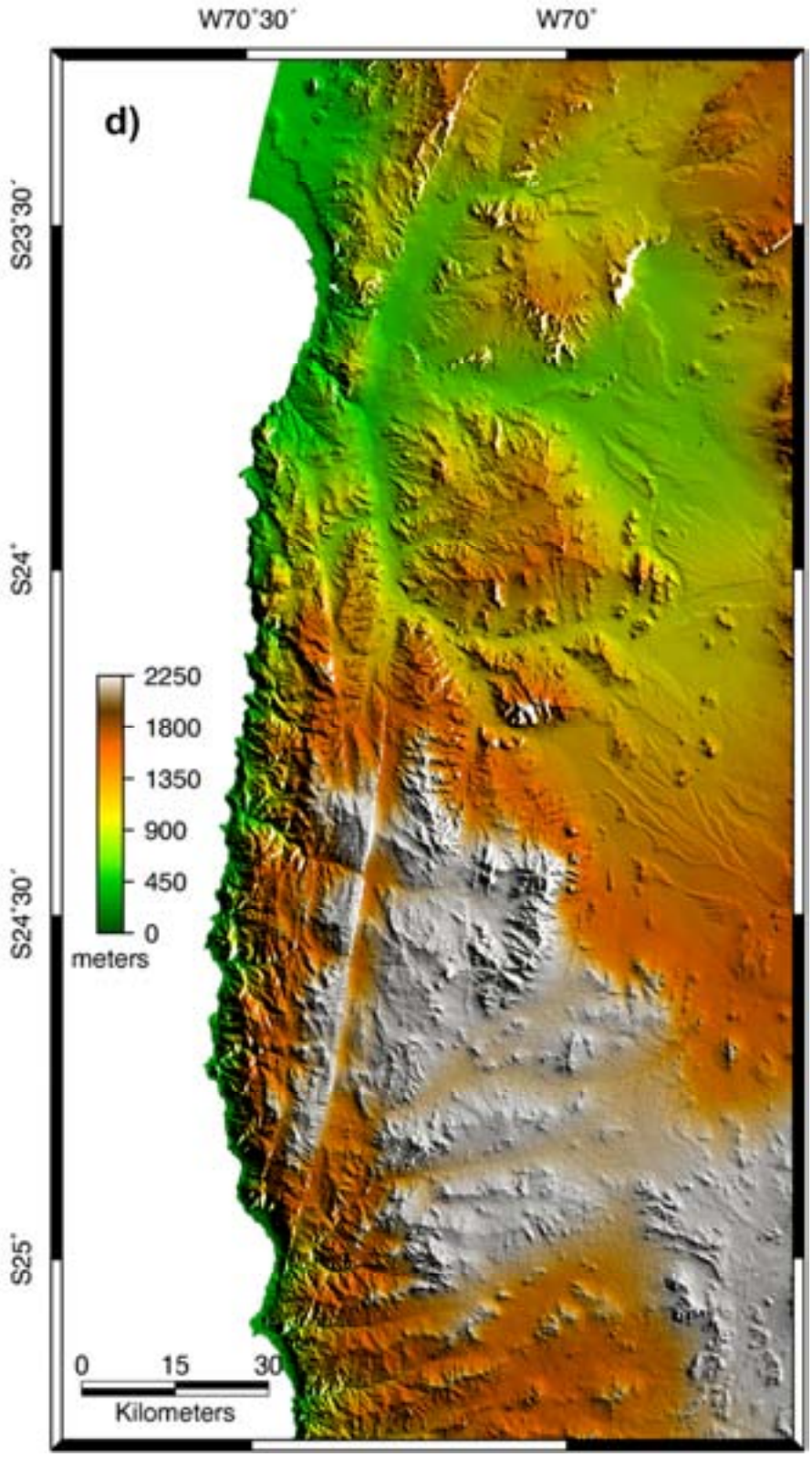

Figure 3.2 (Continued)

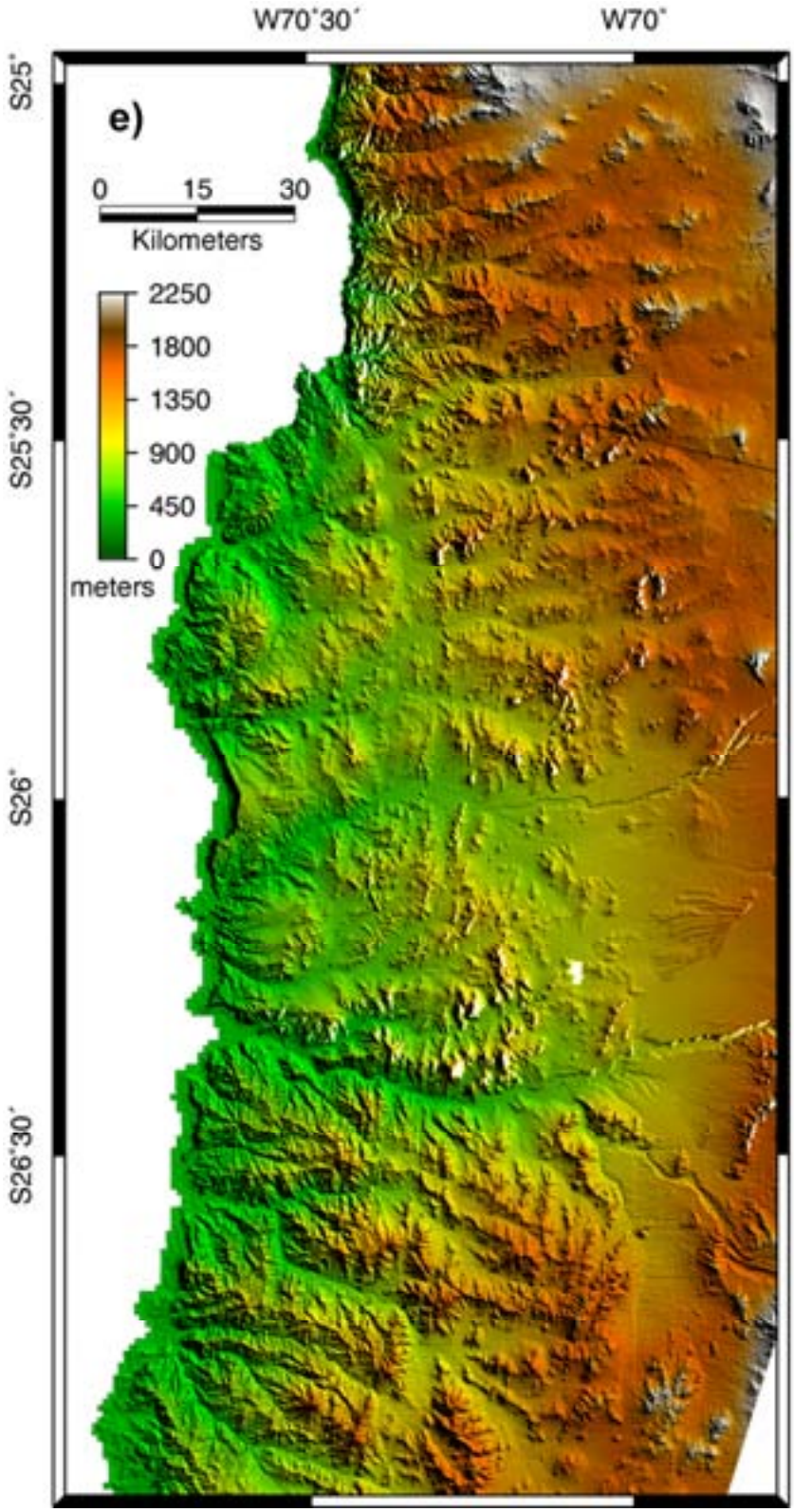

Figure 3.2 (Continued)

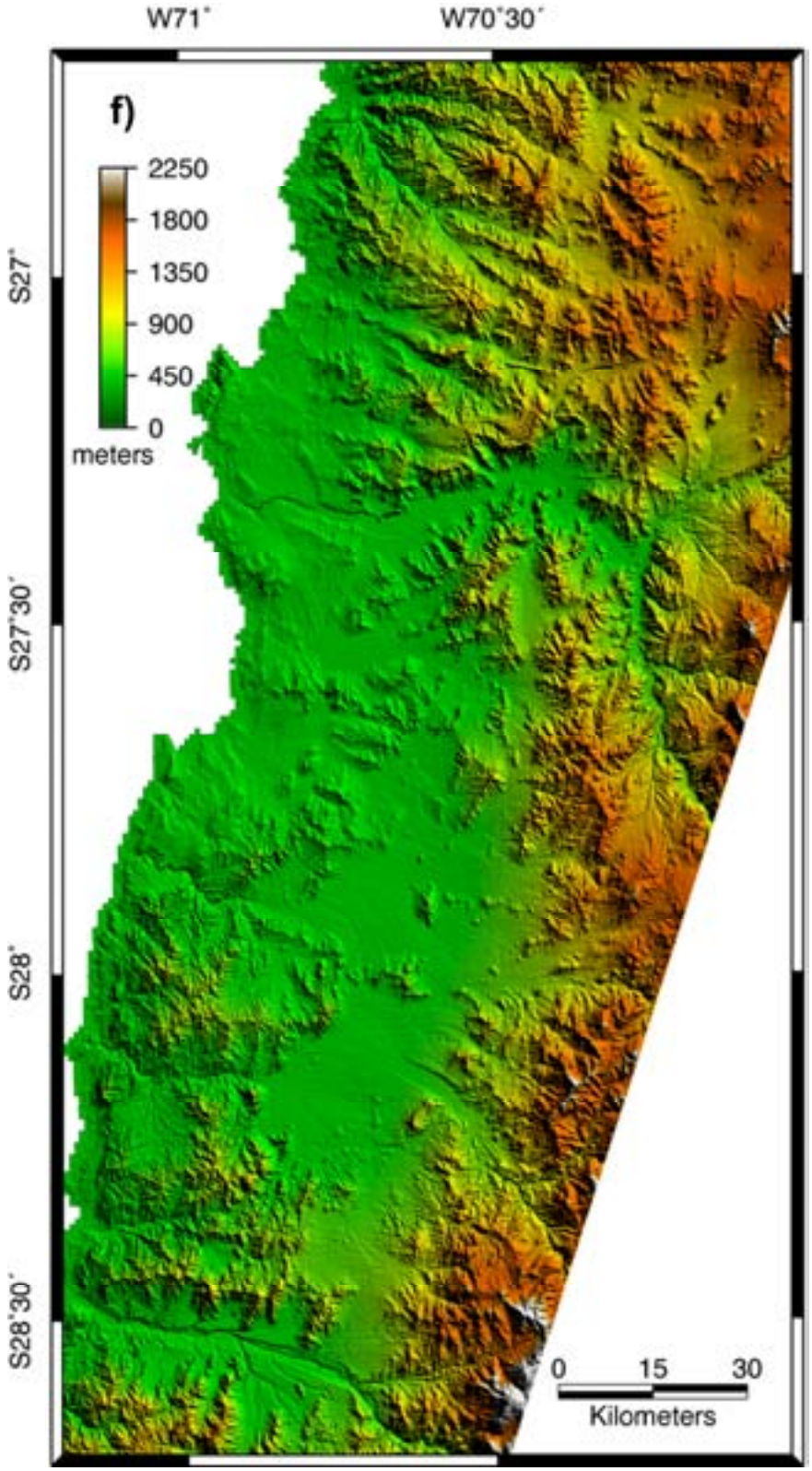

Figure 3.2 (Continued)

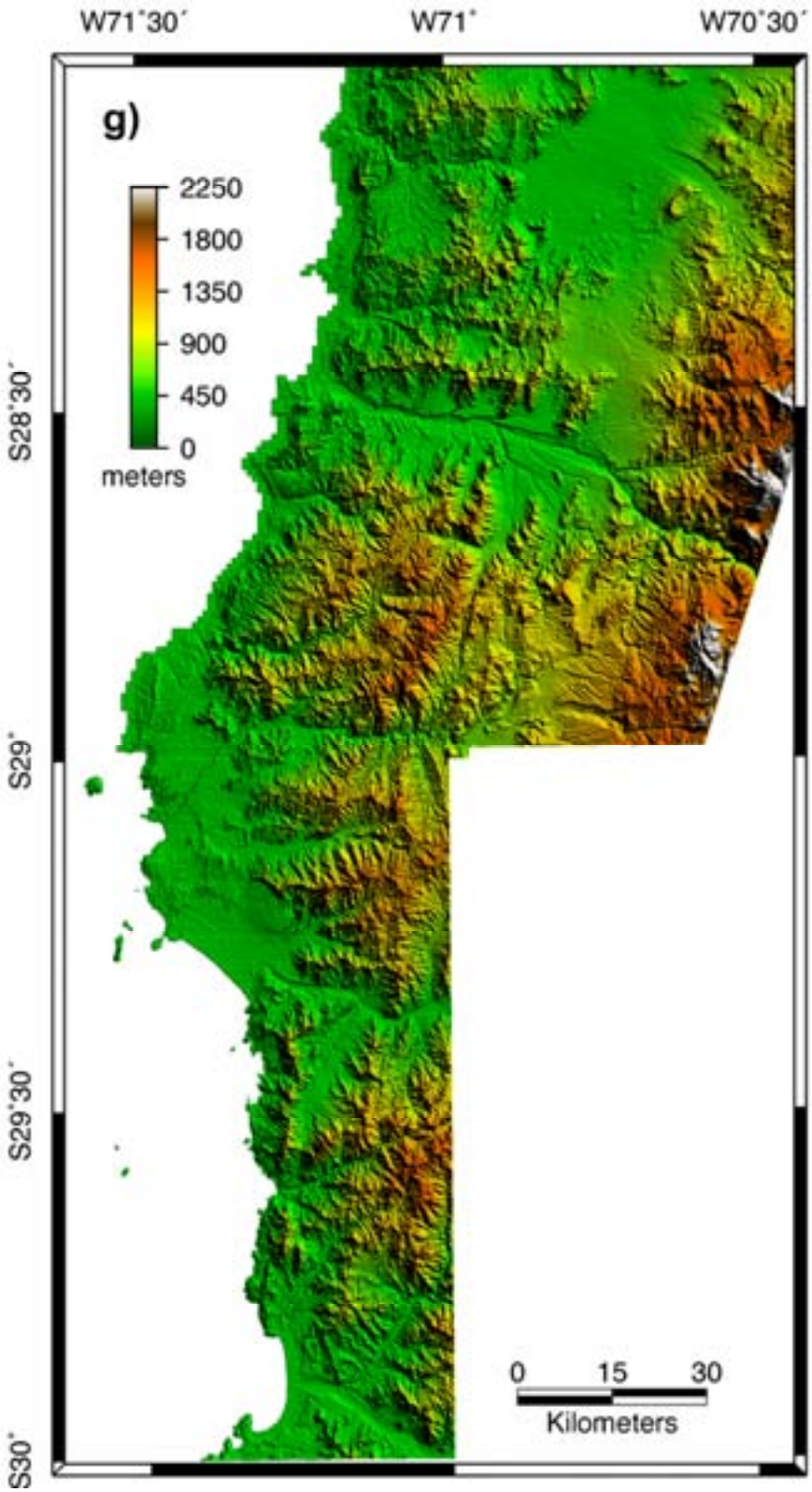

3.1 *Fault Map*

We created a fault map (Figure 3.3) in which we attempt to identify prominent and youthful looking fault scarps in the digital topographic dataset from Arica (18° 30' S) to La Serena (30° S). Scarp selection was based on the following criteria: 1) a minimum 20-meter vertical offset 2) sharpness of profile and 3) a traceable linear feature. The selection of a 20-meter minimum vertical offset is based on the relative vertical resolution (2-3 meters), which places 20 meters at the 5 to 7σ significance level, to ensure that we do not erroneously identify scarps close to the vertical resolution limit of the 20-meter DEM. Qualifying scarps were identified on shaded relief images of the DEM in ERMapper. Different sun-shade angles were applied to examine all orientations of scarps. For each scarp, we measured scarp profiles along the length of the fault at approximately 200 m intervals, to identify the maximum vertical offset on the fault (barring any anomalous topographic highs), and to find a representative shape in determining sharpness of profile. If the profile was significantly degraded, we assumed the scarp was old considering the erosional regime within the Atacama Desert, and rejected it from the qualifying group. Finally, the trace of the fault scarp had to be relatively linear and traceable. Obliteration of a candidate by drainages or concentrated degradation were primary reasons to discard a scarp. In total we identified 310 fault scarps, 24 of which were red-flagged (see below).

Figure 3.4 contains more detailed views of the fault map shown in Figure 3.3. The green lineaments are those faults that meet the criteria discussed above. Red lines mark fault-line scarps of the AFS that do not meet all of the outlined

Figure 3.3: Fault scarp map over Coastal Cordillera. Left panel contains all traces over the topography, middle panel is traces only, and the right panel is topography only. Green traces are the fault scarps that have a continuous scarp, maximum offset greater than 20 meters and youthful looking scarp profile. Red fault traces are highlighted in Table 3.1 and do not meet the criteria of the search.

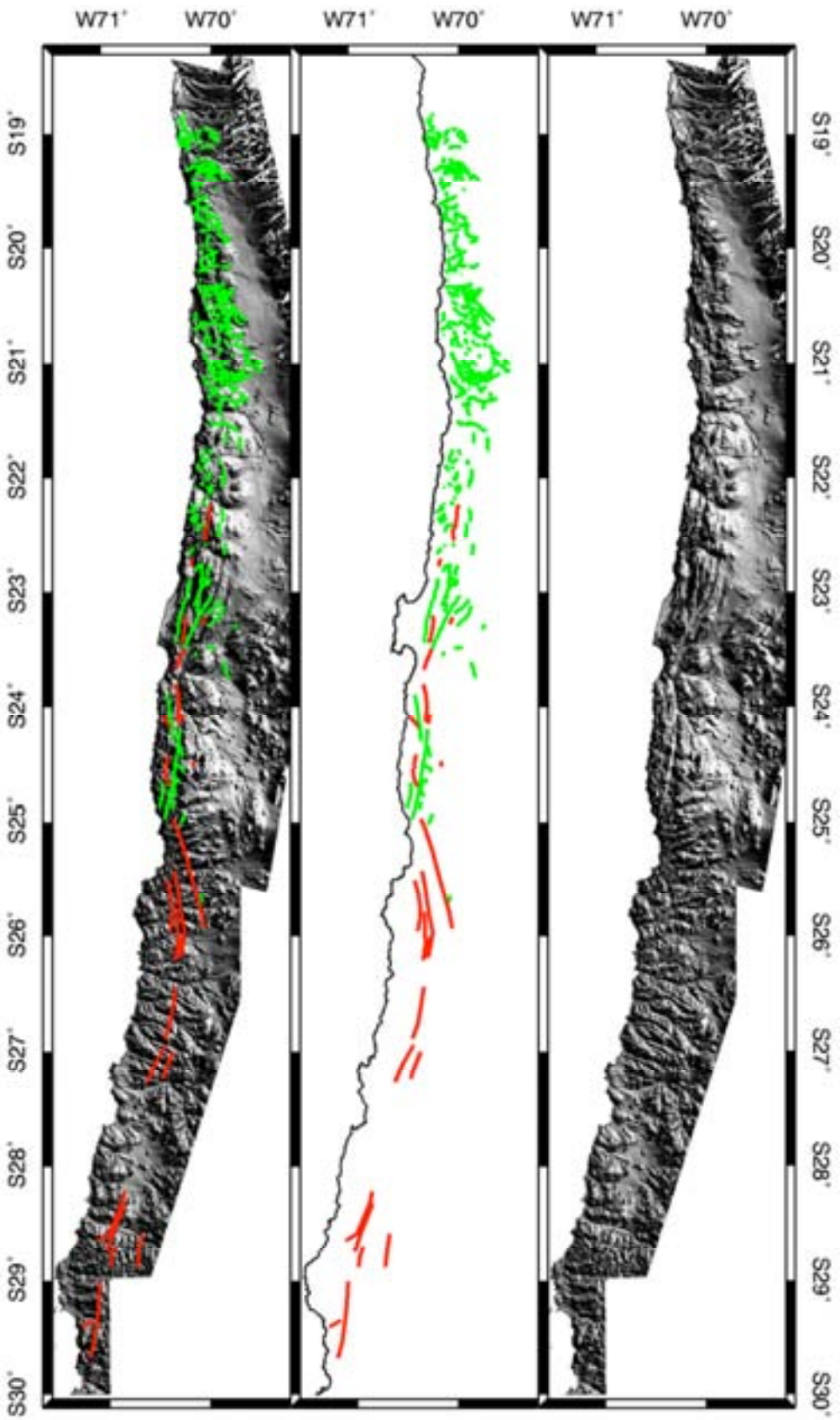
W71°
W70°
W71°
W70°
W71°
W70°
S19°
S20°
S21°
S22°
S23°
S24°
S25°
S26°
S27°
S28°
S29°
S30°
S19°
S20°
S21°
S22°
S23°
S24°
S25°
S26°
S27°
S28°
S29°
S30°

Figure 3.4. Detailed fault map sections overlain on grayscale sun-shaded (elevation 45° from the northeast) topography. Each segment corresponds to the topography displayed in Figure 3.2: a) 18° S to 20° S b) 20° S to 22° S c) 21° 30'S to 23° 30'S d) 23° S to 25° S e) 25° S to 27 °S f) 26° 30'S to 28° 30'S g) 28° S to 30° S. Projection is custom TMAndes, datum is WGS84.

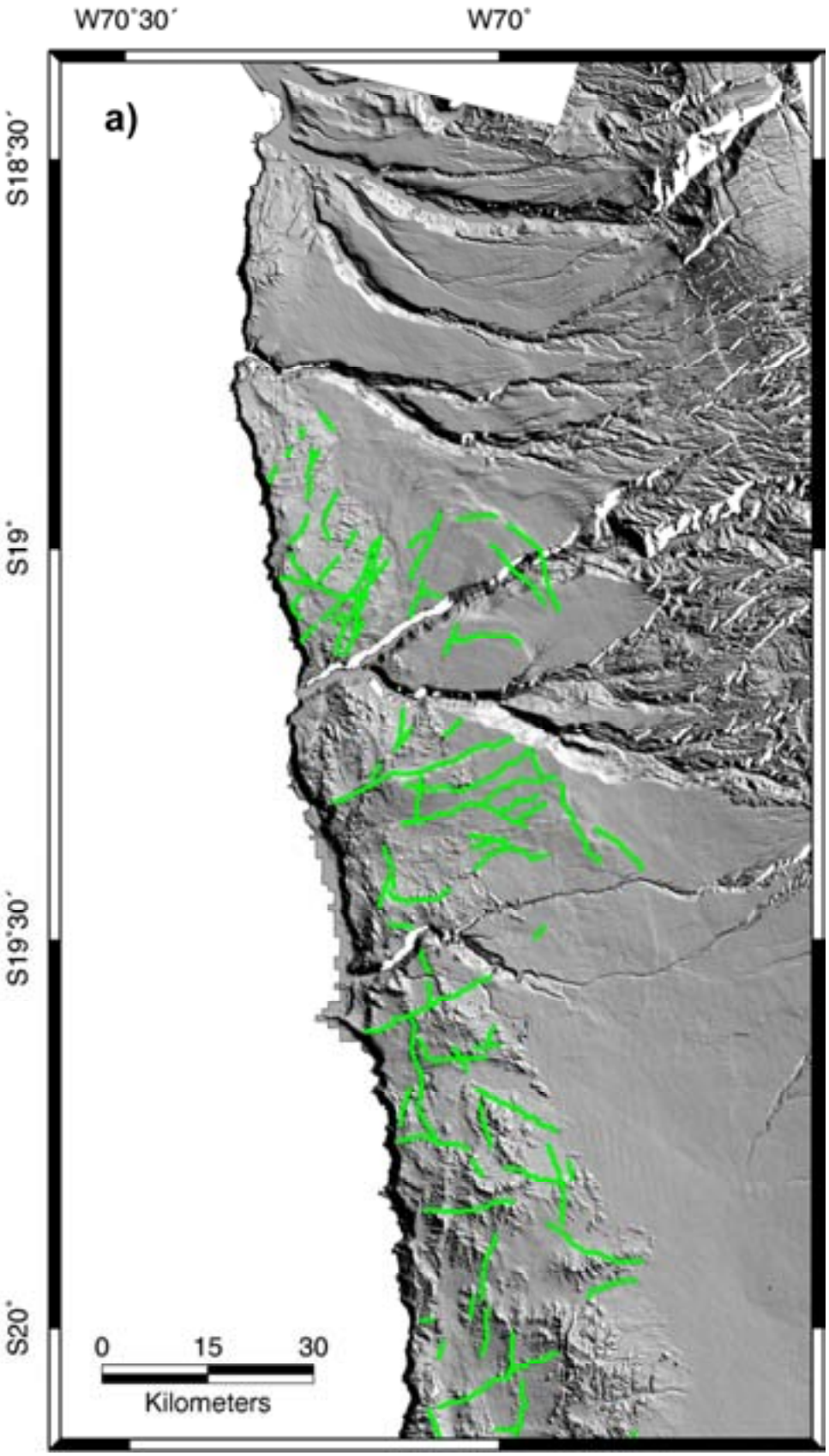
W70°30´
W70°
a)
S18°30´
S19°
S19°30´
S20°
0
15
30
Kilometers

Figure 3.4 (Continued)

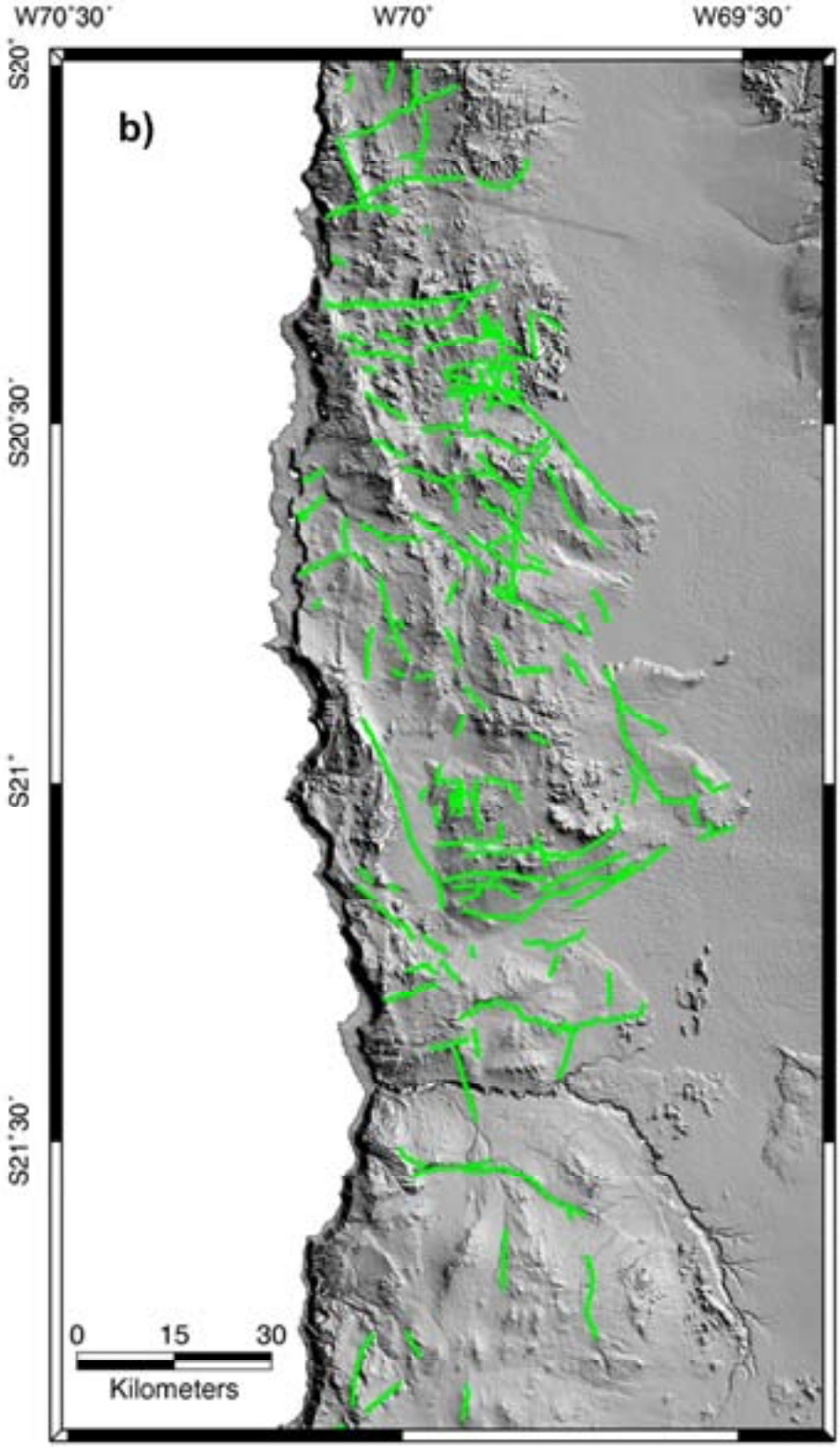

Figure 3.4 (Continued)

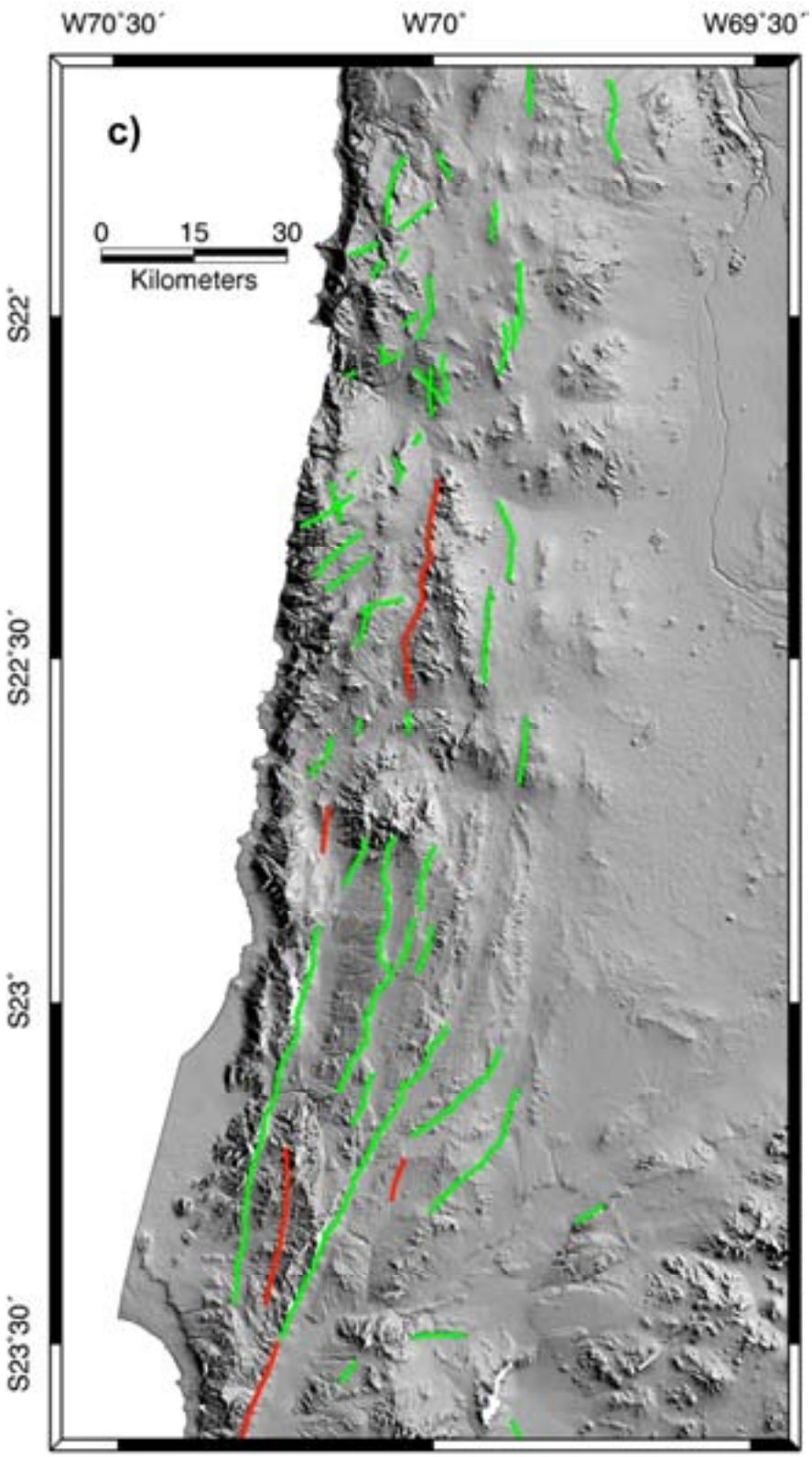

Figure 3.4 (Continued)

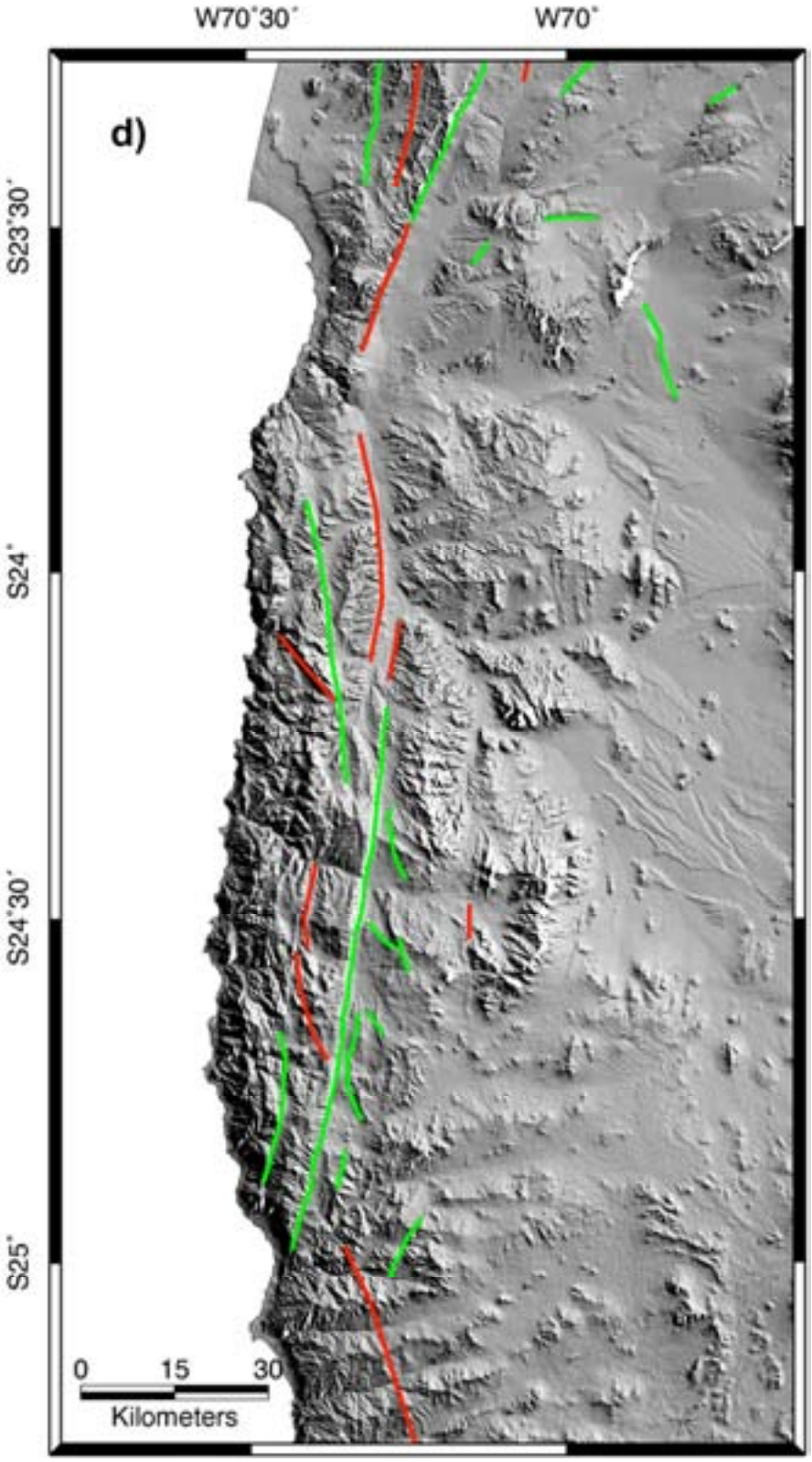

Figure 3.4 (Continued)

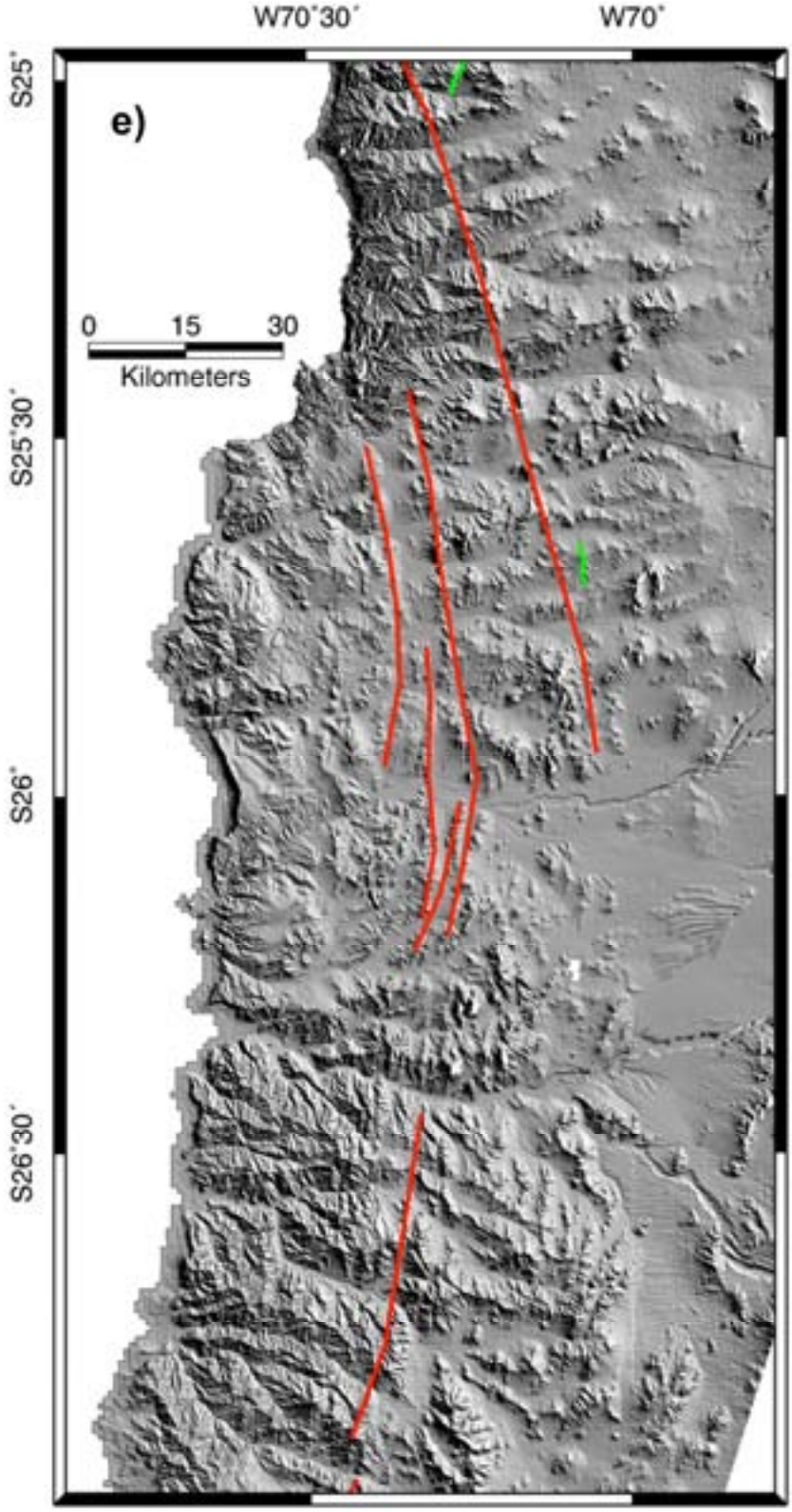

Figure 3.4 (Continued)

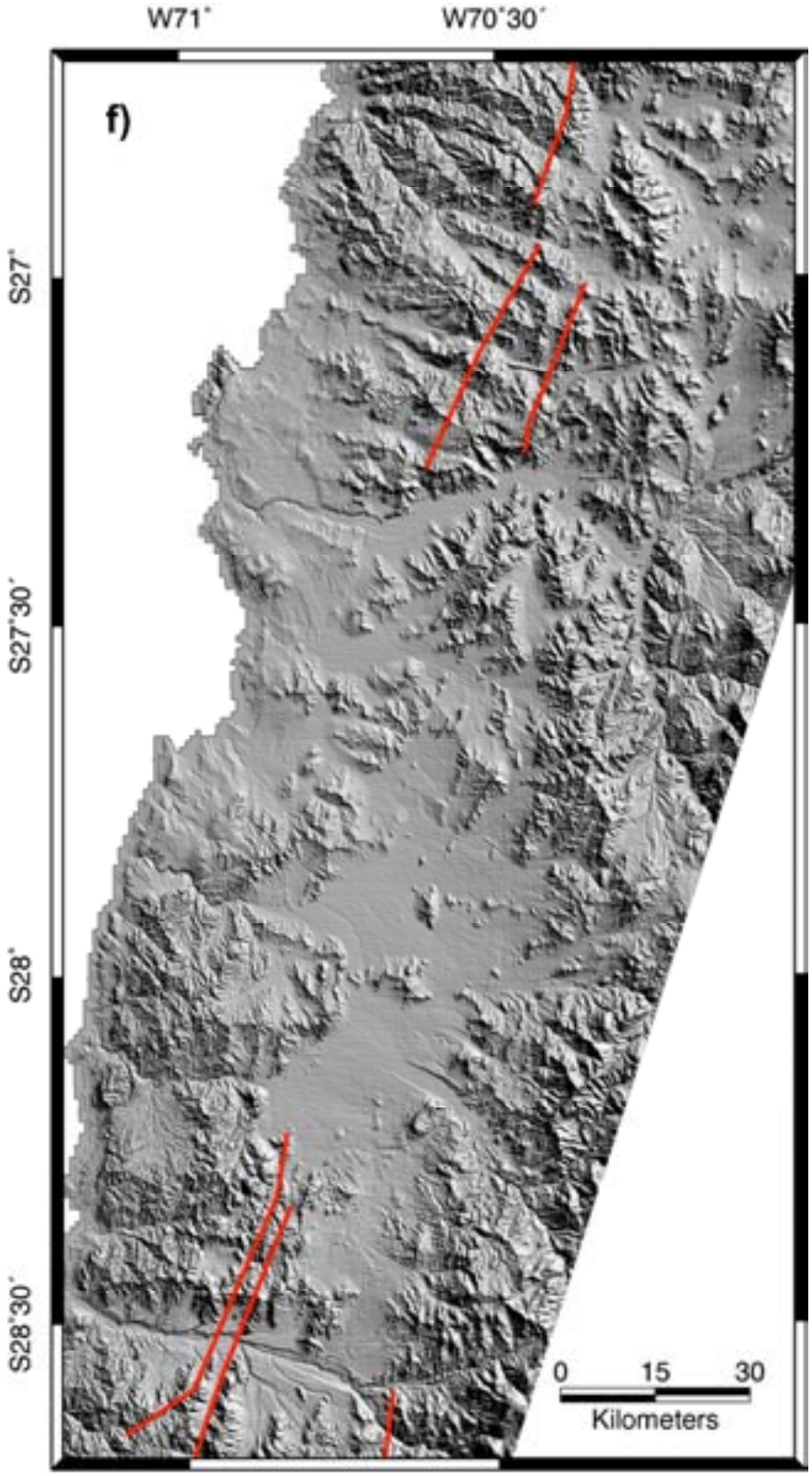

Figure 3.4 (Continued)

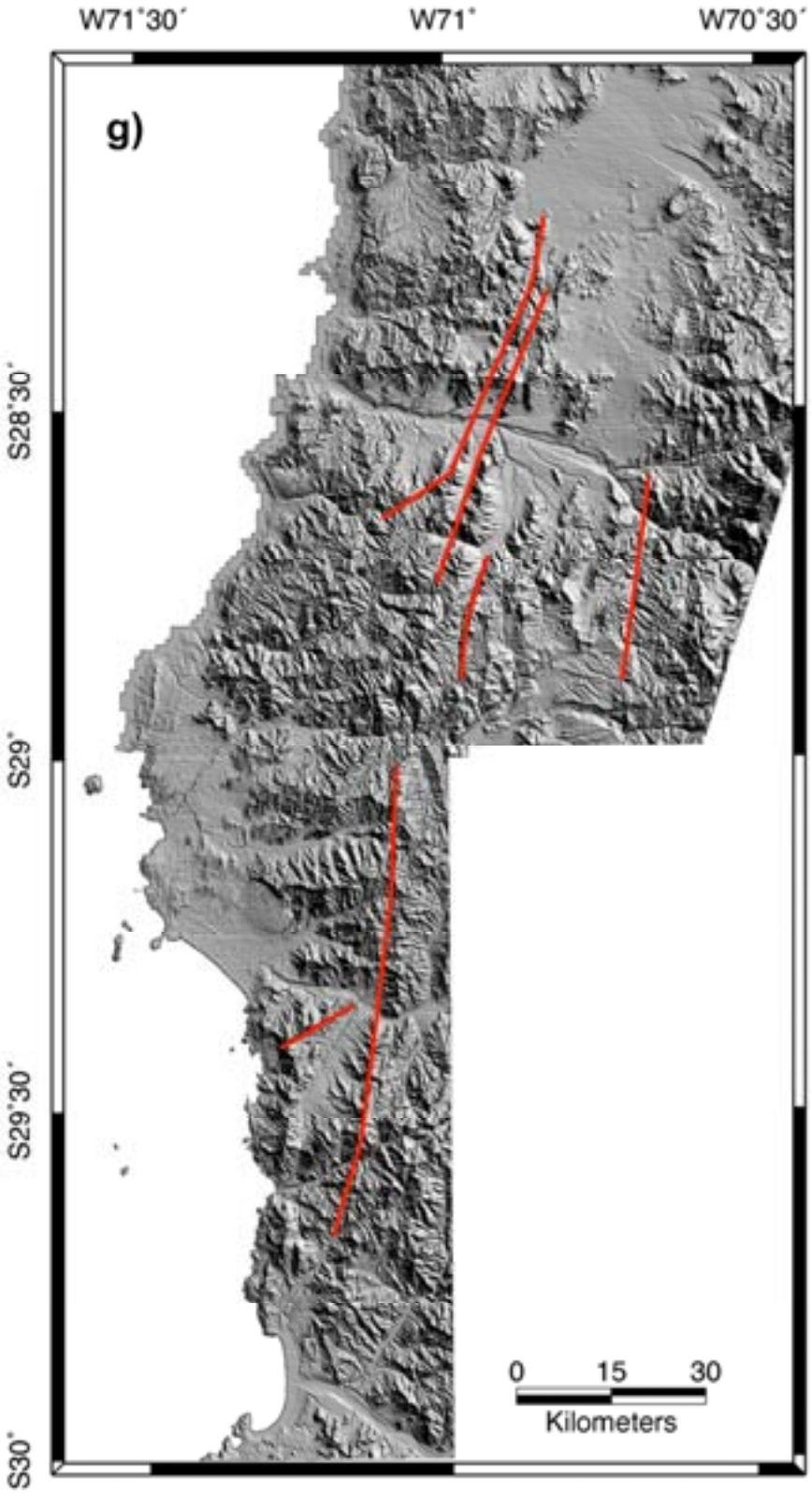

criteria, and whose scarps are apparently older and have been degraded and dissected by erosion. Although not included in the analysis, these red faults are listed and mapped for their obvious trace and for their extent in the south. Table 3.1 lists the fault scarps identified in the fault map and their measured properties in order of decreasing northing. The properties are: fault center point easting, northing, latitude, and longitude, maximum measured vertical offset, overall trend, trace length, and direction of downside block. The highlighted scarp entries represent the red traces in the fault map.

A handful of scarps have maximum offsets of slightly less than 20 meters because the measured maximum offset coincided with topographic highs. In these cases, the representative profile was offset to avoid contamination by the local topography. By the nature of the search criteria, we exclude strike-slip faulting unless a qualifying scarp was produced as a result of dip-slip motion. However, the majority of field investigations along the AFS suggest that significant strike-slip motions in the late Cenozoic are essentially absent from the AFS history with the exception of dextral motions on and near the Salar Grande. Although the digital topography permits the assessment of a region over 1000 kilometers long at a 20-meter resolution, this study is still limited by spatial resolution; the dataset is unable to resolve many of the smaller faults that record late Cenozoic activity, particularly Recent activity, in the Coastal Cordillera that field studies have identified (Delouis et al., 1998; González et al., 1999; González et al., 2003).

Table 3.1 Fault Scarp Coordinates and Measured Profiles

Easting (m)	Northing (m)	Latitude (º)	Longitude (º)	Offset (m)	Trend (º)	Trace Length (m)	Downside
1975802.18	7917051.00	18:50:17.80S	70:13:46.87W	34	-36	3506	SW
1971985.88	7915649.58	18:51:03.22S	70:15:57.35W	30	7	1011	W
1972303.06	7915534.44	18:51:06.98S	70:15:46.52W	70	31	1378	NW
1970336.63	7912857.26	18:52:33.99S	70:16:53.86W	74	24	1673	NW
1974157.12	7912256.08	18:52:53.73S	70:14:43.31W	44	34	2065	NW
1973148.61	7910002.50	18:54:07.01S	70:15:17.89W	69	5	7339	W
1968080.72	7909835.60	18:54:12.18S	70:18:11.14W	48	28	2757	NW
1976224.52	7905372.21	18:56:37.79S	70:13:32.95W	70	27	4460	NW
1997112.78	7903656.11	18:57:34.12S	70:01:38.73W	35	84	5804	N
1972147.01	7901733.62	18:58:35.99S	70:15:52.56W	113	35	5008	NW
1975633.16	7901454.60	18:58:45.23S	70:13:53.35W	20	-24	2584	SW
1988521.48	7900810.15	18:59:06.60S	70:06:32.58W	44	46	3838	NW
1979360.01	7900775.58	18:59:07.47S	70:11:45.91W	95	31	2753	NW
1989999.26	7899864.39	18:59:37.40S	70:05:42.06W	141	24	10570	NW
1982625.26	7898109.53	19:00:34.32S	70:09:54.32W	81	16	6436	NW
2006473.28	7896608.01	19:01:23.40S	69:56:18.56W	35	-27	15391	NE
1975978.49	7896404.75	19:01:29.54S	70:13:41.76W	41	40	4824	NW
1972003.64	7895980.57	19:01:43.16S	70:15:57.76W	39	-39	5551	SW
2003044.04	7895267.85	19:02:07.03S	69:58:15.86W	28	-42	11835	NE
1980008.45	7893962.69	19:02:49.15S	70:11:23.99W	65	37	16866	NW
1975454.66	7893184.05	19:03:14.31S	70:13:59.83W	63	-78	13375	NNE
1990585.99	7892642.43	19:03:32.38S	70:05:22.11W	40	-75	3131	NNE
1988702.29	7892309.34	19:03:43.19S	70:06:26.57W	29	19	5980	NW
1979983.53	7891916.20	19:03:55.74S	70:11:24.92W	132	24	16183	WNW
1971387.87	7891794.16	19:03:59.34S	70:16:19.04W	55	36	2478	NW
1971427.79	7889718.41	19:05:06.87S	70:16:17.79W	72	-40	2198	SW
1977819.19	7889708.67	19:05:07.48S	70:12:39.07W	22	7	1158	W
1979916.35	7889160.43	19:05:25.39S	70:11:27.32W	93	17	10725	WNW
1977008.94	7889098.04	19:05:27.31S	70:13:06.82W	15	28	1646	WNW
1980315.46	7887792.05	19:06:09.93S	70:11:13.71W	43	24	2927	NW
1973137.18	7887272.70	19:06:26.53S	70:15:19.41W	35	41	3475	NW
1998411.27	7886786.86	19:06:42.97S	70:00:54.38W	56	91	10426	N
1993370.48	7886188.36	19:07:02.41S	70:03:46.92W	37	21	4866	NW
1986331.59	7874062.32	19:13:36.80S	70:07:48.16W	73	7	5024	W
1993502.69	7873675.99	19:13:49.50S	70:03:42.54W	77	47	3790	NW
1986661.83	7872144.60	19:14:39.20S	70:07:36.89W	65	41	4380	NW

Table 3.1 (Continued)

Easting (m)	Northing (m)	Latitude (º)	Longitude (º)	Offset (m)	Trend (º)	Trace Length (m)	Downside
2005280.15	7868418.78	19:16:40.55S	69:56:59.09W	45	-25	3856	W
1989761.71	7867844.24	19:16:59.18S	70:05:50.79W	567	70	28080	NNW
1982744.28	7867629.54	19:17:05.99S	70:09:51.23W	75	31	2540	NW
2002620.73	7866233.02	19:17:51.69S	69:58:30.20W	69	70	11484	NNW
1996912.94	7865709.19	19:18:08.73S	70:01:45.78W	155	79	20701	NNW
1988672.98	7863722.61	19:19:13.25S	70:06:28.18W	10	4	6442	W
2003094.29	7863391.06	19:19:24.15S	69:58:13.96W	32	70	6165	NNW
1995447.40	7862836.18	19:19:42.19S	70:02:36.03W	50	-64	19757	NNW/NNE
2004949.63	7862039.89	19:20:08.09S	69:57:10.36W	29	60	4622	NNW
2010901.18	7859804.18	19:21:20.75S	69:53:46.33W	56	-25	13690	WSW
1998948.01	7858208.71	19:22:12.76S	70:00:36.06W	18	-78	6170	SSW
1998741.90	7857619.82	19:22:31.92S	70:00:43.13W	34	74	5498	S
2017640.27	7856858.10	19:22:56.42S	69:49:55.23W	20	-50	9494	NE
2001958.17	7856759.96	19:22:59.89S	69:58:52.87W	63	56	12618	S
1984889.02	7854279.05	19:24:20.40S	70:08:38.13W	54	-12	6518	WSW
1983726.79	7850431.06	19:26:25.56S	70:09:18.10W	106	19	4466	NW
1988920.20	7849313.45	19:27:02.05S	70:06:20.01W	57	-95	10345	N
1986251.19	7845655.16	19:29:01.01S	70:07:51.65W	127	-75	3849	NNE
2005854.86	7844664.13	19:29:33.39S	69:56:39.14W	25	44	2525	NW
1989455.48	7840262.55	19:31:56.52S	70:06:01.83W	40	-20	3791	W
1990200.66	7835970.21	19:34:16.18S	70:05:36.34W	116	-8	3646	W
1990290.18	7834182.51	19:35:14.34S	70:05:33.30W	238	65	20750	NNW
1998885.06	7830319.20	19:37:20.11S	70:00:38.28W	45	22	2716	NW
1998468.14	7828664.28	19:38:13.95S	70:00:52.60W	83	85	4058	N
1989555.07	7827995.37	19:38:35.62S	70:05:58.66W	59	-26	3600	ENE
1994292.56	7826888.85	19:39:11.69S	70:03:16.00W	99	86	8032	N
1994783.48	7826678.46	19:39:18.53S	70:02:59.14W	53	-27	4171	NE
1989048.50	7823276.69	19:41:09.12S	70:06:16.16W	214	-12	18741	W
1986728.78	7820070.02	19:42:53.39S	70:07:35.91W	80	14	5977	WNW
2003192.22	7819340.64	19:43:17.27S	69:58:10.33W	53	-61	14044	SW
1998054.47	7816999.80	19:44:33.43S	70:01:06.85W	85	-15	6796	ENE
1990958.86	7815021.22	19:45:37.73S	70:05:10.68W	94	-80	10643	N
1997005.86	7811263.07	19:47:40.06S	70:01:42.91W	75	-30	3373	WSW
2010233.98	7810848.04	19:47:53.48S	69:54:08.24W	14	-11	2964	W
2005221.10	7809926.97	19:48:23.51S	69:57:00.53W	6	-74	9103	SSW
2009123.61	7808817.64	19:48:59.55S	69:54:46.37W	12	-10	12563	W

Table 3.1 (Continued)

Easting (m)	Northing (m)	Latitude (º)	Longitude (º)	Offset (m)	Trend (º)	Trace Length (m)	Downside
1996297.16	7805185.85	19:50:57.77S	70:02:07.31W	43	83	13432	S
2013638.17	7799242.29	19:54:10.97S	69:52:10.93W	19	-66	15626	SSW
1997896.75	7797516.73	19:55:07.27S	70:01:12.35W	82	12	10211	W
2015576.89	7794750.15	19:56:37.05S	69:51:04.11W	44	70	8253	SSE
1996227.76	7791732.13	19:58:15.45S	70:02:09.80W	51	8	3276	E
1989924.31	7789746.96	19:59:19.95S	70:05:46.73W	95	72	2124	S
1998333.16	7788196.28	20:00:10.49S	70:00:57.37W	66	9	7125	E
1991937.23	7785491.00	20:01:38.44S	70:04:37.53W	15	14	2746	W
2001823.48	7785084.16	20:01:51.73S	69:58:57.23W	66	4	6506	E
2000770.39	7781505.01	20:03:48.17S	69:59:33.48W	103	64	19593	NNW
2003187.64	7776367.01	20:06:35.31S	69:58:10.22W	41	7	10627	W
2001390.57	7774248.43	20:07:44.24S	69:59:12.10W	29	86	3559	N
1992274.64	7771340.04	20:09:18.80S	70:04:26.13W	343	-22	11706	NE
2001503.12	7770896.32	20:09:33.29S	69:59:08.22W	35	78	16426	N
2016768.81	7769758.80	20:10:10.03S	69:50:22.28W	64	35	10858	NNW
1994123.53	7766312.39	20:12:02.38S	70:03:22.50W	46	87	11813	N
2003699.12	7762963.52	20:13:51.34S	69:57:52.51W	56	80	1145	S
1990021.87	7757933.82	20:16:34.88S	70:05:44.00W	35	-65	2681	NNE
1999640.07	7751668.76	20:19:58.78S	70:00:12.41W	102	85	22188	N
2008413.39	7750292.45	20:20:43.49S	69:55:09.81W	84	87	17498	NNW
2022759.03	7748845.07	20:21:30.15S	69:46:54.95W	55	-53	4140	NNE
2013309.66	7748764.57	20:21:33.09S	69:52:20.90W	23	-29	3114	WSW
2012608.68	7748378.14	20:21:45.68S	69:52:45.07W	10	-22	3002	WSW
2019935.34	7746639.06	20:22:42.03S	69:48:32.27W	179	-8	7674	W
1992510.34	7746425.58	20:22:49.29S	70:04:18.38W	30	-72	4717	S
2009279.85	7746169.71	20:22:57.59S	69:54:39.85W	123	77	11790	N
1998834.73	7746117.43	20:22:59.37S	70:00:40.20W	22	-71	5567	SSW
2015193.55	7746019.96	20:23:02.32S	69:51:15.83W	28	-10	6505	W
2015611.57	7745933.14	20:23:05.14S	69:51:01.41W	71	-62	5839	NNE
1996935.36	7743959.35	20:24:09.57S	70:01:45.74W	48	-78	10728	S
2012858.93	7742691.66	20:24:50.66S	69:52:36.29W	115	78	14096	N
2014925.13	7741552.02	20:25:27.68S	69:51:24.96W	48	91	3237	S
1995068.67	7741442.54	20:25:31.43S	70:02:50.17W	79	-76	2409	S
2017354.65	7740891.05	20:25:49.10S	69:50:01.09W	93	-22	4175	WSW
2014905.64	7740462.24	20:26:03.13S	69:51:25.60W	21	-2	2816	W
2008703.38	7740281.26	20:26:09.15S	69:54:59.64W	72	-83	4164	N

Table 3.1 (Continued)

Easting (m)	Northing (m)	Latitude (º)	Longitude (º)	Offset (m)	Trend (º)	Trace Length (m)	Downside
2012033.68	7739272.08	20:26:41.92S	69:53:04.68W	35	18	4736	WNW
2012941.94	7738515.20	20:27:06.52S	69:52:33.31W	70	-83	12225	S
2009006.14	7737674.21	20:27:33.96S	69:54:49.14W	84	85	4296	S
2016582.21	7737329.71	20:27:44.98S	69:50:27.63W	20	-12	1638	W
2013412.89	7737236.90	20:27:48.09S	69:52:17.02W	49	10	4881	WSW
2014993.88	7736182.59	20:28:22.34S	69:51:22.42W	92	-80	2559	S
1997169.34	7735741.38	20:28:36.90S	70:01:37.72W	61	-57	7721	NNE
2009611.23	7735300.18	20:28:51.17S	69:54:28.21W	22	-4	5503	E
2011052.39	7731506.61	20:30:54.55S	69:53:38.37W	124	-63	17732	S
2006964.02	7730535.20	20:31:26.22S	69:55:59.53W	37	30	1805	NW
2020994.23	7729564.56	20:31:57.42S	69:47:55.01W	37	45	4641	NNW
1997905.35	7729264.44	20:32:07.60S	70:01:12.34W	51	-63	6119	SW
2025229.76	7729035.12	20:32:14.46S	69:45:28.72W	166	-45	32586	NE
2019522.04	7726107.32	20:33:49.94S	69:48:45.71W	132	53	11029	WNW
2012574.44	7725335.12	20:34:15.28S	69:52:45.66W	30	-79	4486	S
1986315.78	7724931.94	20:34:28.36S	70:07:52.68W	43	62	3960	SSE
2004984.94	7724500.30	20:34:42.56S	69:57:07.81W	66	-80	10536	S
2014464.44	7724490.74	20:34:42.69S	69:51:40.35W	117	-50	9954	NE/SW
2008380.69	7722209.30	20:35:57.04S	69:55:10.47W	147	-42	5400	WSW
1986114.03	7720068.26	20:37:06.57S	70:07:59.79W	62	53	5473	SSE
2025734.04	7719639.16	20:37:20.08S	69:45:10.82W	41	-34	15564	NE
1984754.79	7719011.07	20:37:40.92S	70:08:46.79W	37	5	1061	ENE
1984679.27	7718482.48	20:37:59.12S	70:08:49.41W	41	68	1485	SSE
2015866.35	7718180.42	20:38:07.93S	69:50:51.72W	98	-39	10184	SW
2006204.93	7716069.91	20:39:16.78S	69:56:25.56W	48	-46	12515	SW
1991022.41	7715990.53	20:39:19.33S	70:05:10.27W	39	-3	5256	W
1997902.55	7715329.61	20:39:40.90S	70:01:12.49W	31	0	10542	SSW
2015340.66	7715038.57	20:39:50.14S	69:51:09.79W	43	64	3613	NNW
2017138.25	7714775.70	20:39:58.64S	69:50:07.65W	25	6	16930	W
1993461.49	7712152.29	20:41:24.22S	70:03:46.02W	20	-54	3902	SW
2020170.62	7712139.34	20:41:24.29S	69:48:22.74W	22	-62	2798	SSW
2011305.90	7711978.22	20:41:29.80S	69:53:29.17W	91	-53	5662	SSW
2015641.03	7711754.75	20:41:36.96S	69:50:59.31W	45	-65	14458	SW
1987626.89	7711457.14	20:41:46.73S	70:07:07.73W	75	64	8154	SSE
2016559.15	7708506.74	20:43:22.58S	69:50:27.46W	37	-48	1055	SW
2015854.85	7707406.47	20:43:58.40S	69:50:51.77W	36	-61	2998	SSW

Table 3.1 (Continued)

Easting (m)	Northing (m)	Latitude (º)	Longitude (º)	Offset (m)	Trend (º)	Trace Length (m)	Downside
2007671.08	7707356.64	20:44:00.20S	69:55:34.75W	37	25	3750	WNW
2018612.93	7705438.65	20:45:02.32S	69:49:16.33W	106	-60	10216	SSW
1986793.65	7705343.13	20:45:05.59S	70:07:36.70W	44	45	1888	NW
2030666.99	7705116.59	20:45:12.22S	69:42:19.46W	36	-24	5484	NE
2024690.03	7702815.74	20:46:27.38S	69:45:46.04W	44	-56	6291	SSW
1998120.67	7702549.13	20:46:36.64S	70:01:05.00W	67	-19	14078	ENE
1999688.45	7702289.95	20:46:45.08S	70:00:10.78W	55	-32	1621	NE
2027927.62	7702072.84	20:46:51.38S	69:43:54.02W	41	-21	4132	NE
1997851.81	7699804.07	20:48:05.93S	70:01:14.31W	38	29	743	WNW
2008088.46	7698471.40	20:48:49.23S	69:55:20.17W	24	-20	6631	ENE
1994571.54	7698018.32	20:49:04.00S	70:03:07.81W	75	5	8089	E
2015096.10	7697695.06	20:49:14.32S	69:51:17.71W	13	-24	5101	SW
2026513.75	7695375.35	20:50:29.32S	69:44:42.56W	63	-37	5313	NE
2019749.33	7695125.79	20:50:37.74S	69:48:36.61W	20	87	5591	S
1999414.35	7694697.66	20:50:52.05S	70:00:20.27W	49	-70	2242	NNE
2003519.74	7694180.69	20:51:08.85S	69:57:58.20W	57	80	3173	SSE
2011033.48	7690844.54	20:52:57.26S	69:53:38.11W	29	43	4864	NE
2037462.72	7687338.49	20:54:50.06S	69:38:23.07W	39	-60	8305	SW
2008843.59	7686464.76	20:55:19.78S	69:54:53.82W	26	21	3301	SE
2034390.04	7684328.53	20:56:28.19S	69:40:09.23W	59	-22	24612	SW
2021202.04	7684323.97	20:56:29.05S	69:47:45.87W	7	-61	3330	SSW
2005541.79	7678952.46	20:59:24.19S	69:56:48.05W	96	12	3064	WNW
2046697.79	7678123.01	20:59:49.06S	69:33:02.48W	53	-43	4811	SW
2014624.75	7677954.82	20:59:56.46S	69:51:33.42W	143	-72	4650	NNE
2007353.79	7677834.27	21:00:00.54S	69:55:45.27W	70	-82	3529	N
2036029.85	7677693.28	21:00:03.90S	69:39:11.96W	19	-43	6162	W
2048973.02	7677076.40	21:00:22.89S	69:31:43.56W	152	65	2812	SSE
2017545.93	7676138.95	21:00:55.43S	69:49:52.16W	86	-26	2508	ENE
2003174.12	7676103.71	21:00:56.87S	69:58:10.04W	34	29	2322	NW
2010195.01	7675925.63	21:01:02.57S	69:54:06.81W	36	-41	1772	NE
2007519.16	7675507.34	21:01:16.22S	69:55:39.51W	30	0	2167	E
2009019.23	7675270.49	21:01:23.90S	69:54:47.53W	41	0	5919	E
2043019.60	7674897.94	21:01:34.29S	69:35:09.59W	185	84	6199	NNW
2008150.77	7674796.79	21:01:39.33S	69:55:17.61W	63	12	4697	W
2033967.58	7674787.72	21:01:38.56S	69:40:23.18W	22	-13	563	WSW
2011170.27	7674398.89	21:01:52.21S	69:53:32.99W	71	-9	8258	W

Table 3.1 (Continued)

Easting (m)	Northing (m)	Latitude (º)	Longitude (º)	Offset (m)	Trend (º)	Trace Length (m)	Downside
2044999.95	7673063.26	21:02:33.79S	69:34:00.81W	47	-15	4384	WSW
2005125.45	7672675.32	21:02:48.37S	69:57:02.40W	208	-10	3156	W
2033142.30	7671984.18	21:03:09.80S	69:40:51.58W	18	-27	1680	SW
2000370.12	7671711.01	21:03:19.77S	69:59:47.17W	51	-23	32270	NE/SW
2047387.76	7671180.23	21:03:34.83S	69:32:37.89W	95	-37	1766	SW
2015098.45	7670375.53	21:04:02.98S	69:51:16.77W	43	-7	2312	ENE
2048363.14	7670032.83	21:04:12.06S	69:32:03.98W	140	72	5761	SSE
2010511.93	7668732.32	21:04:56.55S	69:53:55.68W	217	86	10485	N
2021493.48	7666743.79	21:06:00.89S	69:47:34.99W	262	-20	4858	ENE
2023245.62	7666589.19	21:06:05.84S	69:46:34.25W	421	84	25542	NNW
2028149.84	7664442.58	21:07:15.41S	69:43:44.13W	130	67	14600	NNW
2014116.60	7663944.90	21:07:32.19S	69:51:50.60W	215	-89	16662	N
2034421.63	7663503.96	21:07:45.56S	69:40:06.64W	52	58	17684	NNW
1994495.02	7663474.36	21:07:47.66S	70:03:10.85W	41	-45	3326	SW
2013950.33	7662931.14	21:08:05.17S	69:51:56.34W	48	33	1987	NW
2013280.41	7662049.68	21:08:33.86S	69:52:19.54W	94	-82	11156	N
2026067.02	7661752.38	21:08:43.03S	69:44:56.19W	28	66	21386	NNW
1994176.45	7660822.47	21:09:13.92S	70:03:21.93W	24	-50	3869	SW
2011270.67	7660427.78	21:09:26.66S	69:53:29.18W	195	56	4593	NW
2013173.97	7657264.91	21:11:09.50S	69:52:23.10W	59	-85	8647	N
1999201.61	7656264.00	21:11:42.22S	70:00:27.69W	56	-50	8712	SW
2004767.15	7652893.32	21:13:31.84S	69:57:14.62W	11	-58	4495	SW
2023969.92	7652781.23	21:13:34.94S	69:46:08.44W	45	81	10713	SSE
2010783.88	7651757.48	21:14:08.70S	69:53:45.87W	15	-9	1722	E
2023309.35	7649769.34	21:15:12.94S	69:46:31.21W	22	24	3556	NW
2002696.35	7649580.81	21:15:19.61S	69:58:26.44W	122	72	3700	NNW
2004443.24	7649151.26	21:15:33.57S	69:57:25.82W	31	-36	2326	WSW
2007242.75	7648854.61	21:15:43.18S	69:55:48.68W	49	-42	4506	SW
2031915.00	7646058.64	21:17:13.17S	69:41:32.37W	32	-3	5490	E
2001405.03	7645398.29	21:17:35.66S	69:59:11.23W	164	72	8767	NNW
2017238.14	7643002.29	21:18:53.30S	69:50:01.62W	73	65	19323	S
2031433.99	7640920.27	21:20:00.33S	69:41:48.72W	140	79	14955	S
2025424.66	7639727.59	21:20:39.47S	69:45:17.27W	43	-72	2612	SSW
2011387.76	7637768.79	21:21:43.69S	69:53:24.58W	70	-11	4739	ENE
2007361.26	7637610.89	21:21:48.91S	69:55:44.39W	54	76	6223	NNE
2025283.12	7635873.97	21:22:44.82S	69:45:21.98W	44	18	7391	ESE

Table 3.1 (Continued)

Easting (m)	Northing (m)	Latitude (º)	Longitude (º)	Offset (m)	Trend (º)	Trace Length (m)	Downside
2009650.84	7631294.82	21:25:14.31S	69:54:24.76W	76	-16	11582	WSW
2001086.18	7619659.84	21:31:32.85S	69:59:22.24W	74	-60	5437	SW
2011831.76	7619031.89	21:31:53.13S	69:53:08.69W	50	78	3938	S
2016069.17	7617987.82	21:32:26.97S	69:50:41.34W	163	-55	29819	S
2025743.98	7611332.20	21:36:03.04S	69:45:04.62W	32	-8	1585	W
2015637.20	7604388.62	21:39:49.31S	69:50:55.90W	34	3	9522	W
2028857.94	7598494.92	21:43:00.41S	69:43:15.52W	32	-19	13756	W
2001597.84	7591238.17	21:46:57.28S	69:59:04.36W	122	-27	4830	SW
1993229.04	7587764.33	21:48:50.23S	70:03:55.84W	177	14	12073	WNW
1996939.74	7582948.32	21:51:26.90S	70:01:46.63W	68	50	7093	NW
2009762.61	7582299.44	21:51:47.92S	69:54:19.84W	38	11	6022	W
1988948.64	7577804.53	21:54:14.09S	70:06:25.18W	33	69	5000	NNW
1995369.05	7576766.71	21:54:47.95S	70:02:41.41W	19	30	2459	NW
1990939.46	7574658.47	21:55:56.46S	70:05:15.85W	150	35	3362	NW
2014009.39	7570447.28	21:58:13.31S	69:51:51.50W	123	-2	10911	E
1999592.68	7568029.06	21:59:32.16S	70:00:14.20W	89	15	10783	WNW
1996468.88	7566584.42	22:00:19.13S	70:02:03.16W	31	50	3429	NW
2013010.41	7564322.56	22:01:32.54S	69:52:26.16W	48	2	4773	W
2011573.33	7561877.66	22:02:52.09S	69:53:16.23W	21	7	8557	W
1991886.88	7560999.96	22:03:20.71S	70:04:43.07W	71	-10	2836	WSW
1993314.62	7560102.89	22:03:49.91S	70:03:53.27W	49	66	4192	NNW
1986597.16	7557605.07	22:05:11.01S	70:07:47.73W	76	72	1797	NNW
2001755.85	7557277.60	22:05:21.84S	69:58:58.72W	48	-9	7015	E
1999781.97	7555315.49	22:06:25.66S	70:00:07.61W	52	-43	8082	NE
1999427.07	7554803.26	22:06:42.32S	70:00:20.00W	148	0	8122	W
1997407.55	7547115.93	22:10:52.33S	70:01:30.53W	25	36	2415	NW
1994531.73	7542446.49	22:13:24.18S	70:03:11.02W	345	25	4992	NW/SW
1987040.39	7541491.25	22:13:55.10S	70:07:32.73W	70	52	1912	NW
1984099.17	7537086.50	22:16:18.27S	70:09:15.63W	153	-15	7009	WSW
1983399.65	7535498.80	22:17:09.88S	70:09:40.14W	50	60	9863	SE
2012844.58	7530861.20	22:19:40.83S	69:52:30.98W	43	6	13387	WSW
1984662.87	7529024.83	22:20:40.48S	70:08:56.21W	54	47	10397	SE
1986557.69	7525550.99	22:22:33.51S	70:07:50.07W	56	53	8882	SE
1997887.15	7524445.67	22:23:09.65S	70:01:13.89W		7	36812	W
1991965.83	7520577.08	22:25:15.40S	70:04:41.04W	291	70	7547	NNW
1988570.94	7516629.53	22:27:23.72S	70:06:39.90W	118	25	6155	NW

Table 3.1 (Continued)

Easting (m)	Northing (m)	Latitude (º)	Longitude (º)	Offset (m)	Trend (º)	Trace Length (m)	Downside
2008535.28	7515514.18	22:28:00.05S	69:55:01.33W	120	4	15044	W
1995834.42	7501234.10	22:35:44.53S	70:02:25.90W	136	4	3519	W
1987881.77	7500780.16	22:35:59.16S	70:07:04.45W	79	13	2415	W
1983044.37	7497049.70	22:38:00.33S	70:09:54.03W	39	15	4140	ESE
2014314.54	7495914.06	22:38:37.35S	69:51:38.46W	94	9	10887	W
1980912.70	7493970.61	22:39:40.38S	70:11:08.85W	86	42	2909	SE
1982610.14	7484417.55	22:44:51.13S	70:10:09.75W		8	7757	E
1987584.05	7478890.98	22:47:51.02S	70:07:15.50W	31	26	8619	SE
1998021.22	7476328.25	22:49:14.52S	70:01:09.42W	146	15	11507	ESE
1995913.37	7466021.98	22:54:49.68S	70:02:23.47W	34	20	8438	ESE
1998755.61	7464442.96	22:55:41.05S	70:00:43.69W	51	17	8112	ESE
1992676.39	7461837.58	22:57:05.72S	70:04:17.17W	106	14	50942	ESE
1998600.39	7441787.66	21:08:42.55S	70:00:48.53W	53	-68	2091	SSW
2004761.14	7441116.51	23:08:19.61S	69:57:12.58W	127	46	20758	SE
1988847.26	7441073.48	23:08:20.89S	70:06:32.18W	61	20	9187	ESE
1973280.73	7438889.37	23:09:31.28S	70:15:39.70W	300	13	65750	ESE
2008736.43	7431644.39	23:13:27.58S	69:54:52.59W	105	38	25597	WNW
1987426.15	7428441.33	23:15:11.65S	70:07:22.53W	211	27	59436	SE
1993979.08	7427809.72	23:15:32.32S	70:03:31.91W		28	7251	ESE
2025283.12	7422125.25	23:18:36.51S	69:45:09.80W	85	57	5062	NNW
1975741.41	7420546.24	23:19:27.92S	70:14:14.22W		9	25942	ESE
2000689.91	7402624.37	23:29:11.36S	69:59:35.68W	70	85	8642	S
1986241.88	7396624.10	23:32:26.27S	70:08:05.25W	39	41	4293	SE
1971162.25	7392202.85	23:34:49.32S	70:16:57.42W		20	21761	SE
2015216.88	7381228.67	23:40:46.85S	69:51:02.73W	61	-20	16502	ENE
1970114.13	7345381.81	24:00:11.72S	70:17:37.82W		-9	37046	E
1972583.37	7332910.69	24:06:57.39S	70:16:11.26W		11	9452	WNW
1958293.25	7330384.26	24:08:18.41S	70:24:37.76W		-39	13690	SW
1962626.97	7329611.08	24:08:43.94S	70:22:04.28W	314	-8	46080	ENE
1972318.44	7301810.30	24:23:48.59S	70:16:22.81W	148	-13	12102	WSW
1958648.53	7292408.86	24:28:53.18S	70:24:29.12W		6	14044	
1984465.49	7289566.63	24:30:27.29S	70:09:12.02W		-1	5600	E
1970363.46	7287151.29	24:31:45.08S	70:17:33.32W	66	-45	6033	NE
1973938.82	7284520.37	24:33:10.86S	70:15:26.42W	56	-17	5797	ENE
1965190.28	7281168.03	24:34:59.23S	70:20:37.70W	303	10	88540	ESE
1958332.73	7275355.46	24:38:07.60S	70:24:42.15W		-16	18417	

Table 3.1 (Continued)

Easting (m)	Northing (m)	Latitude (º)	Longitude (º)	Offset (m)	Trend (º)	Trace Length (m)	Downside
1969599.25	7273406.25	24:39:11.93S	70:18:01.54W	145	-33	4625	SW
1965078.16	7266715.34	24:42:49.12S	70:20:42.98W	215	-1	17785	W
1954730.48	7260706.25	24:46:03.52S	70:26:51.98W	199	9	24882	E
1964230.52	7249972.88	24:51:53.39S	70:21:14.70W	68	13	6274	WNW
1974222.19	7237895.16	24:58:26.78S	70:15:19.44W	73	28	11059	NW
1980991.65	7185825.09	25:26:39.98S	70:11:20.60W		-17	111304	
1992382.04	7159928.05	25:40:42.25S	70:04:33.29W	44	-6	6589	W
1963306.64	7153297.30	25:44:16.22S	70:21:57.02W		9	50326	
1972543.90	7144612.70	25:48:59.27S	70:16:26.12W		10	85869	
1968596.35	7124401.26	25:59:56.01S	70:18:49.64W		17	42109	
1970806.98	7112084.91	26:06:36.54S	70:17:31.11W		0	24007	
1963306.64	7049871.57	26:40:18.17S	70:22:07.57W		13	51677	
1948384.91	7001869.40	27:06:16.66S	70:31:14.56W		27	39957	
1960069.65	6999974.58	27:07:19.64S	70:24:10.43W		21	28910	
1909383.14	6852652.12	28:26:58.26S	70:55:31.71W		24	56558	
1910014.75	6845546.54	28:30:49.29S	70:55:10.49W		13	49821	
1932278.92	6820755.94	28:44:19.66S	70:41:36.76W		8	32783	
1905909.30	6814597.77	28:47:33.79S	70:57:50.70W		13	20397	
1891145.48	6752226.53	29:21:15.84S	71:07:17.09W		8	75161	
1882460.87	6749384.29	29:22:45.36S	71:12:40.21W		62	13171	

3.2 *Distribution of Faults*

The most striking pattern that emerges from the fault map at first glance is the dominance of long N-S faults in the southern portion of the study area (south of 21° 30′ S) and the shorter, E-W faults to the north. The density of faults also increases in the northern section of the Coastal Cordillera and the fault trends are not limited to E-W, but also include N-S, NW-SE and NE-SW. The fault map highlights a distinct change in pattern at 21° 30′ S latitude, just south of the Loa River outlet to the Pacific Ocean. Figure 3.5 shows a breakdown of the faults (including those not matching our criteria) into the following general families of trends: E-W, N-S, NW-SE, and NE-SW. Evidence of faulting ends where the Coastal Cordillera terminates on-shore in the north.

Figure 3.5a emphasizes the complete absence of E-W faults to the south of 21° 30′ S with one small exception at 23° 30′ S. The overall orientation of the E-W faults migrates into an ENE-WSW direction as the faults increase their proximity to Arica (18° 30′ S). This orientation follows the change in along-strike direction of the Coastal Cordillera (Figure 3.6). Although the faults and the Coastal Cordillera die out south of Arica and the Central Depression borders the Pacific Ocean at the Arica bight, the range continues offshore as a submarine bench on the continental shelf. The Coastal Cordillera has subsided in this area. We lack any high resolution bathymetry to determine if the faulting pattern continues beyond the onshore termination. Maximum offsets measured for this set of faults range from 20 meters to 567 meters at Falla Atajaña. Fault trace lengths vary from 1.1 to 30 kilometers and the average is 10.9 kilometers. Out of 62 E-W scarps, 40 are offset with the north

Figure 3.5. Fault map divided into four families of trends in the study area: a) east-west, b) north-south, c) northwest-southeast, and d) northeast-southwest.

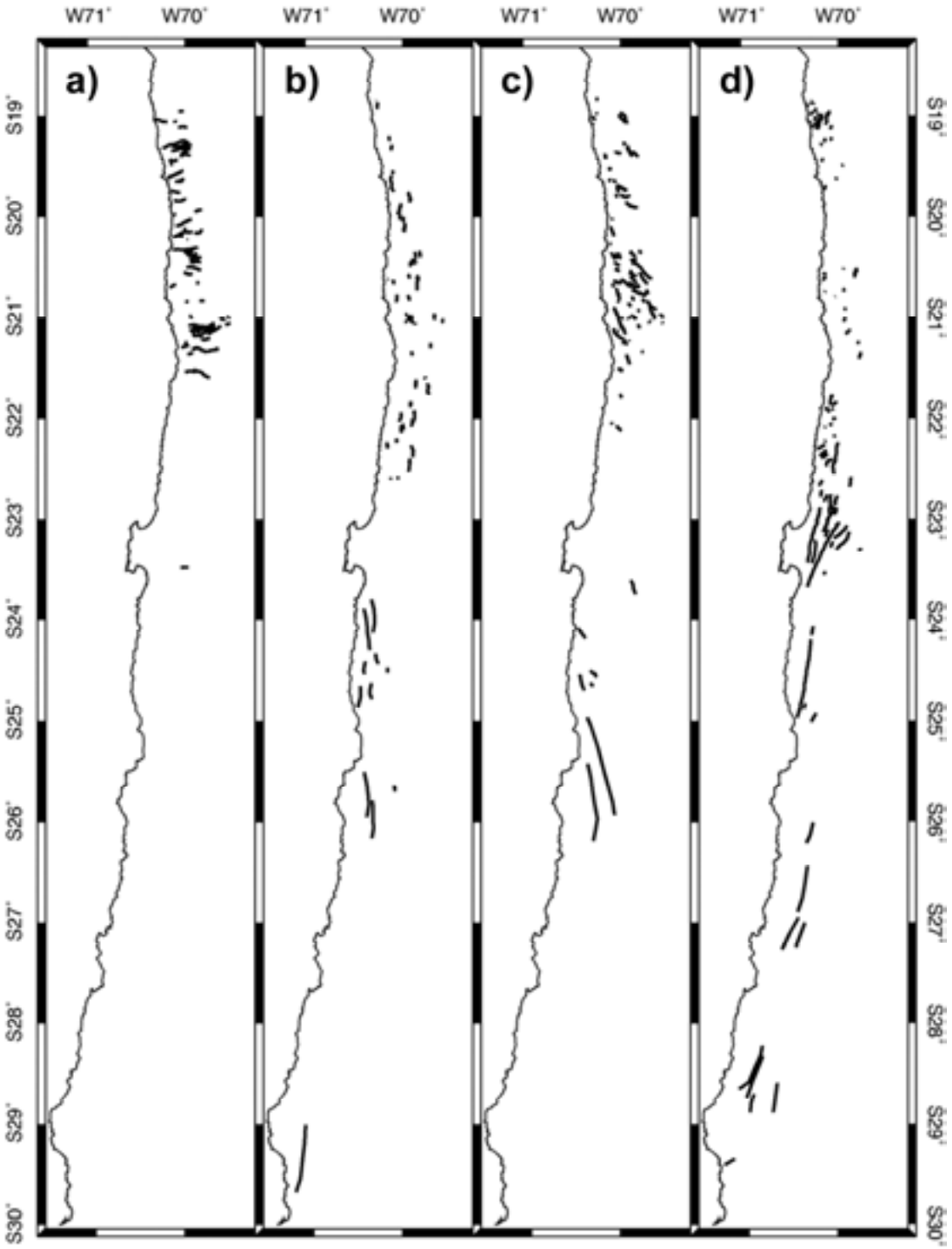
a)
b)
c)
d)
W71°
W70°
S19°
S20°
S21°
S22°
S23°
S24°
S25°
S26°
S27°
S28°
S29°
S30°

Figure 3.6. Plot of E-W trending faults on the Coastal Cordillera. Note the change in orientation of the E-W faults as their proximity to the orocline increases. The faults remain orthogonal to the along-strike direction of the Coastal Cordillera as it parallels the trench to the west and moves off-shore. The bathymetric data highlight the continuation of the Coastal Cordillera in the Pacific Ocean and the subsidence of the range just off the coast of Arica.

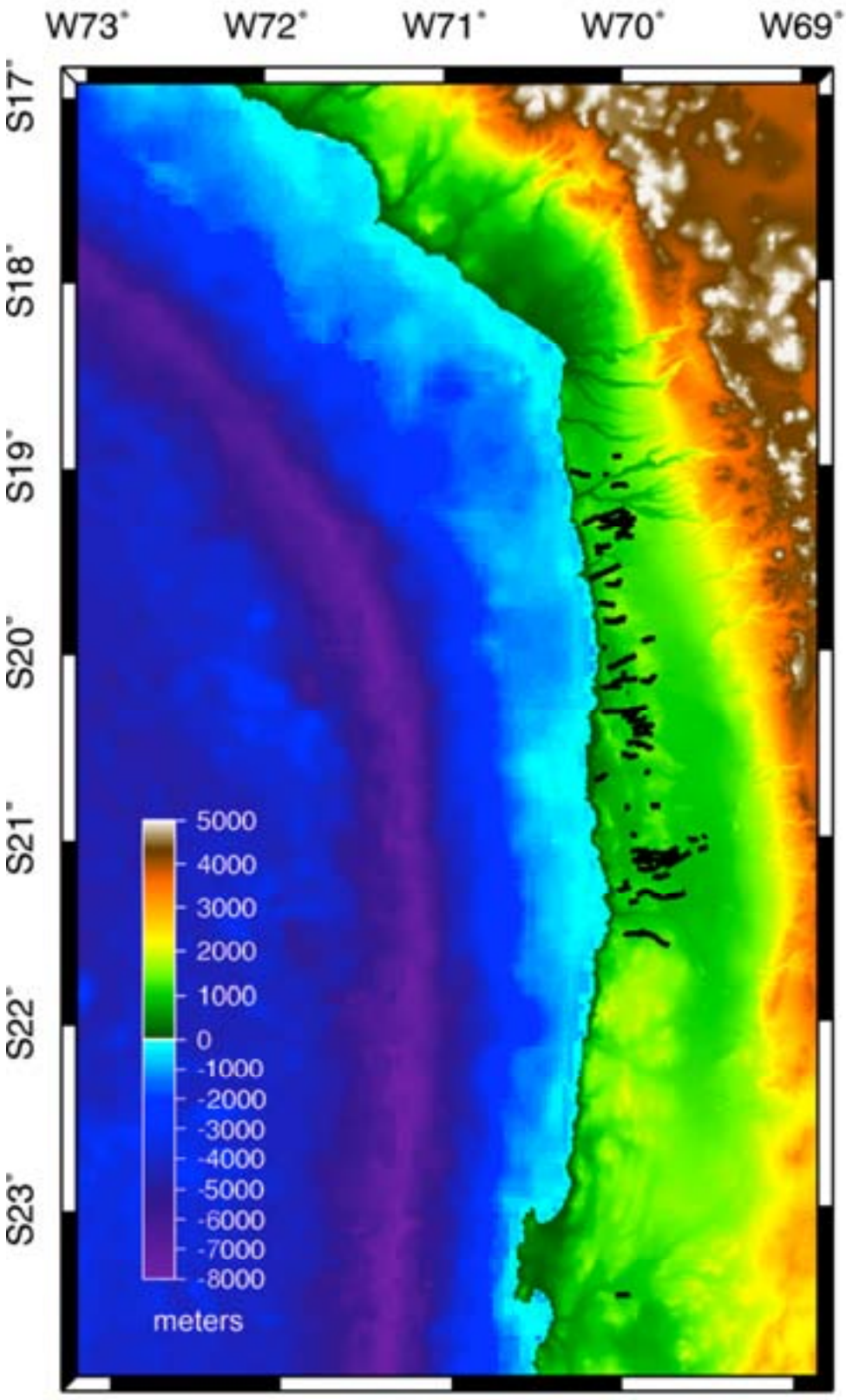
W73°
W72°
W71°
W70°
W69°
S17°
S18°
S19°
S20°
S21°
S22°
S23°
5000
4000
3000
2000
1000
0
-1000
-2000
-3000
-4000
-5000
-6000
-7000
-8000
meters

side down, and the other 22 are offset with the south side down. These descriptive statistics are listed in Table 3.2 for the four trend classifications. The scarps in the north near Salar Grande are distinct and continuous and have youthful looking profiles (Figure 3.7).

Table 3.2 Summary of Fault Scarp Descriptive Statistics Based on Trend Groupings

	E-W	N-S	NW-SE	NE-SW
Minimum trace	1.1	1	0.6	0.7
Average trace	10.9	6.8	9.2	12.3
Maximum trace	30	18.7	32.3	88.5
Maximum red trace	N/A	75.1	111.3	56.6
Minimum offset	20	10	6	15
Average offset	99	84	56	78
Maximum offset	567	345	343	303
# side down	North 40	West 41	SW 55	NW 55
# side down	South 22	East 15	NE 31	SE 21
Total faults	62	62	90	91
Red faults	0	6	4	15

The N-S faults (Figure 3.5b) have shorter trace lengths north of 23° S. The average length is 6.8 km, ranging from 1.0km to 18.7 km. 62 faults are considered in the N-S grouping, 6 are low-confidence (do not meet all criteria, but are clearly long traceable lineaments). Of the 56 remaining scarps, 41 have offsets with west side down and 15 are east side down. South of 23° S, the traces are reactivated branches of the AFS with noticeably longer trace lengths. Near La Serena (30° S), a speculative trace measures over 75 kilometers. The continuity of the scarps is difficult to follow as we move south due to degraded scarp fronts that have been heavily dissected, but not

Figure 3.7 Prominent E-W scarps to the east of Salar Grande. Black line denotes location of profile plot with a vertical exaggeration of 100. Arrows indicate the NW-SE trending strike-slip fault (Cerro Chuculay Fault) that has dextrally displaced the E-W faults by 1 kilometer.

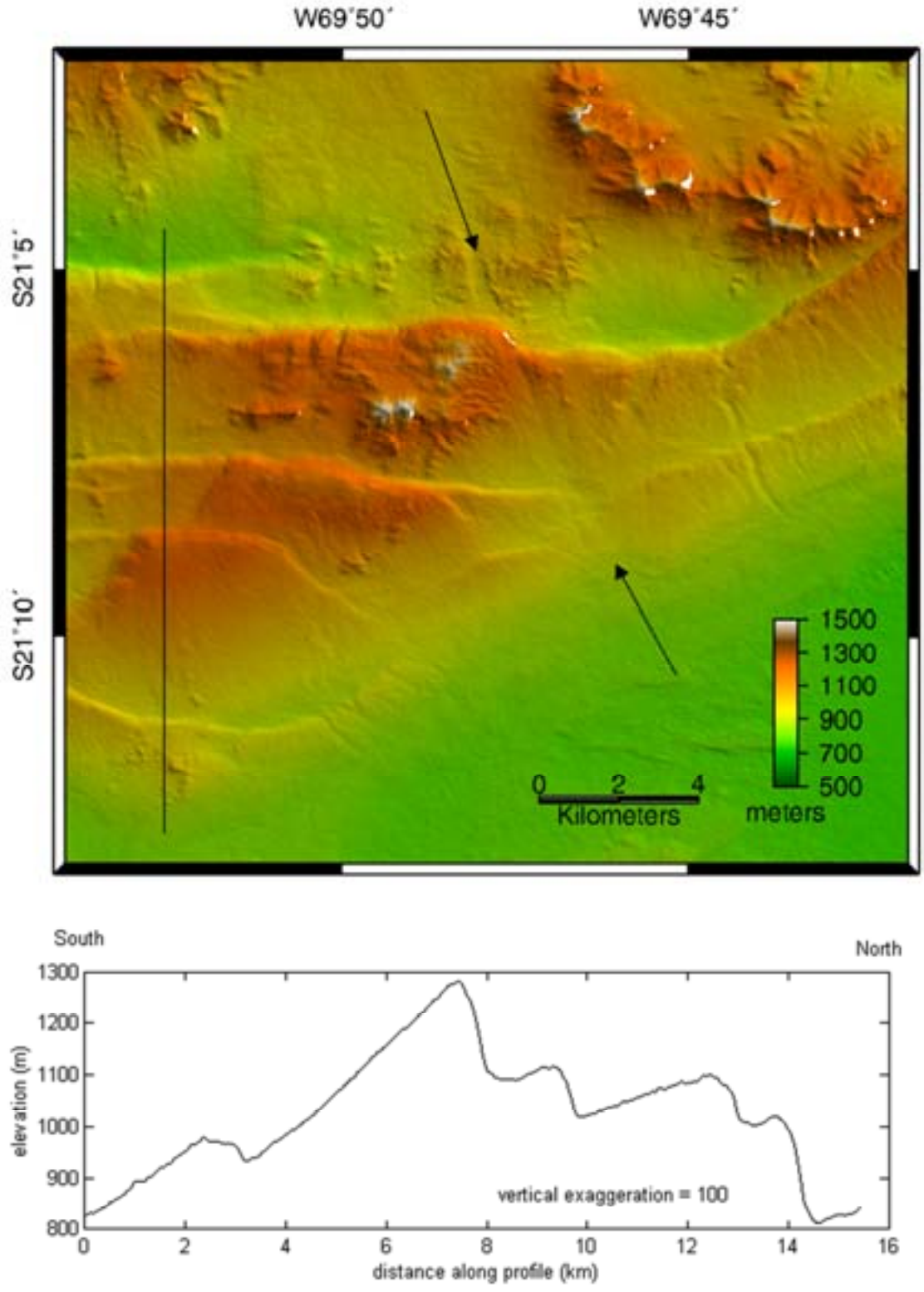
W69°50′
W69°45′
S21°5′
S21°10′
1500
1300
1100
900
700
500
0 2 4
Kilometers
meters
South
North
elevation (m)
1300
1200
1100
1000
900
800
vertical exaggeration = 100
0 2 4 6 8 10 12 14 16
distance along profile (km)

obliterated, by both aerial and fluvial erosion. The decrease in aridity south of 25° S may play a key role in the increased erosion on these structures (Figure 3.8). Data dropouts on the eastern slopes due to radar shadow, and the topography resolution transition from 20 meters to 90 meters near 26° 30′ S latitude also contribute to the red-flagging of in this portion of the map. It is possible that traces might be longer and perhaps more abundant with a complete dataset, but the nature of the faulting is obviously different along the southern AFS than in the northernmost end of the Coastal Cordillera.

The distribution of NW-SE faults in Figure 3.5c is most similar to the N-S faults in Figure 3.5b. There is a cluster of these scarps around 21° S, some of which are interpreted to be strike-slip faults based on dextral offsets of E-W scarps (Figure 3.7). 90 faults fall within this grouping, 4 of which are red-flagged for intermittent fault trace. Out of the 86 NW-SE faults, 55 show SW side down and 31 are NE side down. The average trace length is 9.2 km. The shortest recorded length is 0.6 km and the longest is 32.3 km. Among the red-flagged faults, the longest length jumps to 111.3 km in the southern AFS. The NE-SW scarps have the greatest range of coverage in the study area (Figure 3.5d) and are heavily controlled by the AFS from 22° S to 30° S. This group sparsely populates the Coastal Cordillera from 19° S to 22° S and is nearly absent between Pisagua (19° 30'S) and Iquique (20° 15'S). Trace lengths are generally longer south of 23° S latitude, whereas to the north these traces are on average the shortest of all four groupings. Of the 91 faults, 15 have discontinuous surface expression, 55 are faulted with the NW side down and the remaining 21 are down to the SE. The majority of the SE side down faults

Figure 3.8 Degraded N-S segment of the AFS near Chañaral crossed by E-W drainages heading toward the coast. Black line marks the location of the profile plot (bottom) with vertical exaggeration of 100. Scarp profiles are not well defined on the southern AFS in contrast to northern scarps (see Figure 3.7).

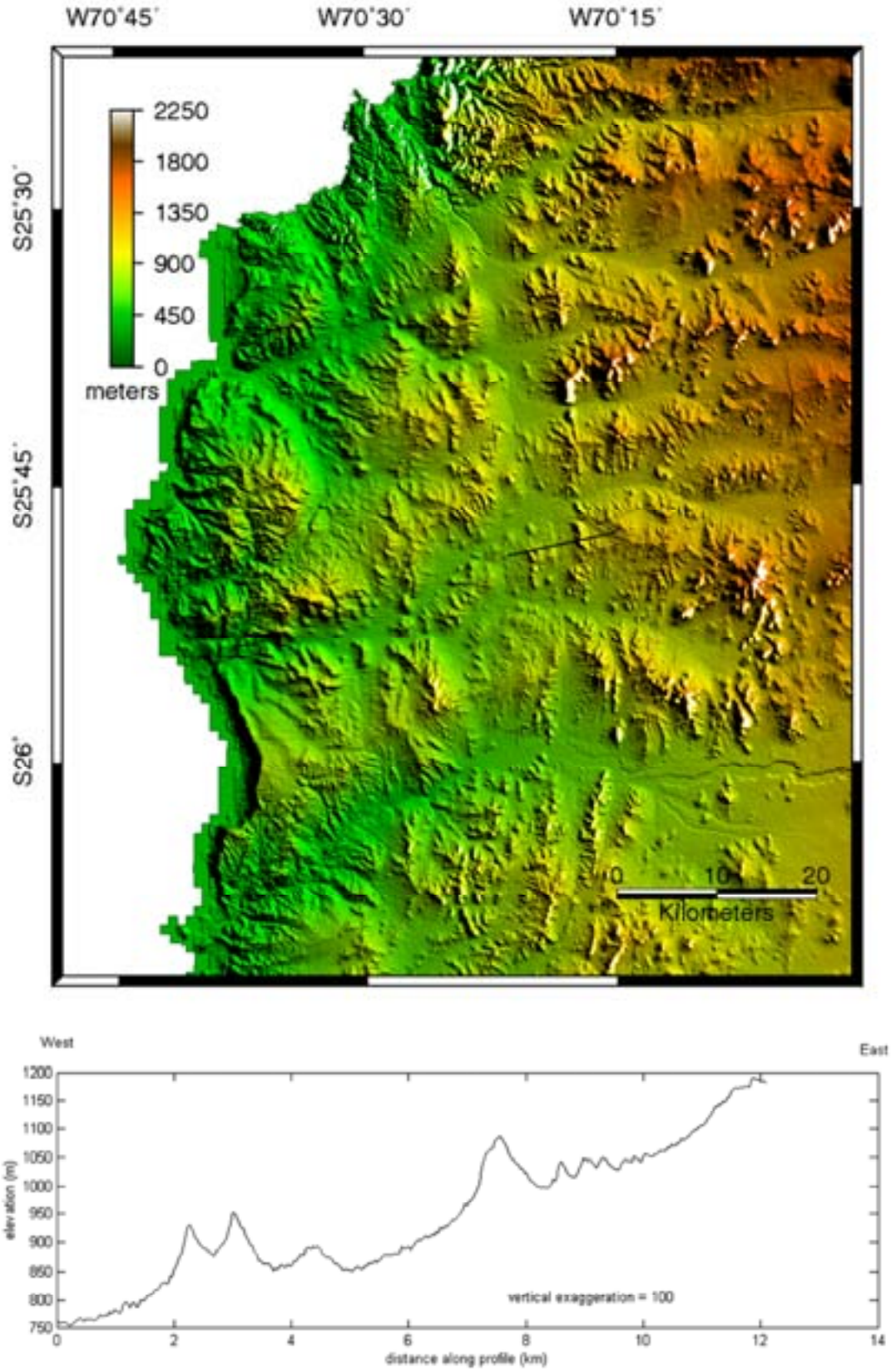
W70°45'
W70°30'
W70°15'
S25°30'
S25°45'
S26°
2250
1800
1350
900
450
0
meters
0
10
20
Kilometers
West
East
elevation (m)
1200
1150
1100
1050
1000
950
900
850
800
750
vertical exaggeration = 100
0
2
4
6
8
10
12
14
distance along profile (km)

are located in the southern end of the study area. The fault lengths range from 0.7 km to as much as 88.5 km, and the average is 12.3 km.

3.3 *Statistics*

We present statistical analyses in Table 3.3, omitting the highlighted scarp entries for which a definitive trace or reliable offset could not be determined. Correlation between fault scarp properties is poor overall (Table 3.3).

Table 3.3 Fault Scarp Statistical Analysis: Correlation Matrix and Principal Components

Correlation Matrix

	Easting	Northing	Offset	Trend	Trace
Easting	1	-0.004	-0.120	-0.104	-0.095
Northing		1	-0.213	-0.019	-0.272
Offset			1	0.154	0.494
Trend				1	0.051
Trace					1

Mean	2001635	7695910	77	5	8525
Std. Dev.	17262	150328	69	48	9478

Eigenvectors

e_1	0.21	0.41	-0.61	-0.21	-0.61	*35%*
e_2	0.00	-0.09	0.69	-0.14	-0.71	*44%*
e_3	0.64	-0.41	-0.01	-0.63	0.17	*66%*
e_4	0.31	0.80	0.39	-0.14	0.30	*82%*
e_5	0.67	-0.11	0.02	0.72	-0.11	*100%*

There are a few trends: maximum vertical offset scales with trace length, and longer fault scarps and larger offsets tend to appear in the south. Are there hidden correlations between linear combinations of scarp properties? A principal component analysis of 284 fault scarps indicates that there is no principal axis, plane, or 3-plane in these data; the first three principal components can account for only two-thirds of the variance in the data, which indicates that there is no outstanding correlation between the fault scarp properties for this map. Figures 3.9-3.11 show the strongest correlations between scarp properties.

3.4 Discussion

The only part of the Chilean terrestrial forearc where the Nazca and South American plates come into contact lies beneath the Coastal Cordillera. The surface faulting we identify in the Coastal Cordillera presumably reflects the coupled interactions at the interplate boundary to some degree. Two patterns in the surface faulting of the forearc are visually evident in the fault map (Figure 3.3). The first is the abundance of E-W trending fault scarps north of 22° S, and the second is the dominance of longer N-S faults south of 22° S. The geographic dichotomy implies a regional factor or factors affecting the along-strike character of faulting in the forearc.

3.4.1 *E-W Faulting*

Due to the limited spatial distribution of the E-W faults between 19° S and 21.5° S latitude, we consider regional factors and anomalous features that

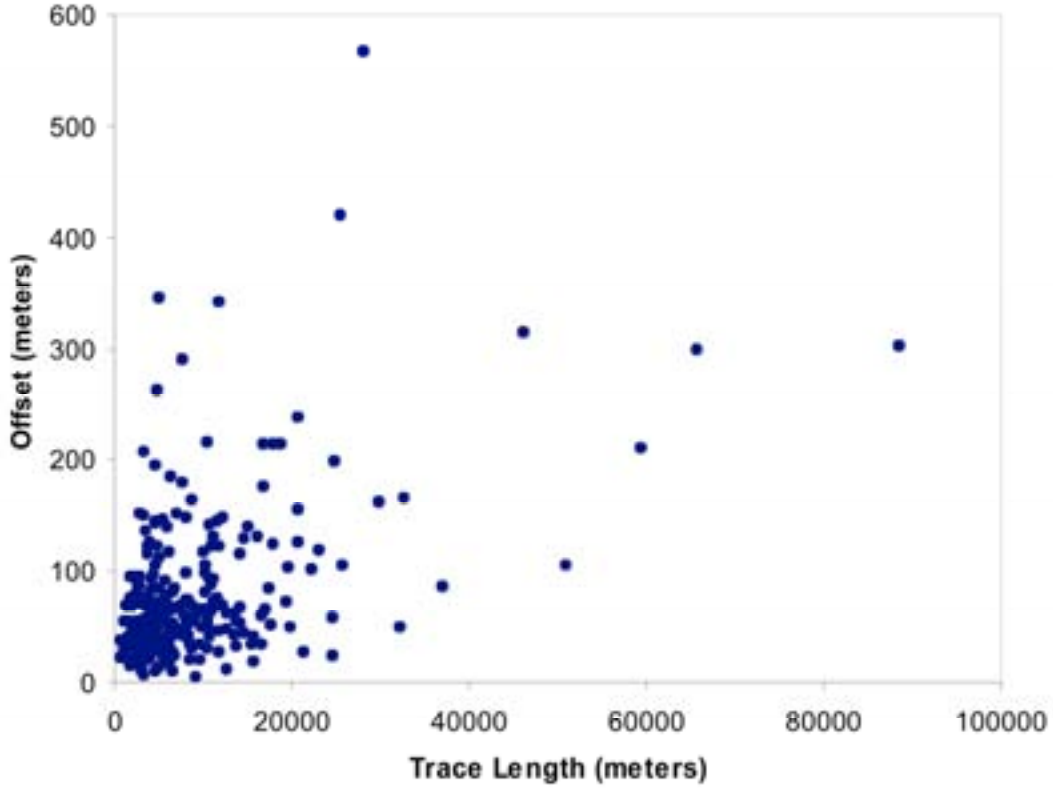

Figure 3.9 Fault scarp maximum vertical offset versus trace length.

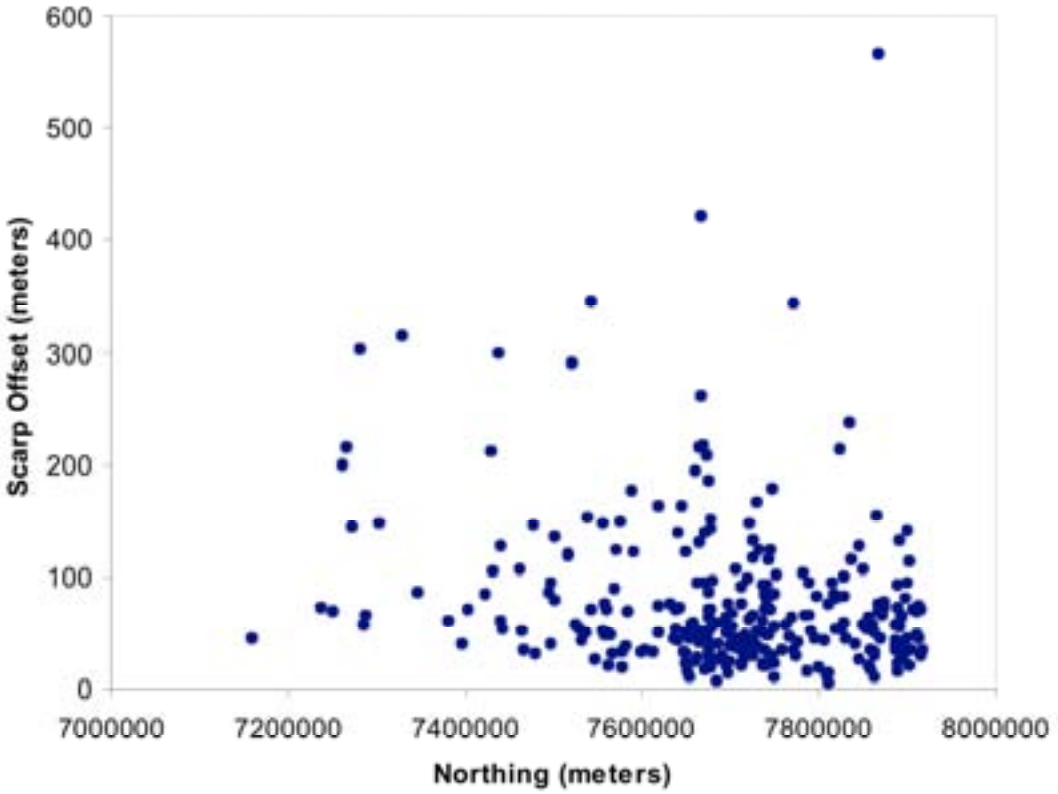

Figure 3.10 Fault scarp maximum vertical offset versus Northing.

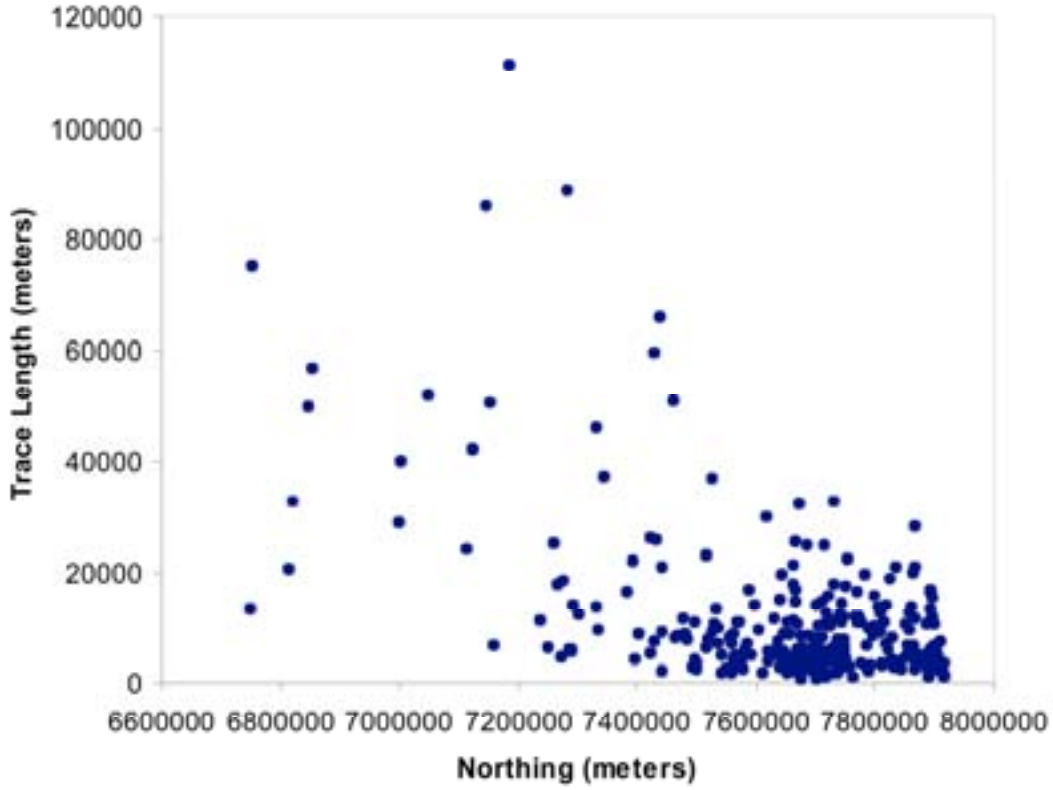

Figure 3.11 Fault scarp trace length versus Northing.

could be responsible for the faulting pattern in this part of the forearc: climate, the pre-existence of the AFS, the aseismic Iquique Ridge, proximity to the Bolivian Orocline, and segment boundaries at the subduction interface. Since the plates are strongly coupled, we expect subduction processes to play a significant role in the surface morphology.

3.4.1.1 *Climate*

An increasing precipitation gradient exists along the length of the Chilean coast from Arica to Patagonia. The climate within the study area is consistently hyper-arid from 18° S down to approximately 25° S, where it transitions to arid. The boundary between the regions of E-W faulting and N-S faulting at 22° S, falls well within the hyper-arid portion of the Coastal Cordillera. If similar E-W faults existed further south, we would expect them to be as well preserved as their counterparts to the north without signs of increased degradation until reaching at least 25° S. Climate does play a role in the dissection of the Paposo and El Salado segments of the AFS, but it is not responsible for the lack of distinct E-W fault structures south of 22° S.

3.4.1.2 *AFS*

The structures of the AFS control the majority of the N-S faulting south of 22° S. Cenozoic normal offsets on old AFS strike-slip faults account for the longer segments in the fault map. Many of these are fault line scarps and reactivations of old structures. We identify several N-S faults north of 22° S, but the nature of these faults has a more continuous scarp and shorter trace

than the southern counterparts. Some of these can be attributed to reactivations near the terminus of the AFS, but several are new faulting that is not part of the AFS.

3.4.1.3 *Iquique Ridge*

The Iquique Ridge is an aseismic ridge averaging 1000 m of relief above the surrounding seafloor off the coast of northern Chile (Figure 1.1). It has a width of approximately 130 km and strikes at 45°. Ridge subduction has been studied to the north where the Nazca Ridge impinges on the west coast of Peru at 15° S latitude. The Nazca Ridge, rising 1750 m above the seafloor and about 200 km in width, is a more pronounced bathymetric feature than the Iquique Ridge. There exists a distinct peninsula and offshore shoaling where the ridge intersects at the coast. Hsu (1988) ran a simple model to characterize and determine the amount of topographic displacement (uplift) expected at the leading edge of forearc deformation with respect to the bathymetric relief of the ridge. The model predicted one to one displacement to relief, although actual data showed a 75-85% displacement onshore to ridge relief. Both observed and predicted subsidence follow the trailing edge of the projected ridge onshore, based on a southward migration.

Extrapolating a line from the Iquique Ridge inland intersects the coast at about 20° 30' S, coinciding with the vicinity of the E-W faulting. The orientation of the ridge and the convergence direction of the Nazca plate results in a southward migration of the leading edge of the ridge with respect to the coast, causing compression to the south in an almost N-S direction.

The Iquique Ridge, when projected onto the Chilean coast, does not show signs of forearc shoaling that stand out from the surrounding shelf given the magnitude of the bathymetric relief, nor is there strong topographic evidence of uplift south of the leading edge (based on the convergence direction of the Nazca plate with respect to the South American plate and the strike of the ridge). Rosenbaum et al. (2005) assert the Iquique Ridge has only entered the trench within the past 2 My and has not yet subducted beneath the South American plate. Considering the lack of a ridge subduction signature in the forearc due to the fact that the Iquique Ridge is believed to be in the early stages of entering the trench, it is unlikely that the E-W faulting, dated older than 2 My by Allmendinger et al. (2005a), is a result of ridge subduction.

3.4.1.4 *Oroclinal Bend*

A notable geographic feature of the Andean forearc that differs in the north from the rest of the Chilean forearc is that this region is part of the southern end of the oroclinal bend. The trench, the forearc, and the plateau bend concave west starting near the E-W fault zone, resulting in a different subduction geometry and in different forces acting on the forearc. Gephart (1994) determined that the vertical symmetry plane of the Bolivian Orocline, based on topography and subduction geometry, was actually south of the bend in the coast. Allmendinger et al. (2005a) observed that the spatial distribution of E-W faults center on Gephart's symmetry plane, which crosses the Chilean coast at 20° 30' S. They believe that the arc-parallel shortening responsible for the E-W faulting is related to deformation from inner oroclinal

bending, but is not necessarily a direct result of it. In the simplest scenario, the forearc is expected to compress the way the concave side of a bending beam does. The lack of vertical axis rotation in the forearc based on paleomagnetic studies (Roperch et al., 1999) suggests more complex and subtle processes influence forearc deformation. Allmendinger et al. (2005b) show that GPS data analysis indicates the bending is ongoing.

Allmendinger et al. (2005a) compare observational data with predictions from McCaffrey's (1996) kinematic model of the forearc and Bevis et al.'s (2001) elastic model integrating GPS vectors with a concave forearc locked at 20-50 km depth. Both models support N-S compression in the northern portion of the Chilean forearc although the models differ on where the transition from extensional to compressional regimes takes place. Neither of these account for the limited spatial extent of the E-W faulting, although they offer potential explanations for the reverse faulting in the E-W zone.

3.4.1.5 *Segment Boundaries*

The work of Victor and Sobiesiak (2005) examined surface faulting in the north Chilean forearc and correlated the spatial extents of what they determined to be active faulting with segment boundaries (boundaries to the propagation of coseismic rupture zones). Sobiesiak (2005) measured b-values (the slope of the logarithmic relationship between magnitude and frequency of earthquakes) based on aftershocks of the Antofagasta 1995 Mw=8.1 earthquake. A high b-value means a greater proportion of energy is released in larger earthquakes for a given sample. Sobiesiak mapped the spatial variability of b-values in the

vicinity of Antofagasta (approximately 23° 30' S), linking b-values to the physical structure of the Nazca-South American fault plane interface. According to Sobiesiak, areas of high b-values can resolve asperities at the interface. She interprets these asperities as batholiths in the overriding plate based on isostatic residual anomalies, mapped Jurassic batholiths, and high b-values.

Victor and Sobiesiak (2005) assert the asperities act as segment boundaries to fault activity at the surface. They map asperity locations and high concentrations of active faulting around the rupture zone of the 1995 Antofagasta earthquake and show asperity locations (inferred from high b-values) coinciding with transitions from zones of high active faulting to zones of low active faulting in the Coastal Cordillera at 23.3° S. Extrapolating this relationship to the north, they suggest there is a similar zone of high active faulting between 21.2° S and approximately 19° S, bordering zones of low active faulting in the 1877 seismic gap that could be explained by segment boundaries. The area of high fault activity in the northern segment overlaps with our zone of E-W faulting, although no b-value mapping is given for this area because of the seismic gap (the absence of a recent large earthquake). Instead, they claim this part of the plate interface has the greatest number of high magnitude seismic events for temporal length of seismic gap. This may impact the density of active faults, but does not explain fault orientation.

Loveless and Allmendinger (2005) applied an elastic half-space dislocation model to a possible segment boundary near Antofagasta. In this model the portion of the subduction zone north of the Mejillones Peninsula was locked

between 20 and 50 km depth and the segment south of the peninsula was locked at 20 to 38 km depth. The results show changes in the strain field (maximum principal extension) that approximate the strike of the AFS, in particular, the eastward jog of the Salar del Carmen segment. This reinforces the hypothesis that the Mejillones Peninsula is the manifestation of a segment boundary at depth, although no such feature is identified to the north near the E-W faulting zone.

3.4.2 *Overprinting*

North of Iquique in the Coastal Cordillera exists a curious concentration of overprinting faults. The location, centered on 20° 25' S, 69° 55' W appears on the fault map as a cluster of relatively short (10-20 km length) north-south and east-west fault scarps with a few scalloped fault traces criss-crossing the surface. Peneplanation occurred at the end of the Oligocene, so it is likely that the faulting records Neogene deformation.

There are three dominant patterns in this area: a series of north-south oriented ridges, east-west scarps, and north-south scarps. The north-south ridges appear to be relicts of scarps that have been incised, eroded, and subsequently faulted by the east-west scarps. These appear to be the oldest of the features, spaced approximately 1-4 km apart over 21 km distance. The east-west scarps are less pronounced in offset compared to the large E-W scarps distributed along the Coastal Cordillera in the Allmendinger et al. (2005a) study. Scarp offsets range from a few tens of meters to 120 meters and the scarps are about 10-20 km in length. Some of the fault traces are

irregular and resemble cuestas. It is possible, because of the orientation, that some of these scarps have been modified by drainage before or during uplift of the Coastal Cordillera. Profiles across a few scarps show gully-like features at the base of the scarp. The fault-bounded blocks exhibit a curious pattern in map view. There appears to be a block that is topographically higher than the two blocks that bound it to the north and south (20:26:27.93S, 69:55:13.37W) (Figure 3.12). South of that fault block, all major E-W faults appear to be south-facing until the Cerro Chuculay series of north-facing faults. North of the same fault block, all E-W faults face north. On average the faults are spaced between 1-3 km.

The second group of N-S faults is smaller in offset, extent, and trace length. Offsets run about 10-60 meters in height. The relative ages of these faults with respect to the E-W faults is ambiguous based on the DEM. In some instances the N-S faults appear to be younger because some abut the E-W faults. Examination of imagery on GoogleEarth for this area suggests that the N-S faults are younger than the E-W faults that they offset. Evidence of old mining activity exists along several faults here, but not enough to alter the scarps as viewed in the DEM.

A somewhat similar morphology is found in south-central Oregon where extensive faulting and cross cutting occurs in a horizontal surface of basalt flows. Donath (1962a) determined the majority of the faults had near vertical dips. Most of those faults formed as conjugate strike-slip shear zones in a stress system characterized by a north-south maximum principal stress and

Figure 3.12 The Coastal Cordillera north of Iquique exhibits curious overprinting faults and several E-W faults of lesser magnitude than the E-W faults from Allmendinger et al. (2005a). Figure 3.12a is the sun-shaded color 20-meter DEM. Figure 3.12b overlays interpreted faults over the same grayscale sun-shaded DEM. Red denotes the E-W faults, which have a greater distribution than the limited N-S faults marked in blue. The black star identifies the keystone block.

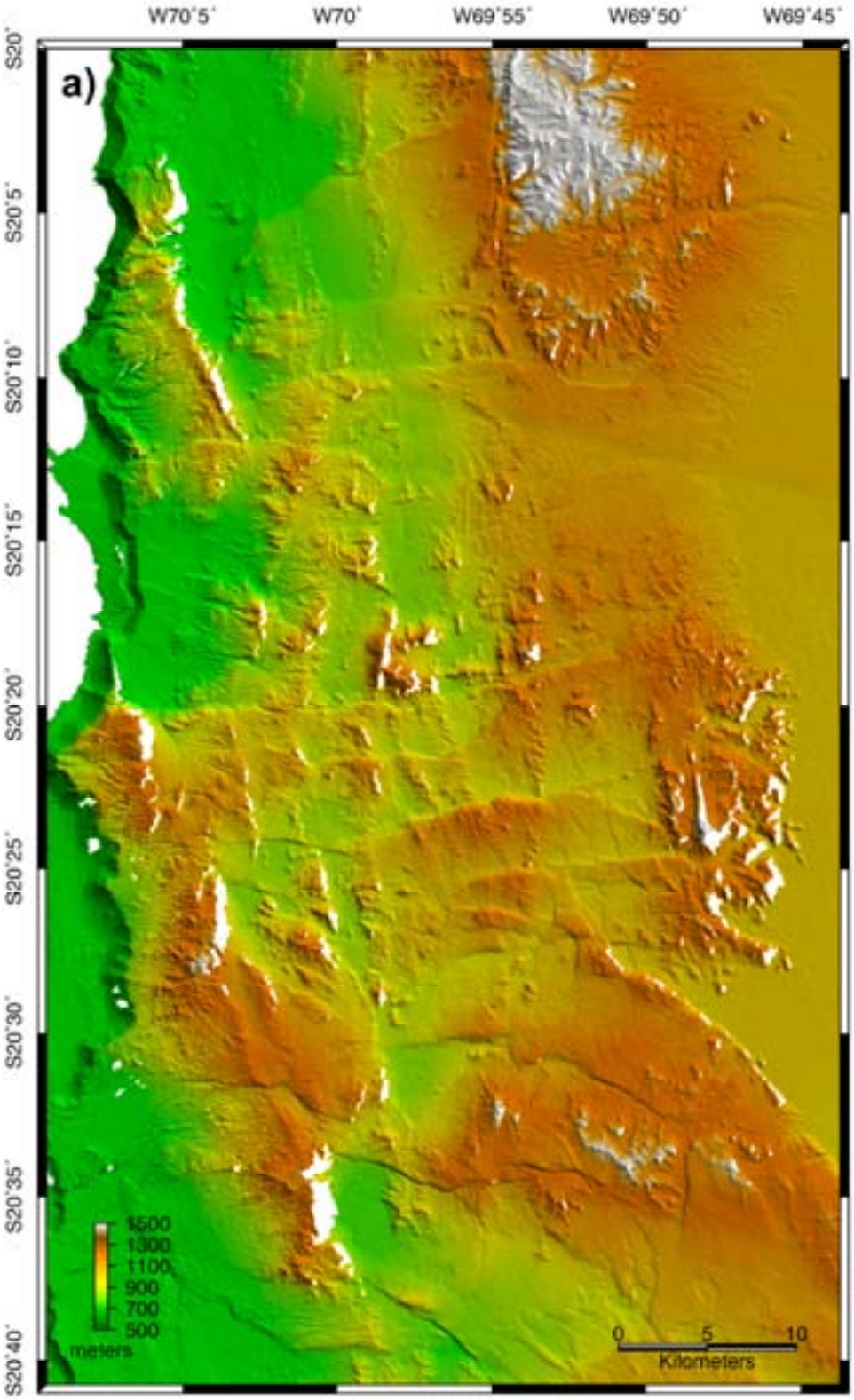
W70°5'
W70°
W69°55'
W69°50'
W69°45'
S20°
S20°5'
S20°10'
S20°15'
S20°20'
S20°25'
S20°30'
S20°35'
S20°40'
a)
1500
1300
1100
900
700
500
meters
0
5
10
Kilometers

Figure 3.12 (Continued)

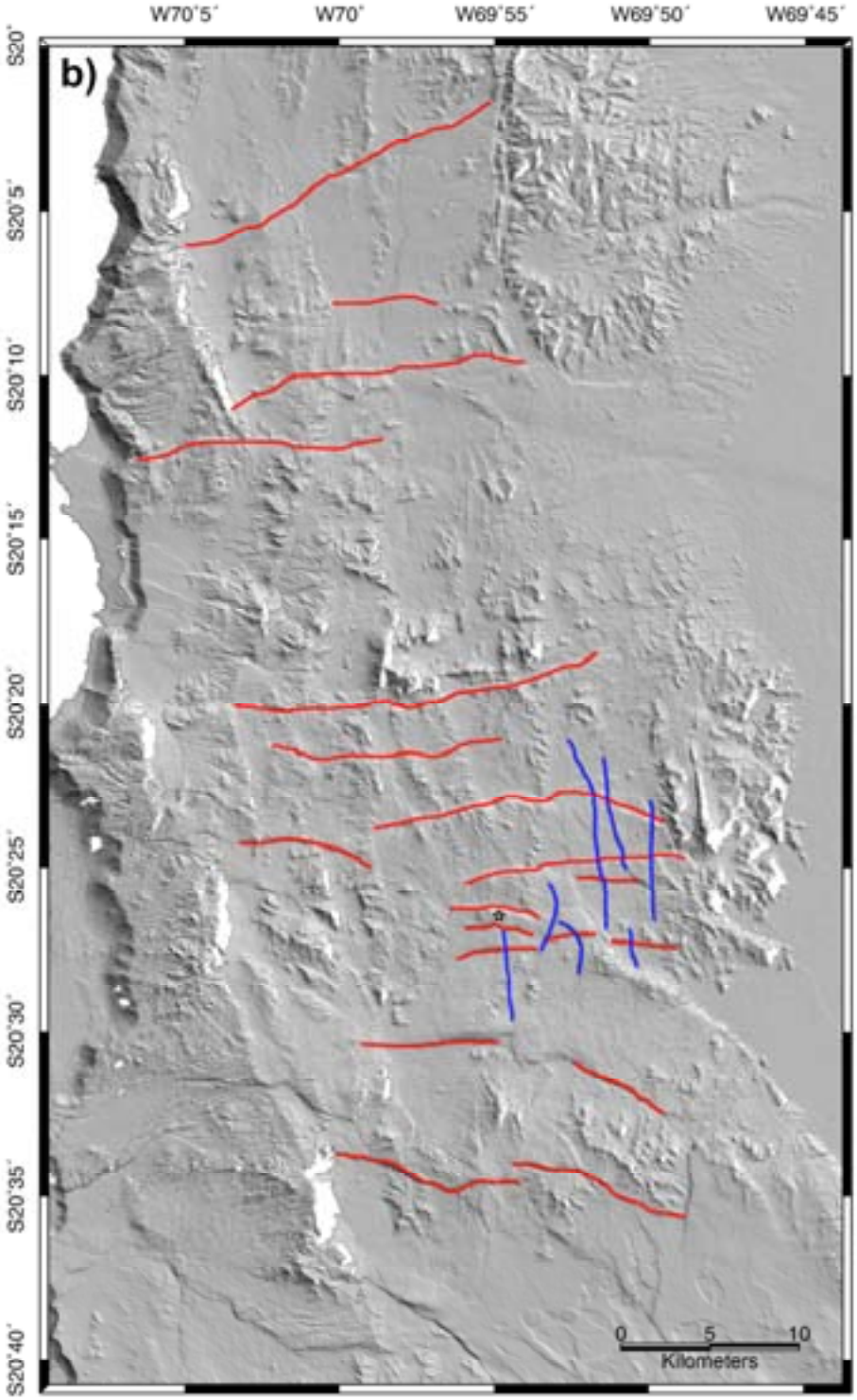

an east-west minimum principal stress. These faults were later block faulted in the latest stage of deformation. The faulting does not represent the latest stage of stress, as the motions on the faults were reactivations of the pre-existing conjugate faults. The faults in the overprinting region of the Chilean forearc are nearly at right angles to each other. It may be possible that some of the Chilean faults are also reactivations of older structures formed in a different stress regime. This is what has been observed along the AFS: Cenozoic reactivations of Mesozoic structures. The current body of knowledge on this specific area of the Chilean forearc, which lies beyond the northern terminus of the AFS, is lacking and so it is difficult to make a definitive statement about the origin of these fault scarps. However, the overprinting does establish a tentative relative chronology in episodes of deformation: old N-S faults (degraded ridges), younger E-W faults, and youngest N-S faults. Curiously, the geographic location of these overprinting faults coincides with a transition from N-S oriented faults in the south to E-W oriented faults to the north as we near the orocline.

3.5 *Summary*

Armed with a DEM and a few criteria for identifying apparent youthful scarps, we produced a fault scarp map for the north Chilean forearc. The map highlights conspicuous patterns in the faulting: 1) dominant N-S trending fault scarps controlled by the AFS and 2) limited E-W fault scarps between 19º S and 21.5º S latitude. In reviewing several factors that could be responsible for the E-W faulting and its confinement to just over 2.5 degrees of latitude in the forearc, we have eliminated climate, the AFS, and Iquique Ridge subduction.

The proximity of the zone to the oroclinal bend supports N-S compression consistent with the E-W reverse faults, though not definitively. Studies on a potential segment boundary at the Mejillones Peninsula imply that changes in the characteristics of the subduction zone at that boundary can influence fault activity and orientation. It is likely that subduction processes and physical properties of the plate interface exert considerable control on surface deformation of the continental forearc and are in part responsible for the E-W faulting zone.

REFERENCES

Allmendinger, R. W., González, G., Yu, J., Hoke, G., Isacks, B., 2005, Trench-parallel shortening in the Northern Chilean Forearc: Tectonic and climatic implications, Geological Society of America Bulletin, 117, 89-104.

Allmendinger, R. W., Smalley, R. Jr., Bevis, M., Caprio, H., Brooks, B., 2005b, Bending the Bolivian orocline in real time, Geology, 33, 905-908.

Bevis, M., Hendrick, E., Smalley, R. Jr., Brooks, B. A., Allmendinger, R. W., Isacks, B. L., 2001, On the strength of interplate coupling and the rate of back arc convergence in the Central Andes; An analysis of the interseismic velocity field, Geochemistry, Geophysics, Geosystems, 2.

Delouis, B., Philip, H., Dorbath, L., Cisternas, A., 1998, Recent crustal deformation in the Antofagasta region (northern Chile) and the subduction process, Geophysical Journal International, 132, 302-338.

Donath, F. A., 1962, Analysis of Basin-Range Structure, South-Central Oregon, Geological Society of America Bulletin, 73, 1-16.

Gephart, J., 1994, Topography and subduction geometry in the Central Andes: Clues to the mechanics of a non-collisional orogen, Journal of Geophysical Research, 99, 12279-12288.

González, G., Cembrano, J., Carrizo, D., Macci, A., Schneider, H., 2003, The link between forearc tectonics and Pliocene-Quarternary deformation of the Coastal Cordillera, northern Chile, Journal of South American Earth Sciences, 16, 321-342.

González, G., et al., 1999, The multi-phase Meso-Cenozoic slip history of the Atacama Fault System, Coastal Cordillera (21°-24° S), Northern Chile, Fourth ISAG, Goettingen (Germany), 291-295.

Hsu, J. T., 1988, Emerged Quaternary marine terraces of southern Peru: Sea level changes and continental margin tectonics over the subducting

Nazca ridge, Ph.D. thesis, pp. 310, Cornell University, Ithaca.

Loveless, J., and Allmendinger, R. W., 2005, Implications of elastic dislocation modeling on permanent deformation in the northern Chilean forearc, paper presented at 6th International Symposium on Andean Geodynamics (ISAG 2005), Barcelona.

McCaffrey, R., 1996, Estimates of modern arc-parallel strain rates in fore arcs, Geology, 24, 27-30.

Roperch, P., Mpodozis, C., Fernandez, R., Arrigada, C., 1999, Tectonic rotations in northern Chile; implications for the geodynamic evolution of the southern Central Andes during the Tertiary, EOS Transactions American Geophysical Union, 80, 1060.

Rosenbaum, G., Giles, D., Saxon, M., Betts, P. G., Weinberg, R. F., Duboz, C., 2005, Subduction of the Nazca Ridge and the Inca Plateau: Insights into the formation of ore deposits in Peru, Earth and Planetary Science Letters, 239, 18-32.

Sobiesiak, M., 2005, Fault Plane Structure of the 1995 Antofagasta Earthquake (Chile) Derived From Local Seismological Parameters, pp. 137, University of Potsdam, Potsdam.

Victor, P., and Sobiesiak, M., 2005, Interaction of the subduction process and forearc tectonics: An example from the active N-Chilean margin, EOS Transactions American Geophysical Union, 86, Abstract T33C-0569.

CHAPTER 4

INVERSE DIFFUSION MODELING OF FIELD- AND DEM-EXTRACTED FAULT SCARP PROFILES: NORTHERN CHILE

4.1 *Introduction*

A high resolution DEM derived from satellite radar interferometry is only as useful as its accuracy. The ground-truthing process for the DEM in this dissertation was originally based on 1:50,000 Chilean topographic maps and the 90-meter DTED topography. In June 2001, measurements were taken in the field to compare with the DEM. Statistically good agreement means that we can use the DEM almost as effectively as field measurements for structures with offsets greater than three times the standard deviation of the DEM's relative vertical uncertainty to conduct morphological studies of the north Chilean forearc. In this chapter we describe the field data collection and processing, review inverse scarp diffusion modeling and apply it to our data, and discuss the implication of the modeling results for the study area.

4.2 *Field Measurements*

Field examination of a sampling of fault scarps identified in the digital elevation model (DEM) from Chapter 2 revealed highly weathered bedrock outcrops where any outcrops existed. Several of the scarps studied in the region could be characterized as debris slopes close to the angle of repose. The scarp

faces were relatively smooth and had rounded crests, with only occasional widely spaced rills disrupting an otherwise continuous surface. This suggests little development of an advective erosional system where fluvial and eolian processes would typically carry detritus away from the scarp. The structures are sitting in the accumulation of their own debris, which is known as a transport-limited system. Transport-limited systems are common in tropical climates where rates of bedrock weathering (soil production) exceed rates of soil transport. The other extreme occurs when weathering cannot keep up with soil transport resulting in a scarp face of bare rock that is usually quite steep -- a weathering-limited setting (Carson and Kirby, 1972). The Atacama Desert provides a transport-limited environment due primarily to hyper-arid conditions. The main forces at work on the degradation of the scarps are creep (movement as a result of gravity) and the infrequent slope wash from rare rainfall events. There is a dense coastal fog prevalent in the Atacama Desert known locally as the Camanchaca. It is particularly active in the winter months and inundates the western edge of the Coastal Cordillera, providing moisture and creating layers of gypcrete, a cement of gypsum and the local gravels (Rech et al., 2003). We encountered gypcrete on slopes and in camp that ranged from thin, easily broken sheets to layers that could not be penetrated with a rock hammer and extended laterally for over a hundred meters.

Profiles were measured in June 2001, over nine scarps near coastal towns: Pisagua (2), Iquique (3), Antofagasta (1), and in an inland location between Pisagua and Iquique (3) (Figure 4.1). Figure 4.2 shows close-ups of the locations on Landsat TM (Thematic Mapper) imagery, the DEM, and in field

photos when available. First-order site selection was based on the identification of prominent and continuous scarps in the DEM with moderate offsets on the order of tens of meters. The next criterion was accessibility to the scarp with a four-wheel drive vehicle. Due to the limited battery life of the equipment, 3-4 profiles were measured across scarps with offsets no larger than 60 meters. Profiles were chosen on sections of the scarp that were representative of overall scarp morphology. We avoided selecting those scarps with highly variable morphology (e.g. splays or channel downcutting). We marked and measured approximately 3-4 lines, 20-40 meters apart, with a tripod-mounted laser range finder aimed at a corner cube reflector held by a field assistant. Readings were recorded every 3 meters along each profile path. We measured profile locations with a Garmin GPS handheld receiver.

The profile data collected by the laser range finder was converted from spherical coordinates to Cartesian coordinates. The discreet points recorded for each profile deviated from a perfectly linear plot (perpendicular to the scarp) due to small-scale obstacles for the individual walking the transect. This resulted in lateral noise on the order of a meter or less. A least-squares best-fit vertical plane was calculated for each profile line. The discreet points were then projected onto the best-fit plane to eliminate any lateral noise in the profile. All of the profiles are shown in Figure 4.3, first in a 3-dimensional perspective and then projected onto the plane perpendicular to the strike of the scarp. They are named according to the chronological order they were measured. Table 4.1 lists the profiles and their corresponding GPS location, bearing, and length.

Figure 4.1 Location map of field profiles. The black boxes outline the four areas along the Coastal Cordillera of northern Chile where field profiles were measured. Box A is near Pisagua where profiles 7 (north) and 8 (south) were recorded. Box B covers the section of overprinting faults discussed in Chapter 3 and contains profiles 4, 5, and 6. Profiles 1 (center), 2 (north), and 3 (south) are located in box C which lies south of Iquique and includes the Salar Grande region. Profile 9 was measured south of Antofagasta as denoted by box D. The red points re the locations of the profiles scarp sites.

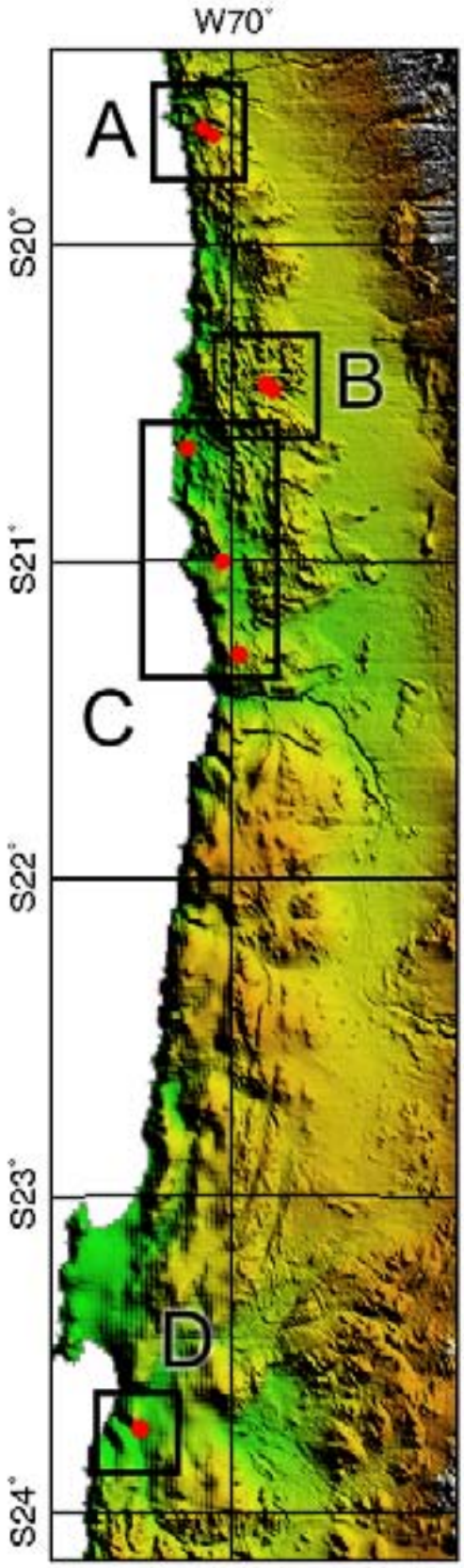
W70°
S20°
S21°
S22°
S23°
S24°
A
B
C
D

Figure 4.2 TM, DEM, and field photos of scarp locations. Each profile site from Figure 4.1 is shown in close-up satellite view on Landsat 5 TM imagery. All profiles are marked on the DEM except scarp 1 which is marked on the Ikonos imagery because the scarp lies in a zone of no data in the DEM (radar shadow). Field photos, if available, are shown of each scarp with a field assistant for scale on scarps 1, 2, and 9. A green line traces the typical profile on each field photos except in d where the profile is behind the hill and denoted by green arrows. The viewing angle of the field photo is depicted by the eye symbol on the Ikonos or DEM images.

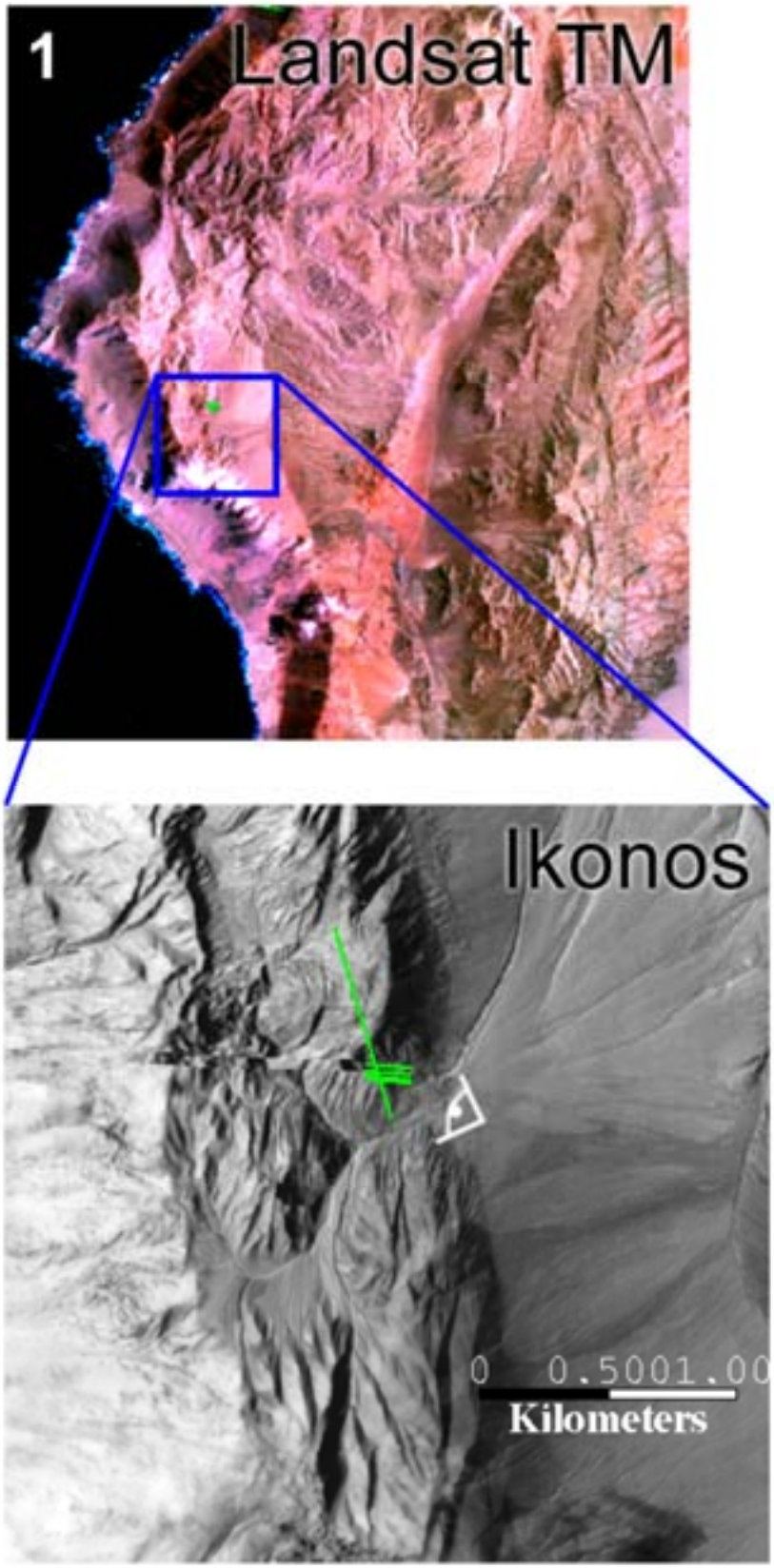
1
Landsat TM
Ikonos
0 0.5001.00
Kilometers

Figure 4.2 (Continued)

Figure 4.2 (Continued)

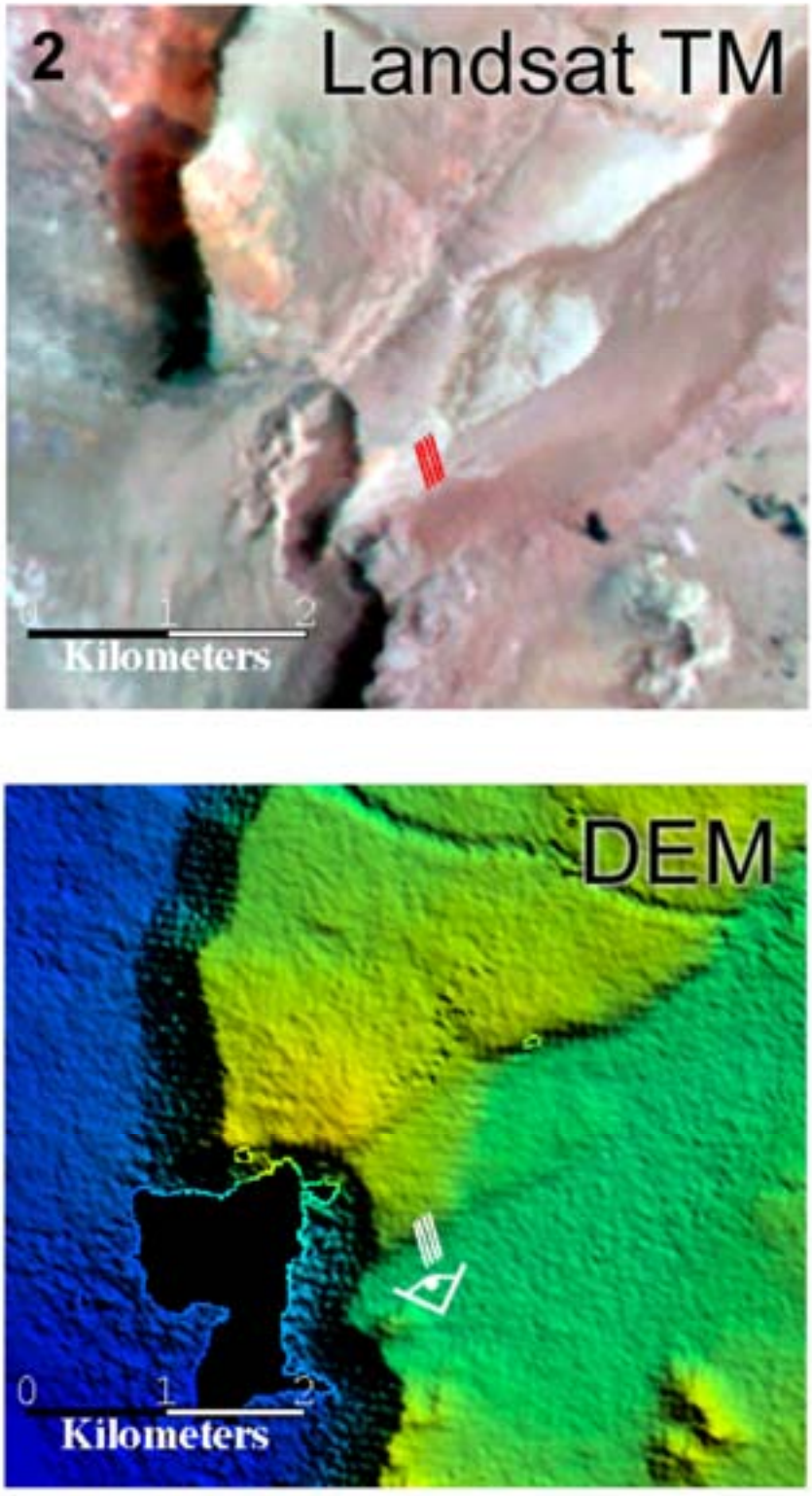

Figure 4.2 (Continued)

Figure 4.2 (Continued)

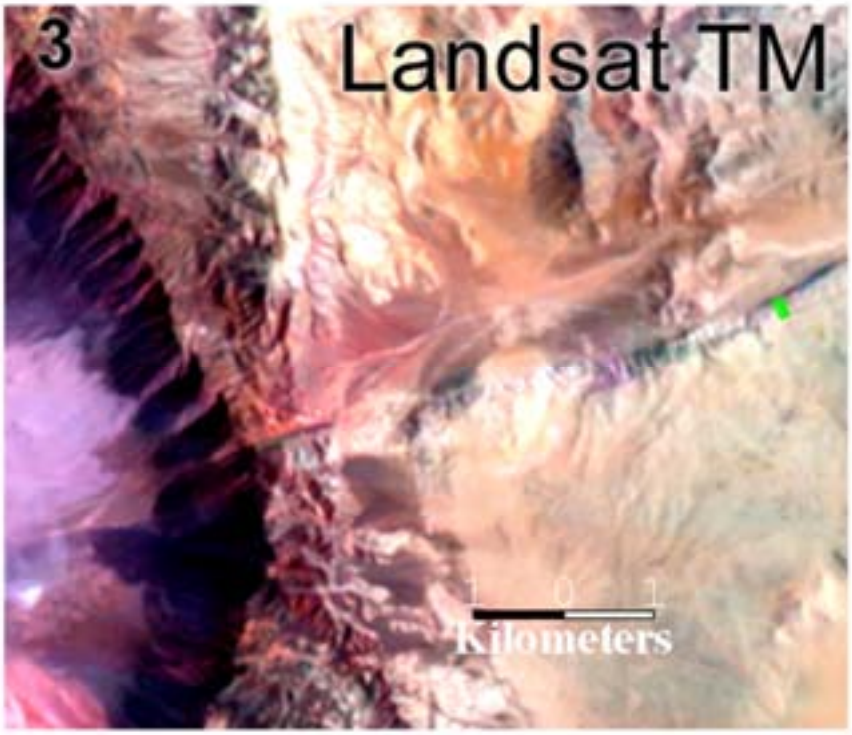

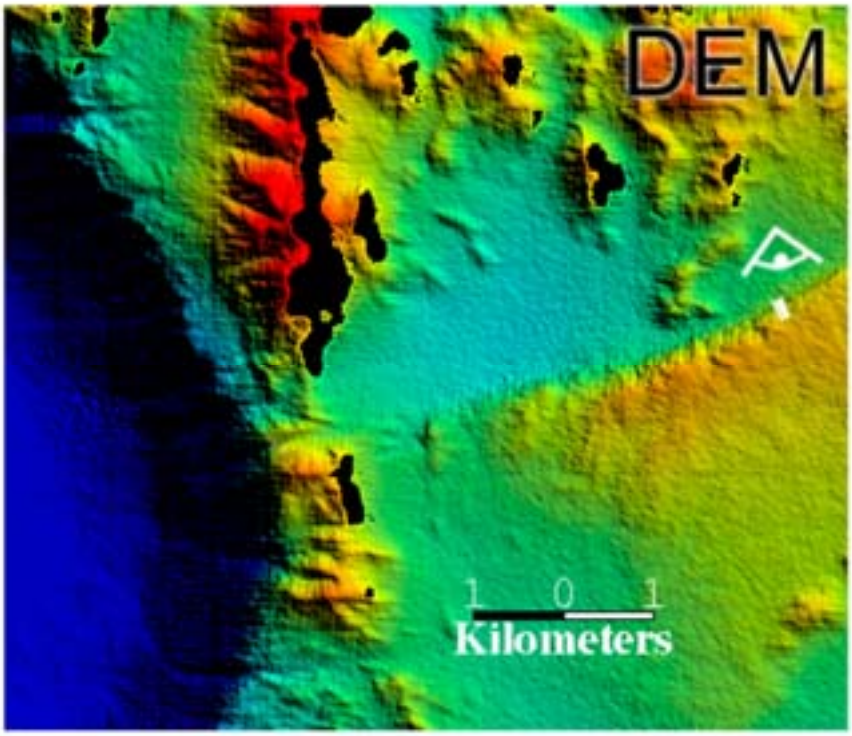

Figure 4.2 (Continued)

Figure 4.2 (Continued)

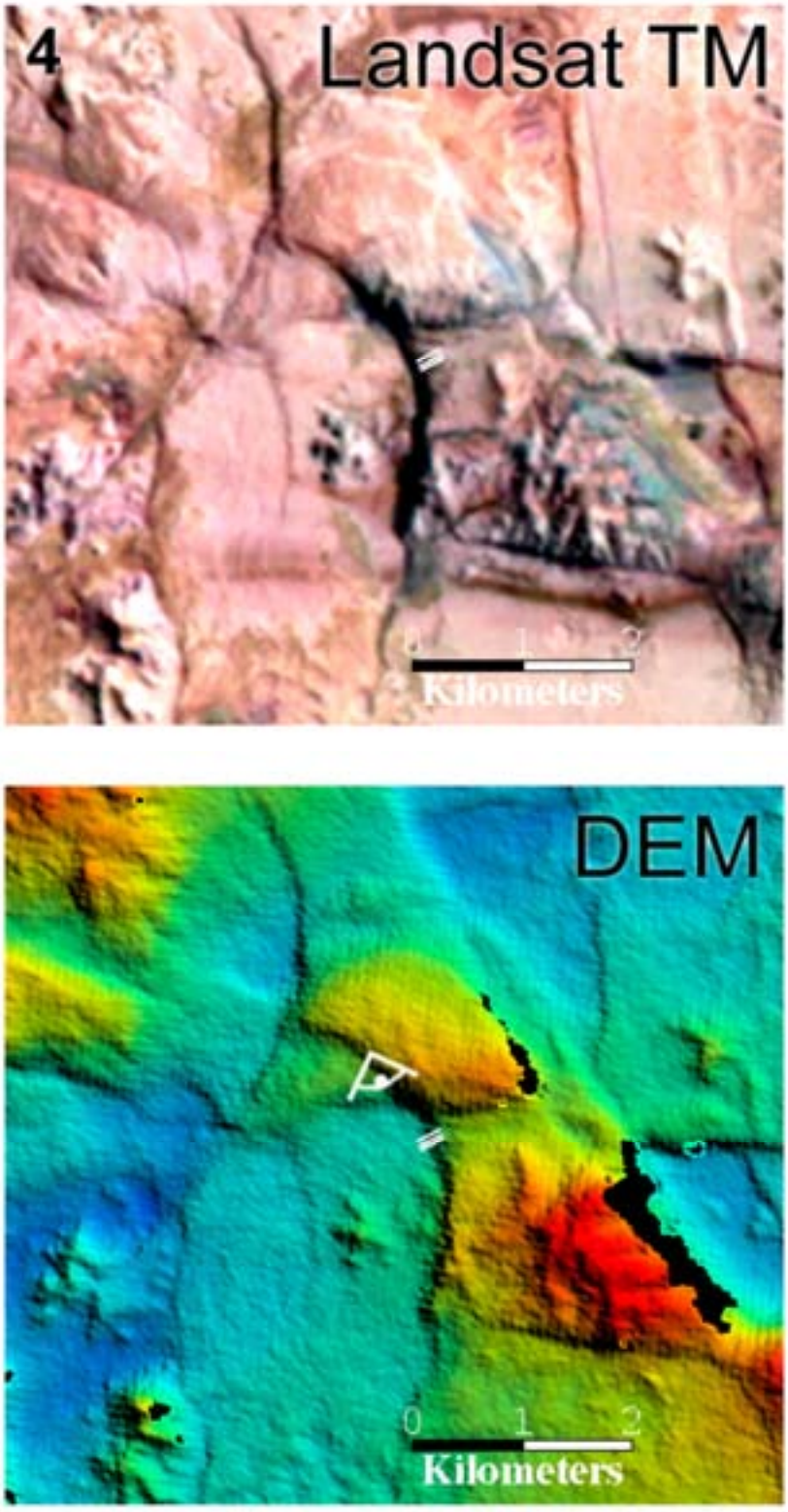

Figure 4.2 (Continued)

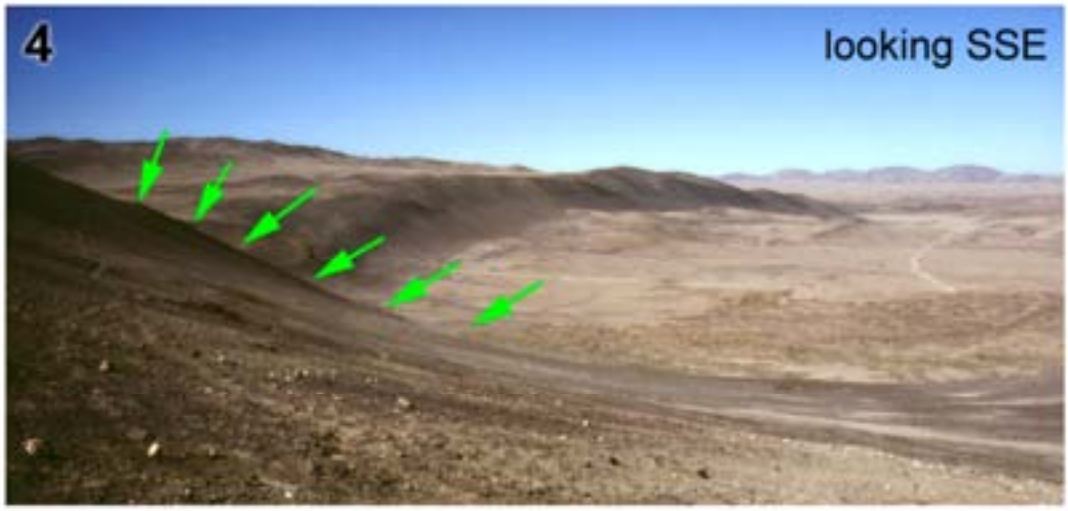

Figure 4.2 (Continued)

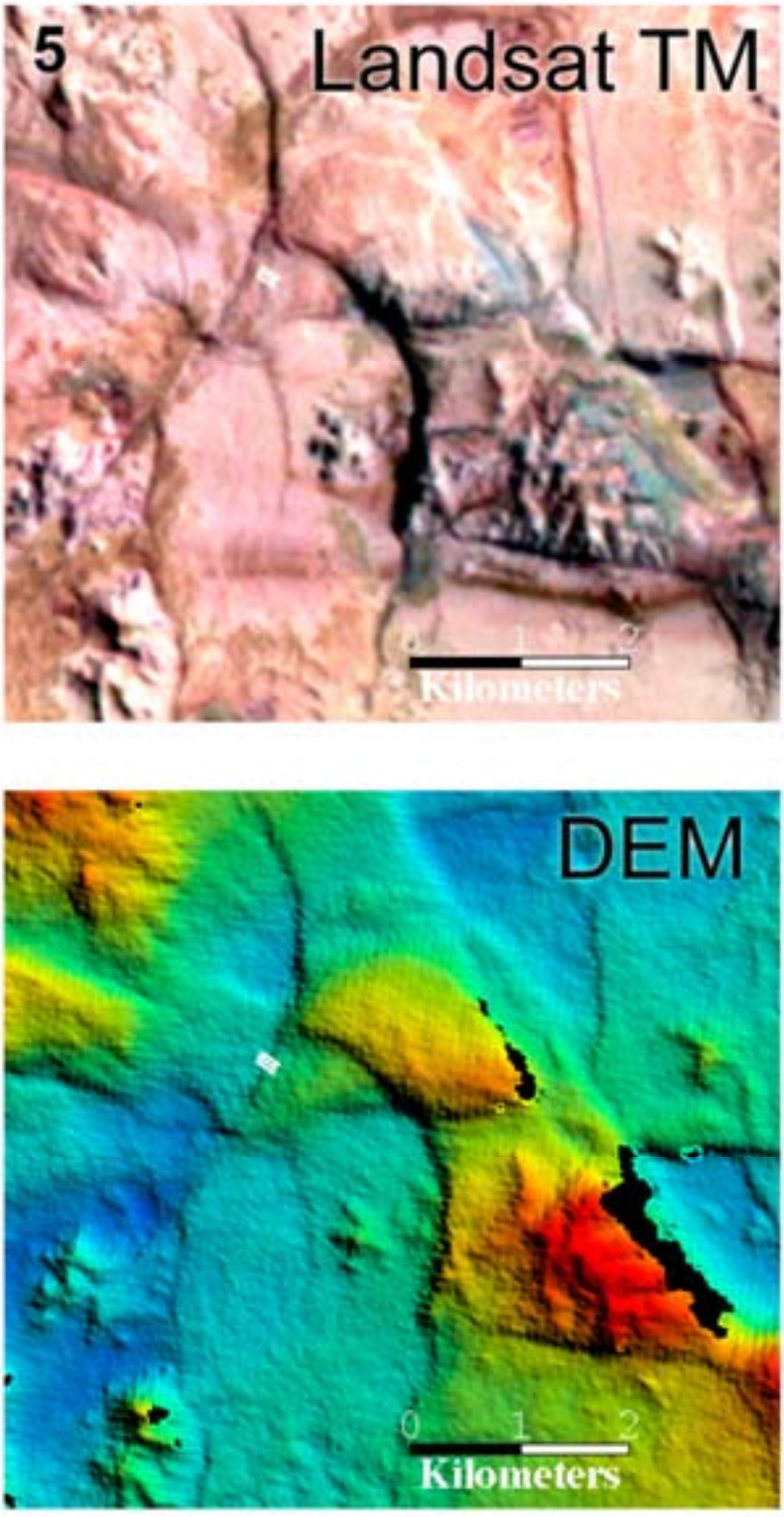

Figure 4.2 (Continued)

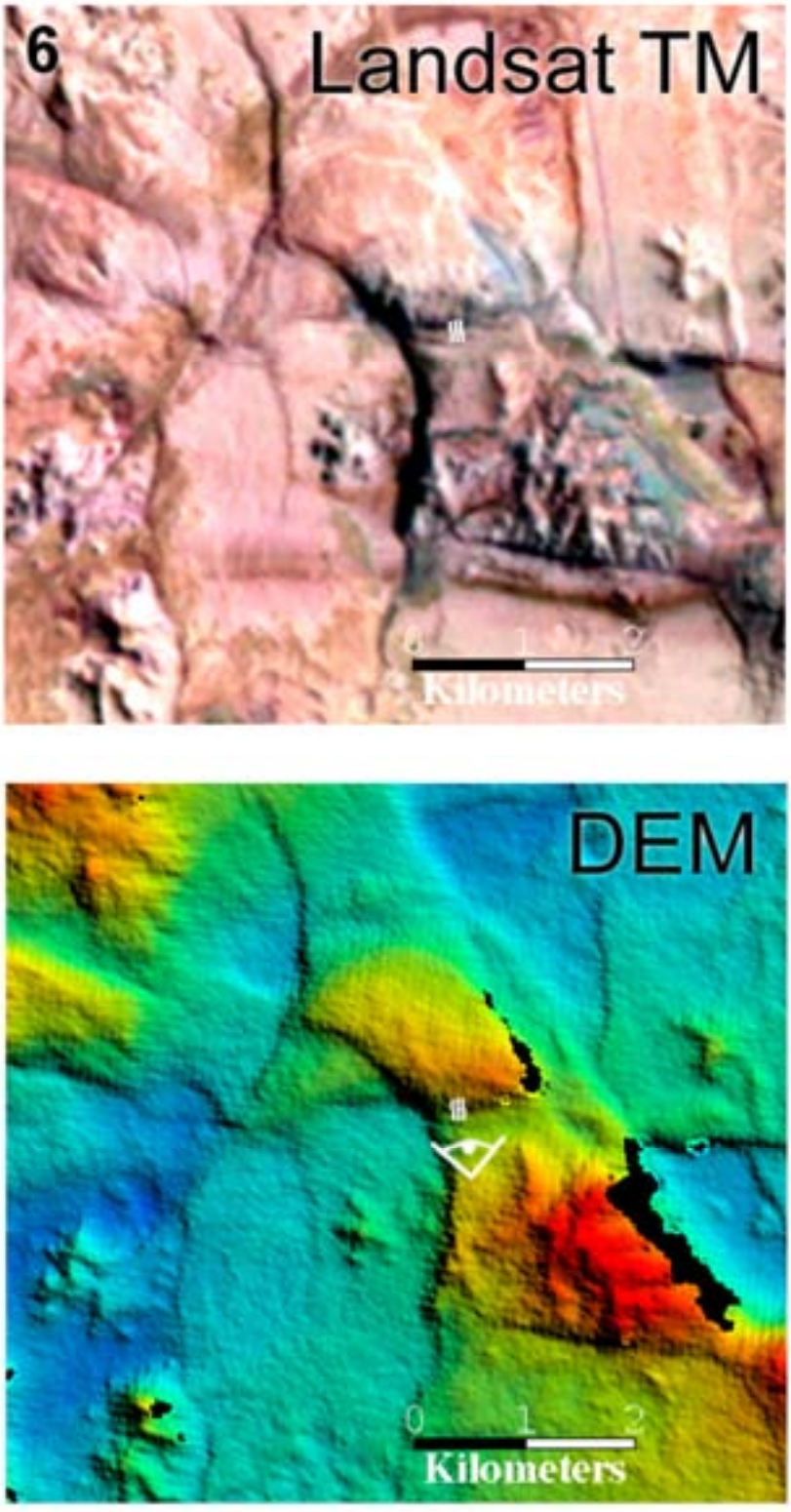

Figure 4.2 (Continued)

Figure 4.2 (Continued)

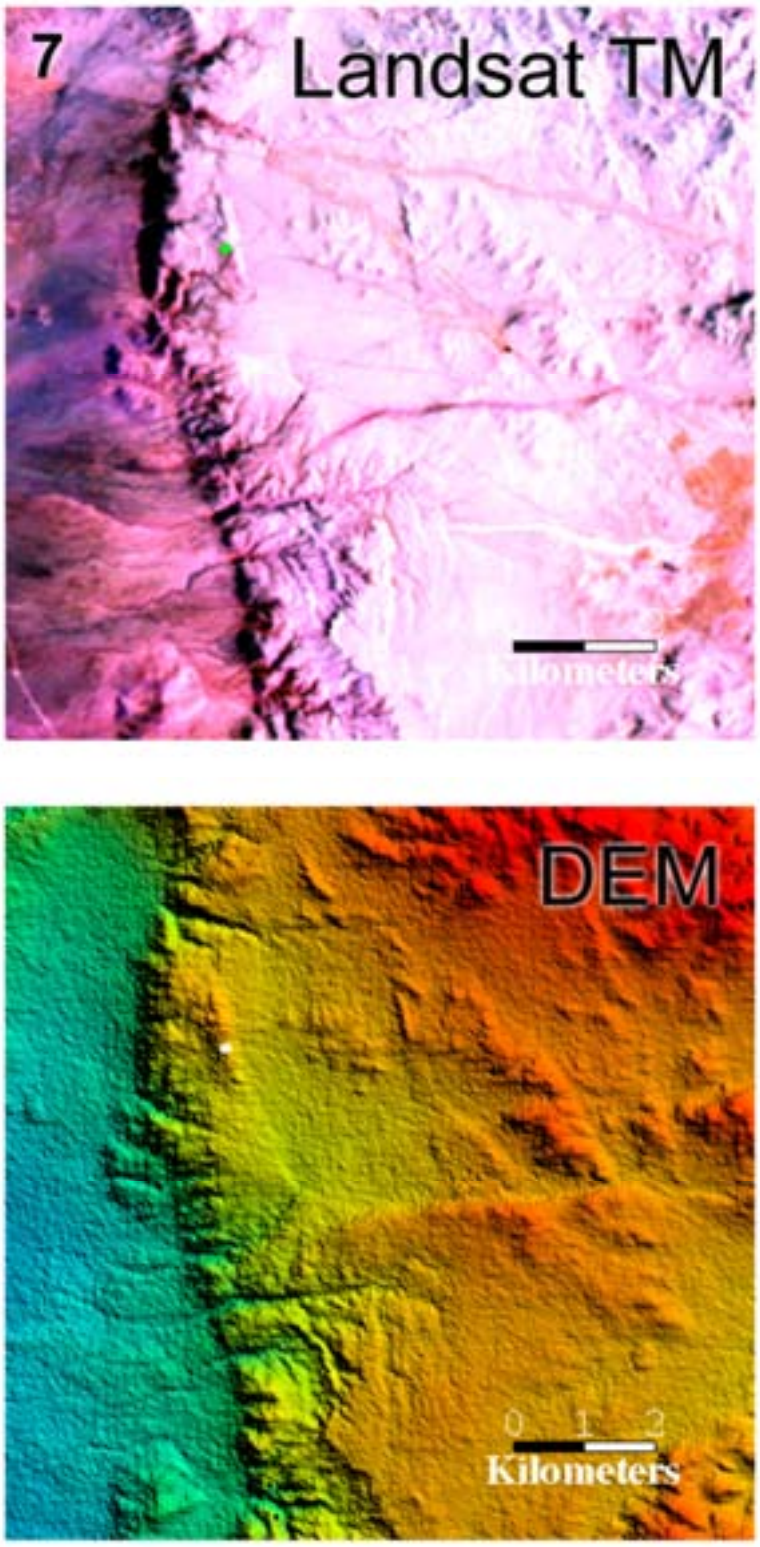

Figure 4.2 (Continued)

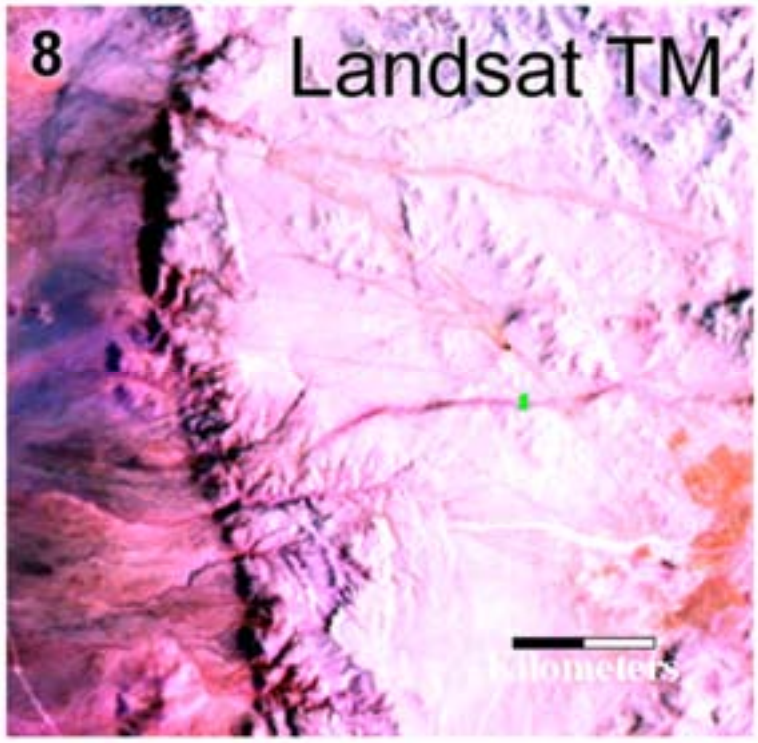

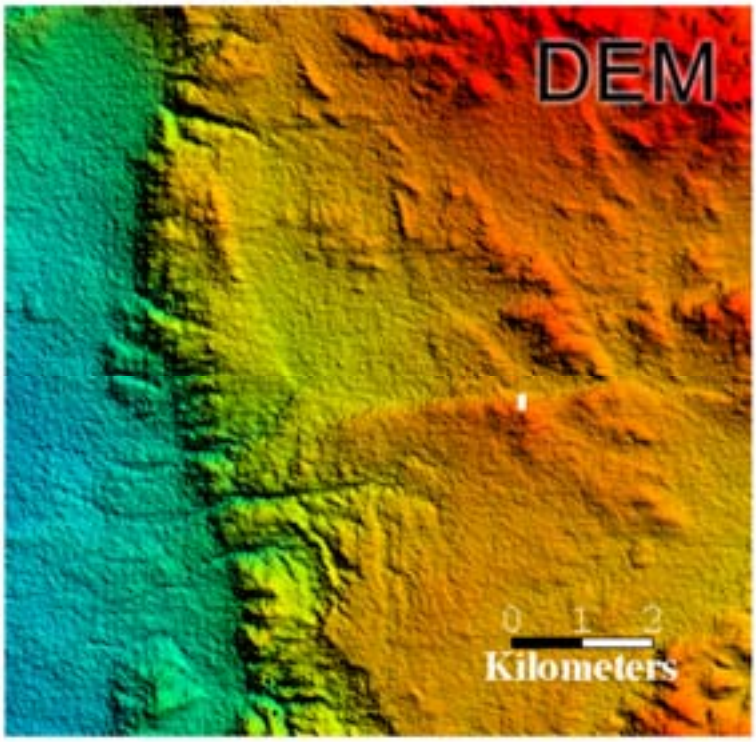

Figure 4.2 (Continued)

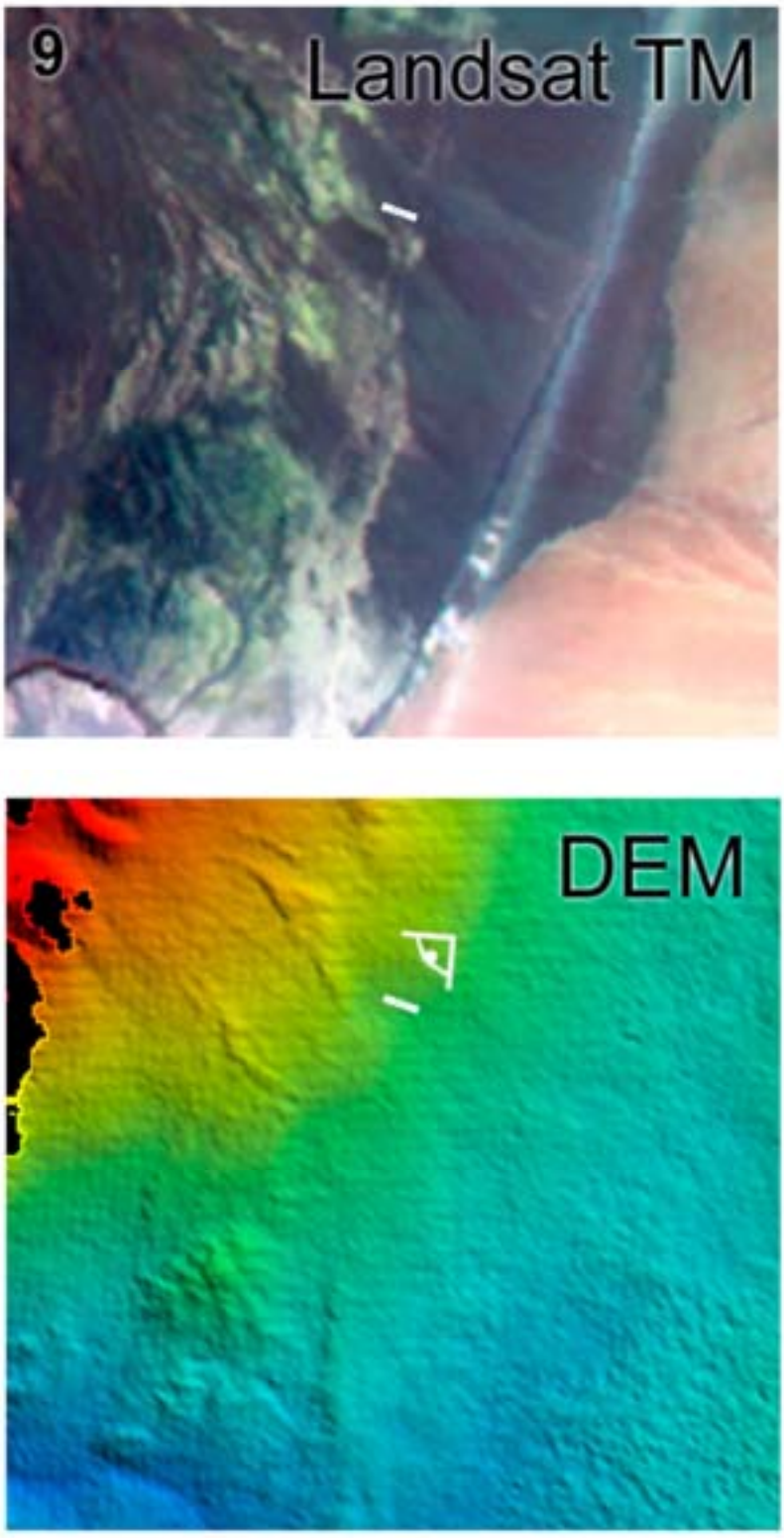

Figure 4.2 (Continued)

Figure 4.3 Plotted scarp profiles for all field sites. The three-dimensional perspective views have axes of horizontal distance along-strike of the profiles, height, and lateral offset from the zero-point (the GPS location for the site). The two-dimensional views are created by projecting the profiles onto the vertical plane of the height versus the distance along-strike of the profile. Units listed are in meters.

Scarp 1 Profiles

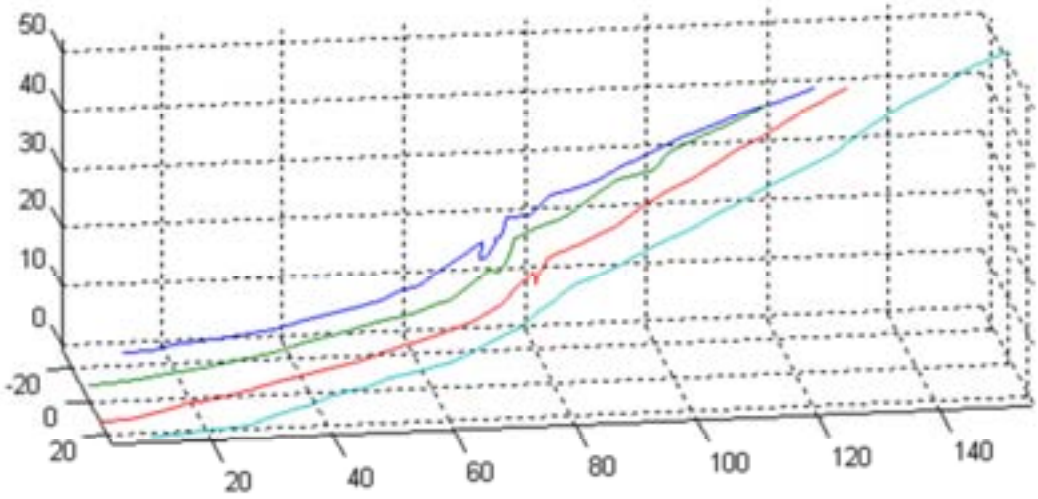

1a - blue 1b - green 1c - red 1d - cyan

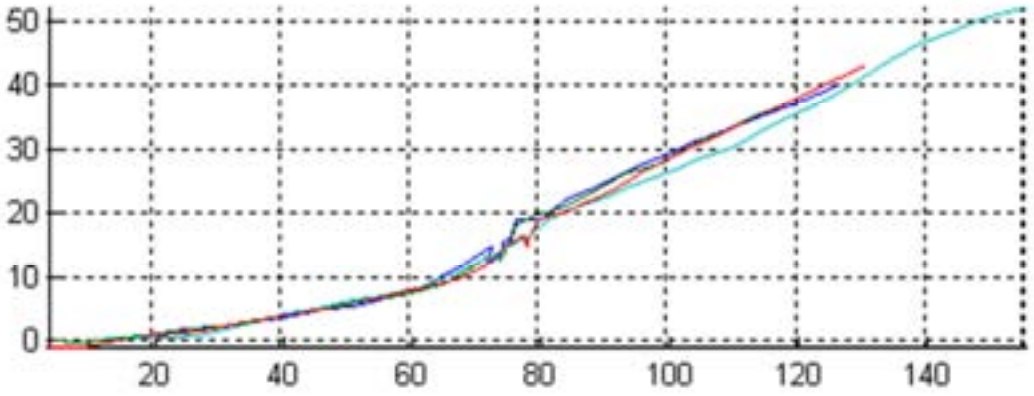

Figure 4.3 (Continued)

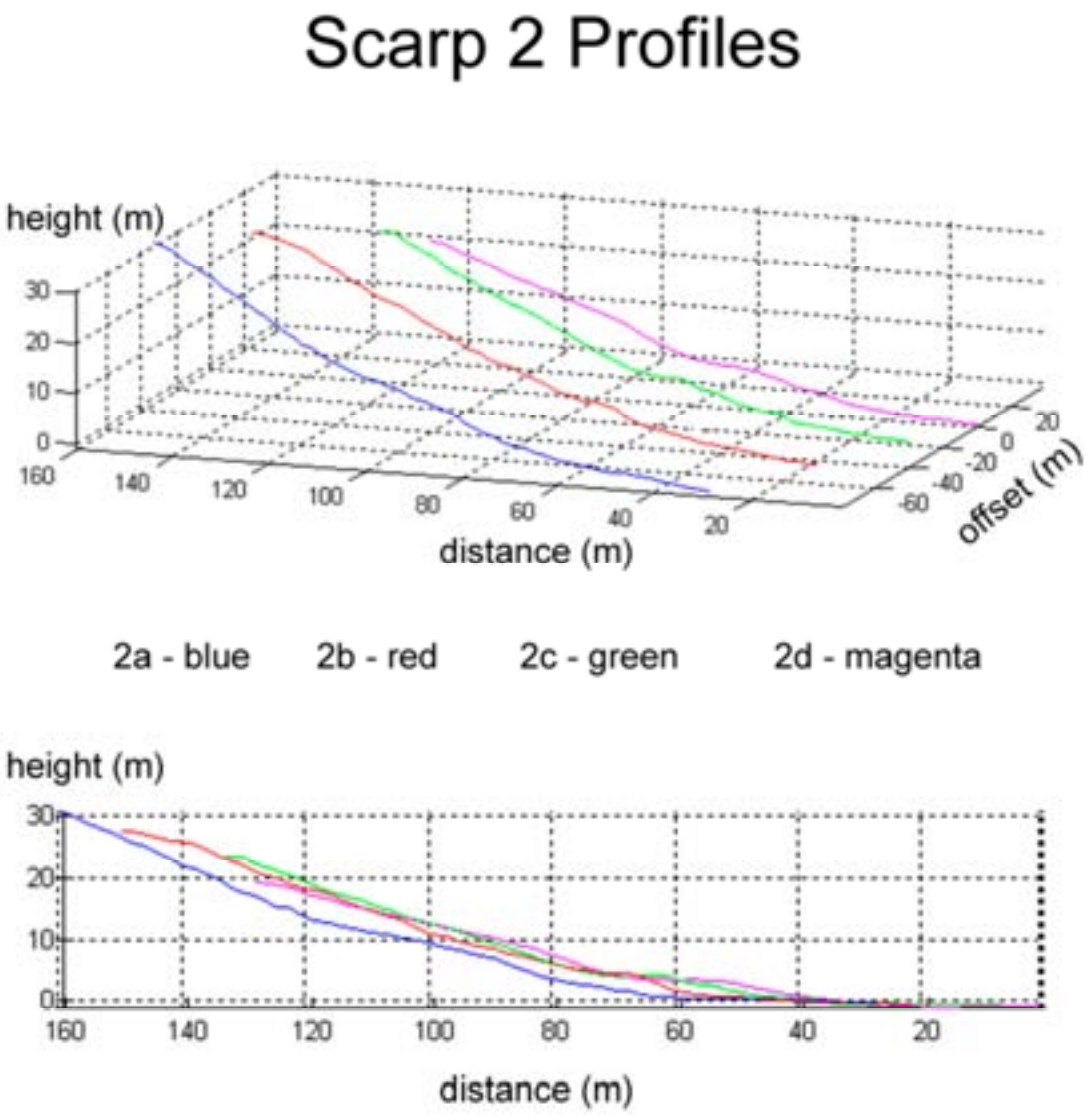

Figure 4.3 (Continued)

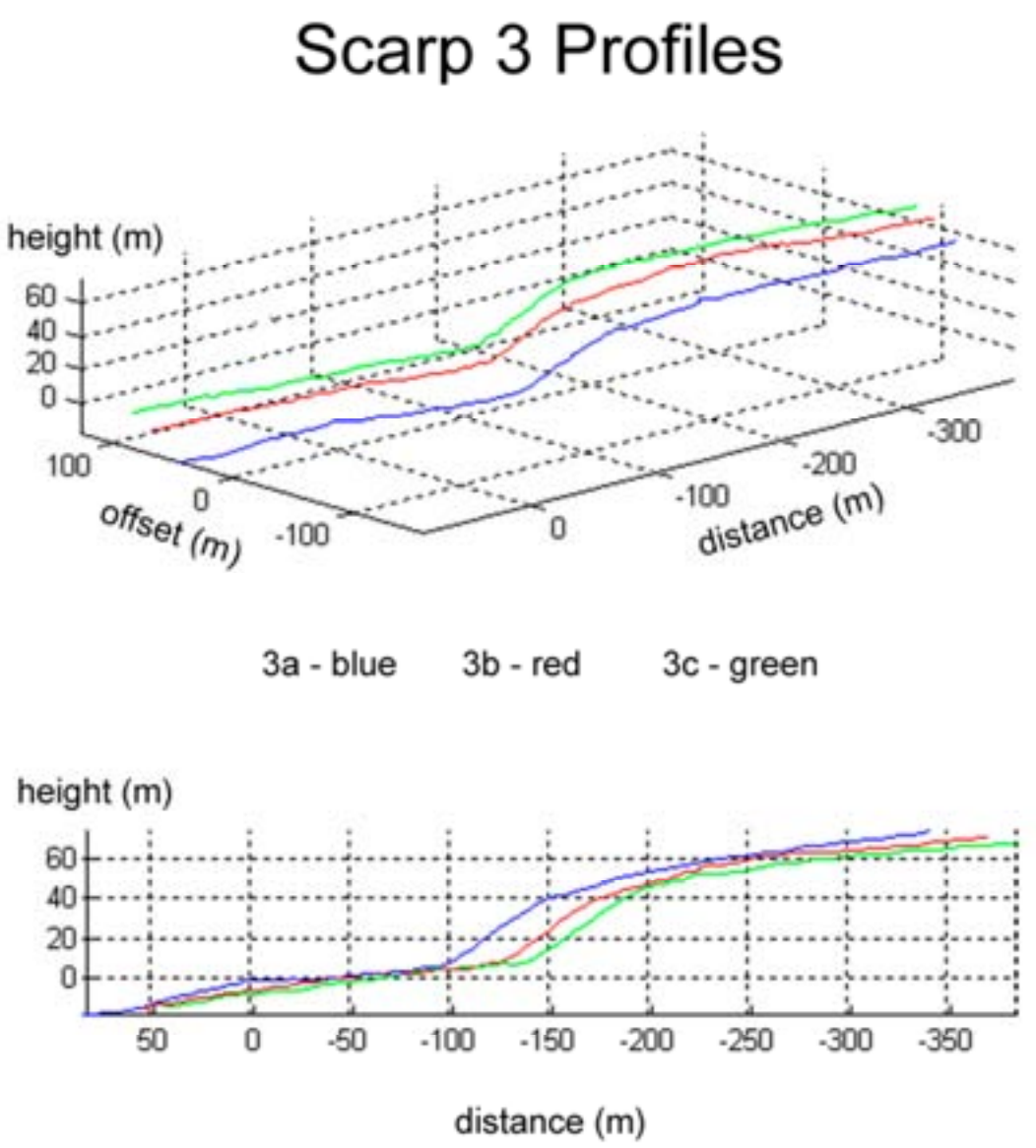

Figure 4.3 (Continued)

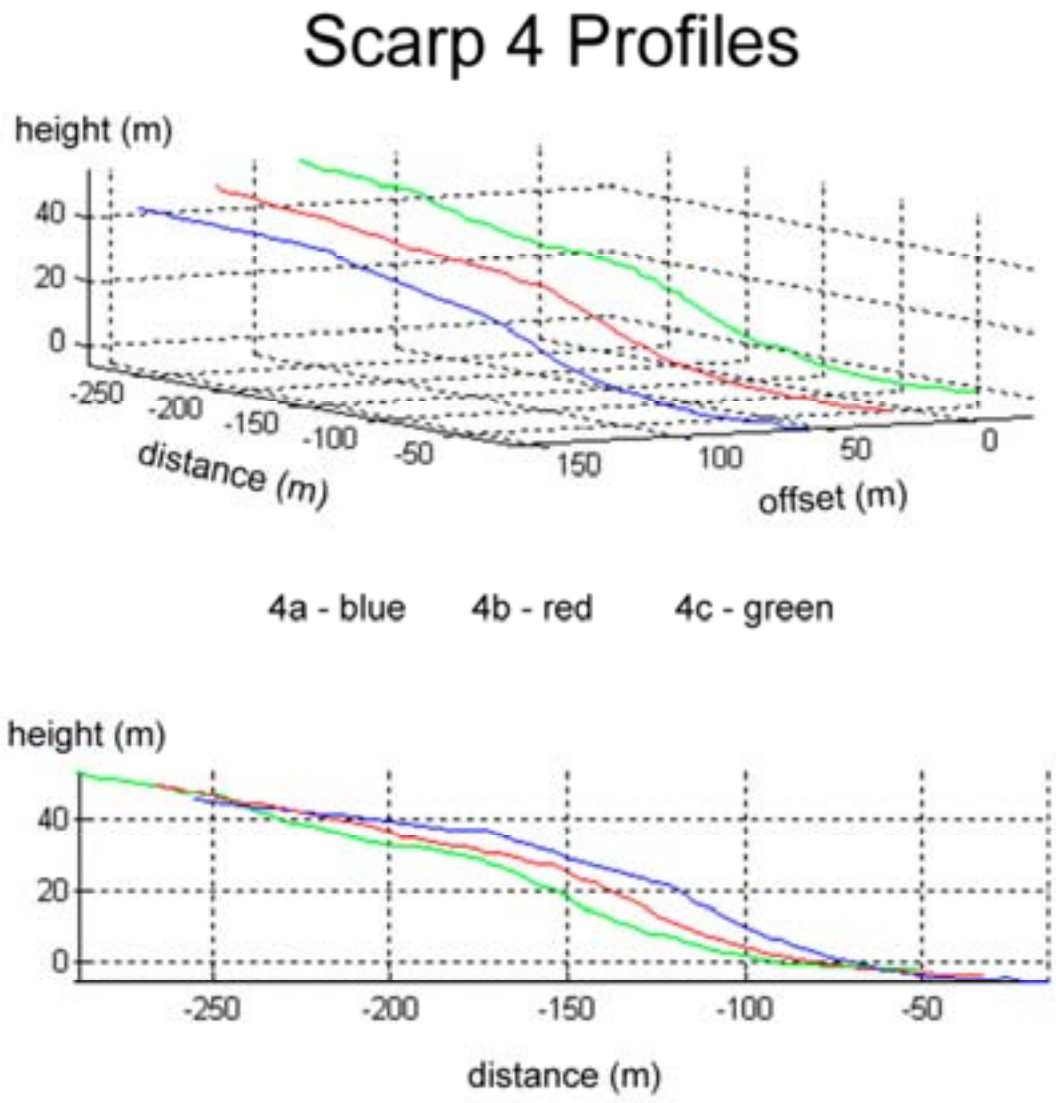

Figure 4.3 (Continued)

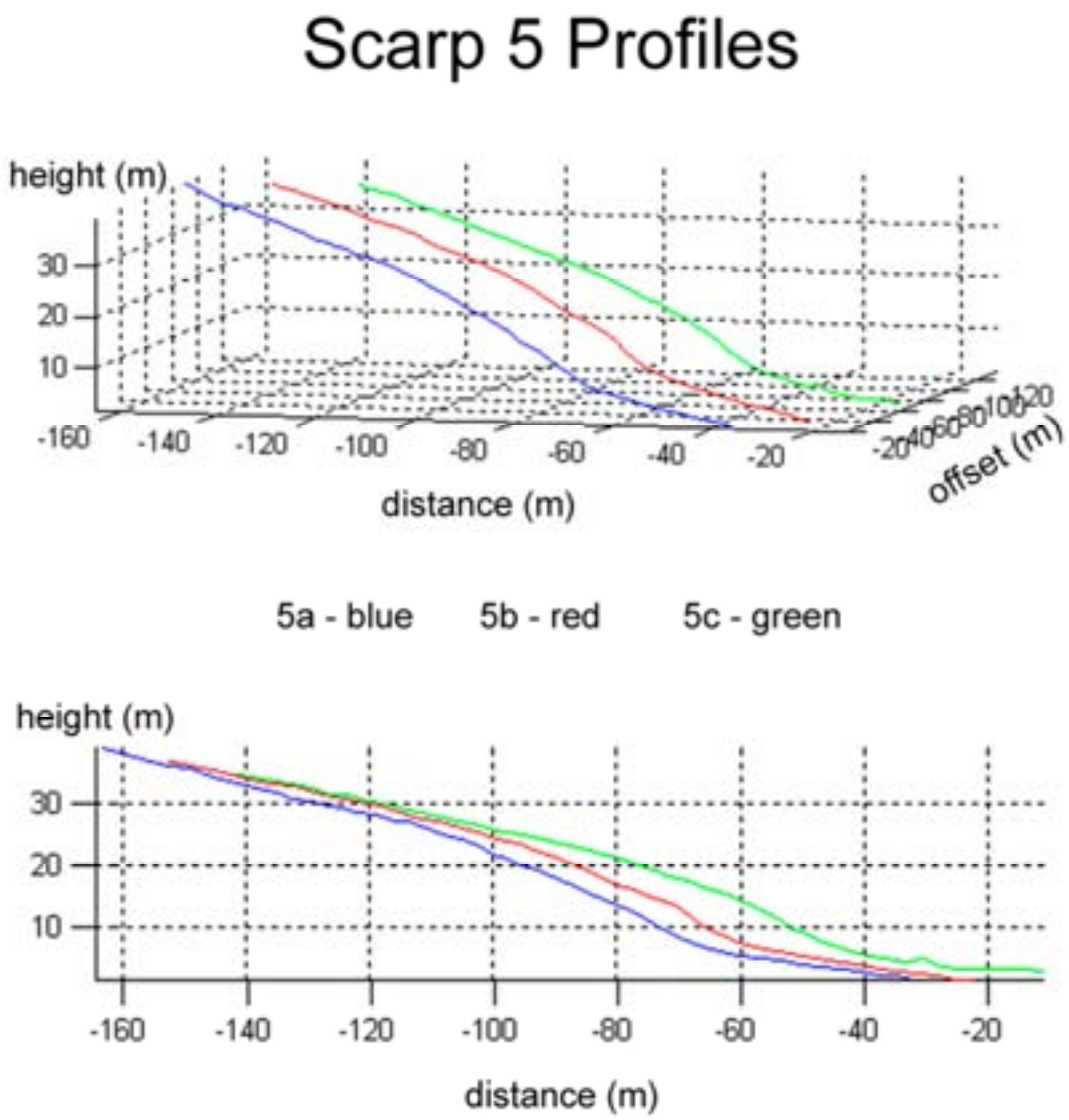

Figure 4.3 (Continued)

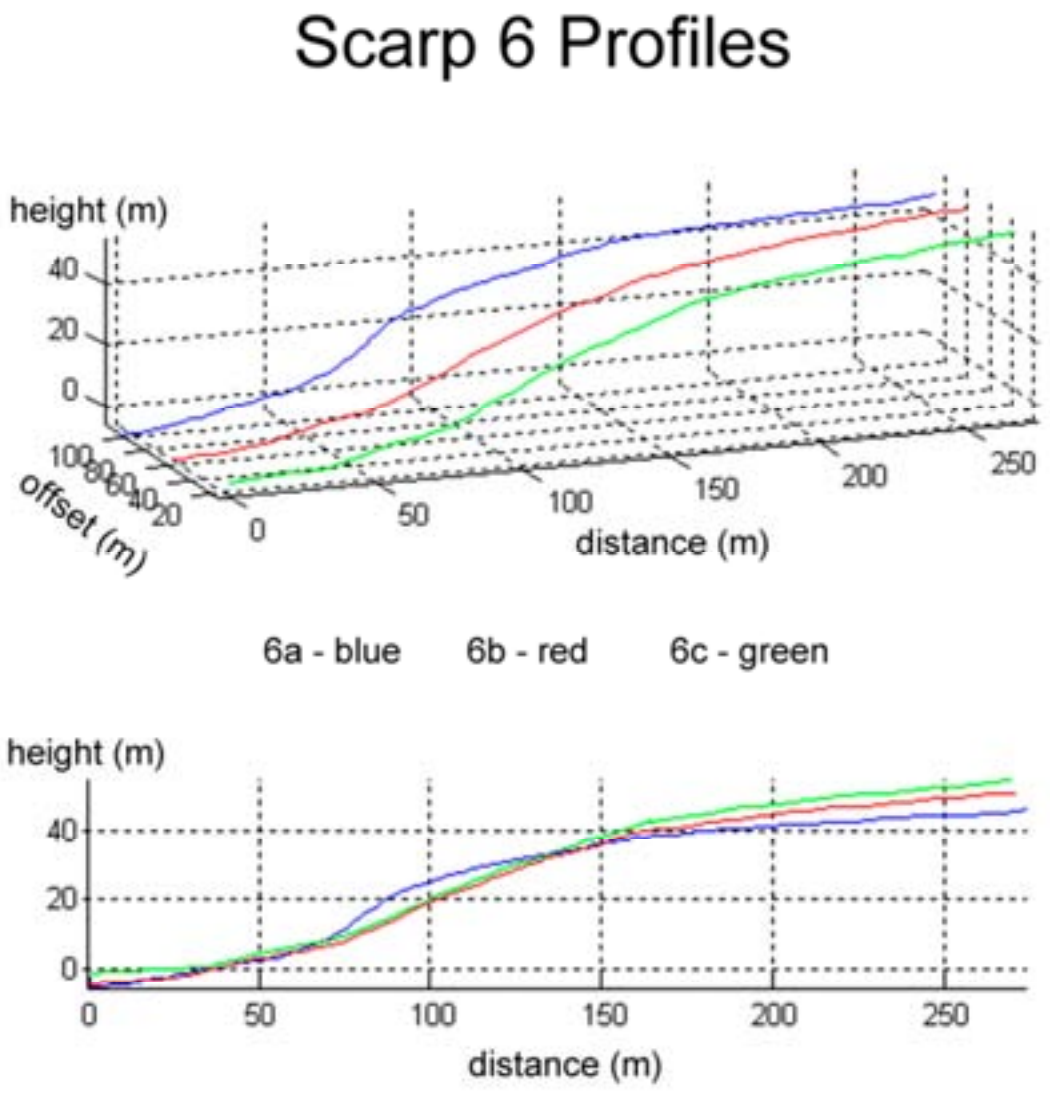

Figure 4.3 (Continued)

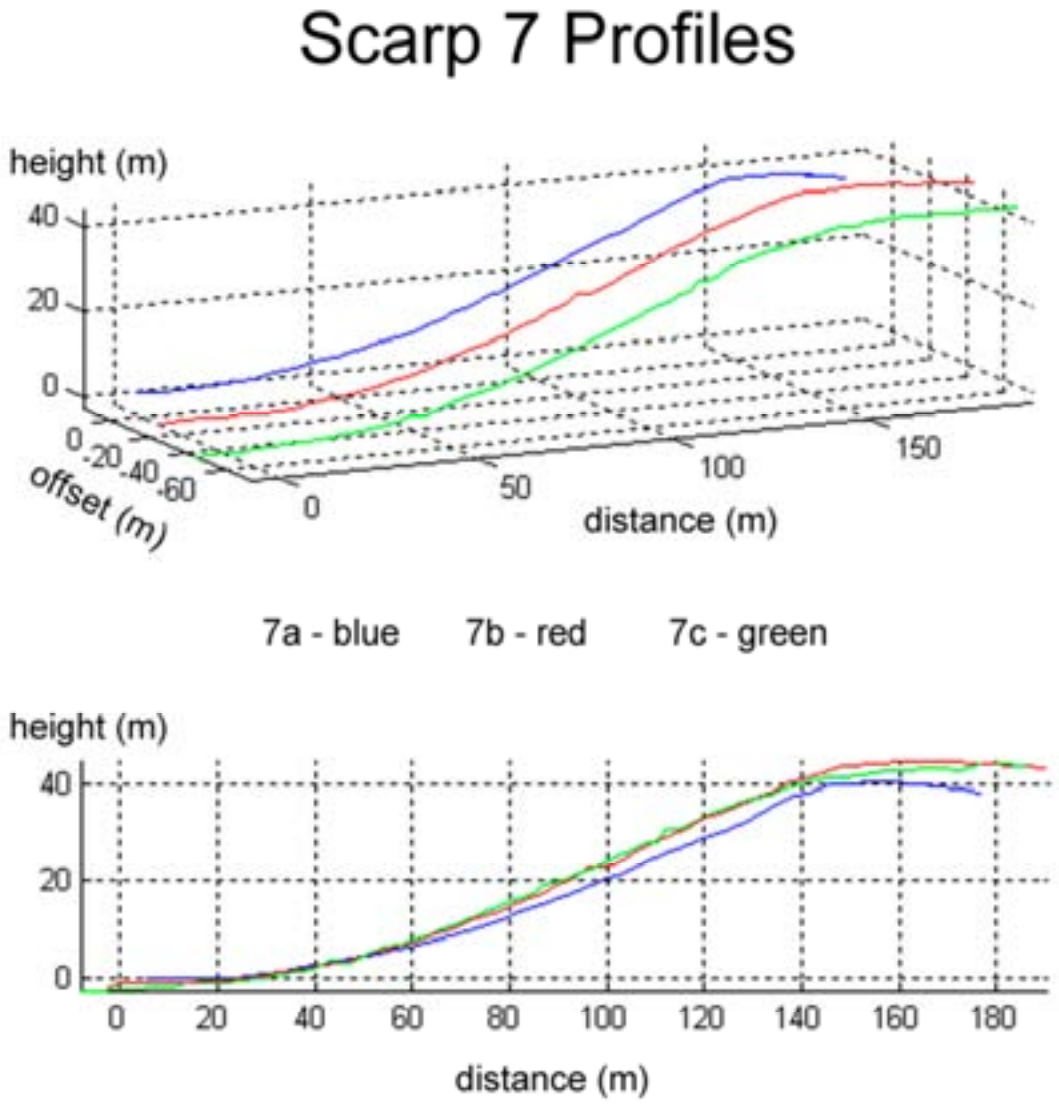

Figure 4.3 (Continued)

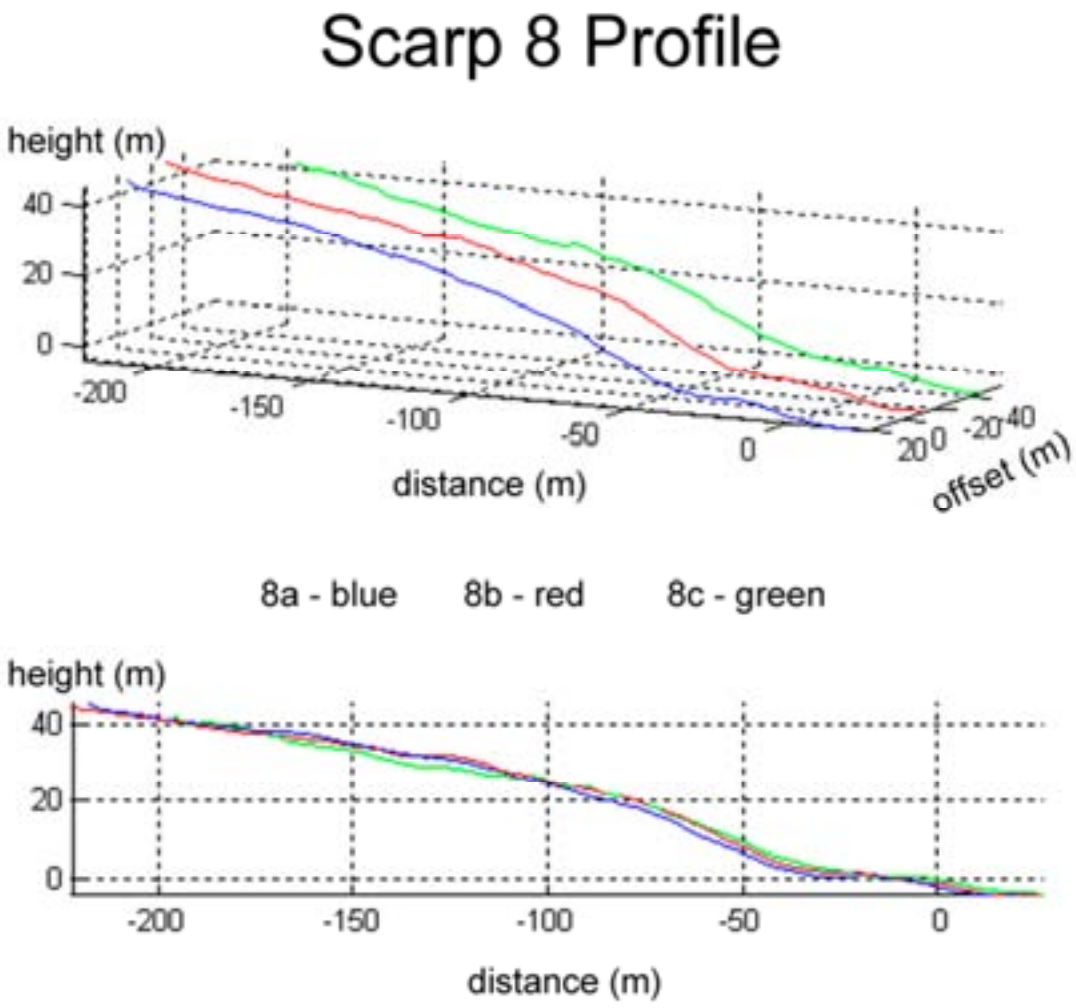

Figure 4.3 (Continued)

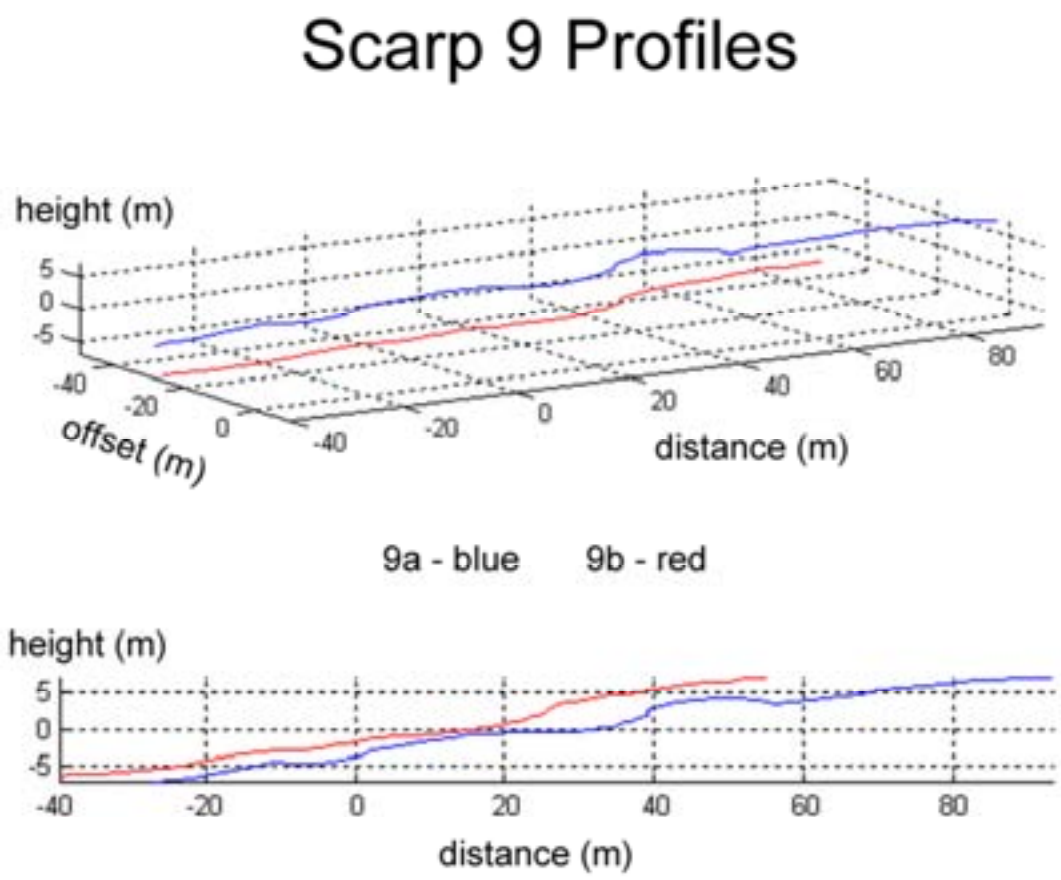

Table 4.1 Field Scarp Profiles Measured

Profile	Location	Bearing	Length (m)
1a	21.0387º S, 70.1299º W	275º	113.9
1b	21.0387º S, 70.1299º W	275º	115.9
1c	21.0387º S, 70.1299º W	275º	129.9
1d	21.0387º S, 70.1299º W	275º	147.5
2a	21.0404º S, 70.1303º W	345º	139.6
2b	21.0404º S, 70.1303º W	345º	139.7
2c	21.0404º S, 70.1303º W	345º	132.9
2d	21.0404º S, 70.1303º W	345º	132.4
3a	20.6376º S, 70.1561º W	155º	470.4
3b	20.6376º S, 70.1561º W	155º	473.7
3c	20.6376º S, 70.1561º W	155º	474.2
4a	21.2886º S, 69.9763º W	70º	262.9
4b	21.2886º S, 69.9763º W	70º	257.4
4c	21.2886º S, 69.9763º W	70º	260.6
5a	20.4568º S, 69.8764º W	300º	146.5
5b	20.4568º S, 69.8764º W	300º	148.3
5c	20.4568º S, 69.8764º W	300º	149.5
6a	20.4453º S, 69.8890º W	0º	278.2
6b	20.4453º S, 69.8890º W	0º	272.6
6c	20.4453º S, 69.8890º W	0º	268.5
7a	19.6369º S, 70.1056º W	80º	172.2
7b	19.6369º S, 70.1056º W	80º	195.0
7c	19.6369º S, 70.1056º W	80º	196.4
8a	19.6562º S, 70.0647º W	355º	241.2
8b	19.6562º S, 70.0647º W	355º	248.2
8c	19.6562º S, 70.0647º W	355º	223.9
9a	23.7331º S, 70.3125º W	290º	128.7
9b	23.7331º S, 70.3125º W	290º	103.3

4.3 *Comparison with DEM*

The collection of scarp profiles in the field was an important step in validating the quality of the DEM. Comparing the profiles with corresponding DEM transects based on GPS locations and profile bearings, we find good agreement between the two datasets at the scarp faces where blue is the DEM transect and red is the field profile (Figure 4.4). It should be noted that this comparison is focused on how well the two datasets correspond in scarp shape and not on absolute elevation because the altimetry readings of the handheld GPS were not reliable. The two plots were aligned at the inflection point on the face of the scarp. The field profiles tend to diverge from the DEM the further we move from the scarp face. Our lack of extensive far-field measurements in the field makes it difficult to determine if this divergence is a result of error propagation during our data collection or of a possible regional tilt in the DEM from an inaccurate spatial baseline (distance between the two satellite positions) which can result from inaccurate or insufficient GCP registration (see Chapter 2 section 6).

Three of the nine scarps were eliminated from comparison with the DEM. Scarp 1 was selected based on the logistics of another field team with which we traveled. Upon our return from the field, we discovered that this hillslope was in radar shadow (a zone of no data) in the DEM. Due to the absence of the corner cube reflector while profiling scarp 2, we were unable to successfully measure the crest and upper slopes of the scarp. Although the field assistant substituted for the reflector, return signals to the laser range finder were weak over greater distances. The incomplete profile rendered the

Figure 4.4 Comparison of field profiles (red) with DEM profiles (blue). All profiles for scarps 3-8 are compared with corresponding DEM profiles. Plot axes are based on the DEM values in meters.

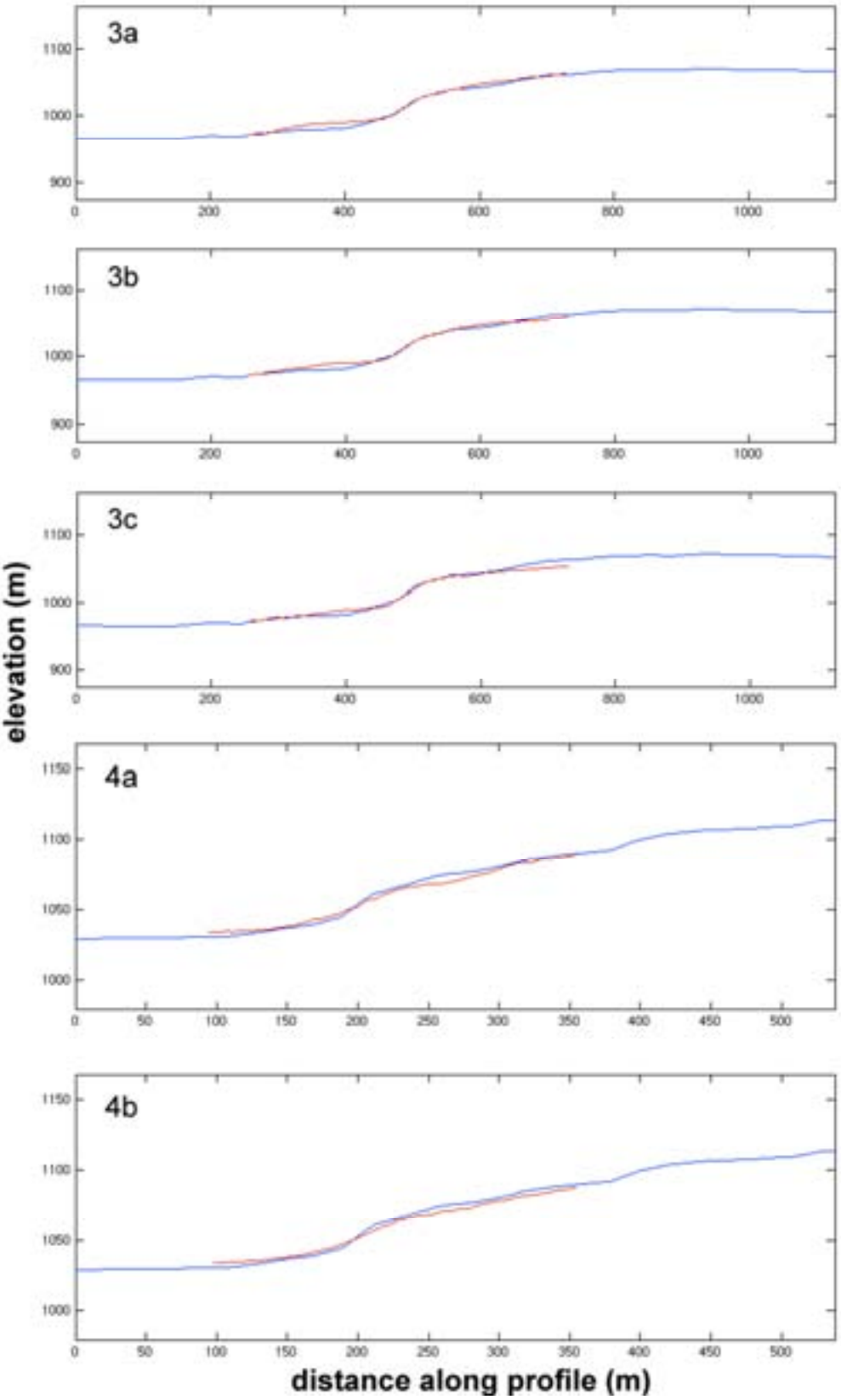
3a
3b
3c
4a
4b
elevation (m)
distance along profile (m)

Figure 4.4 (Continued)

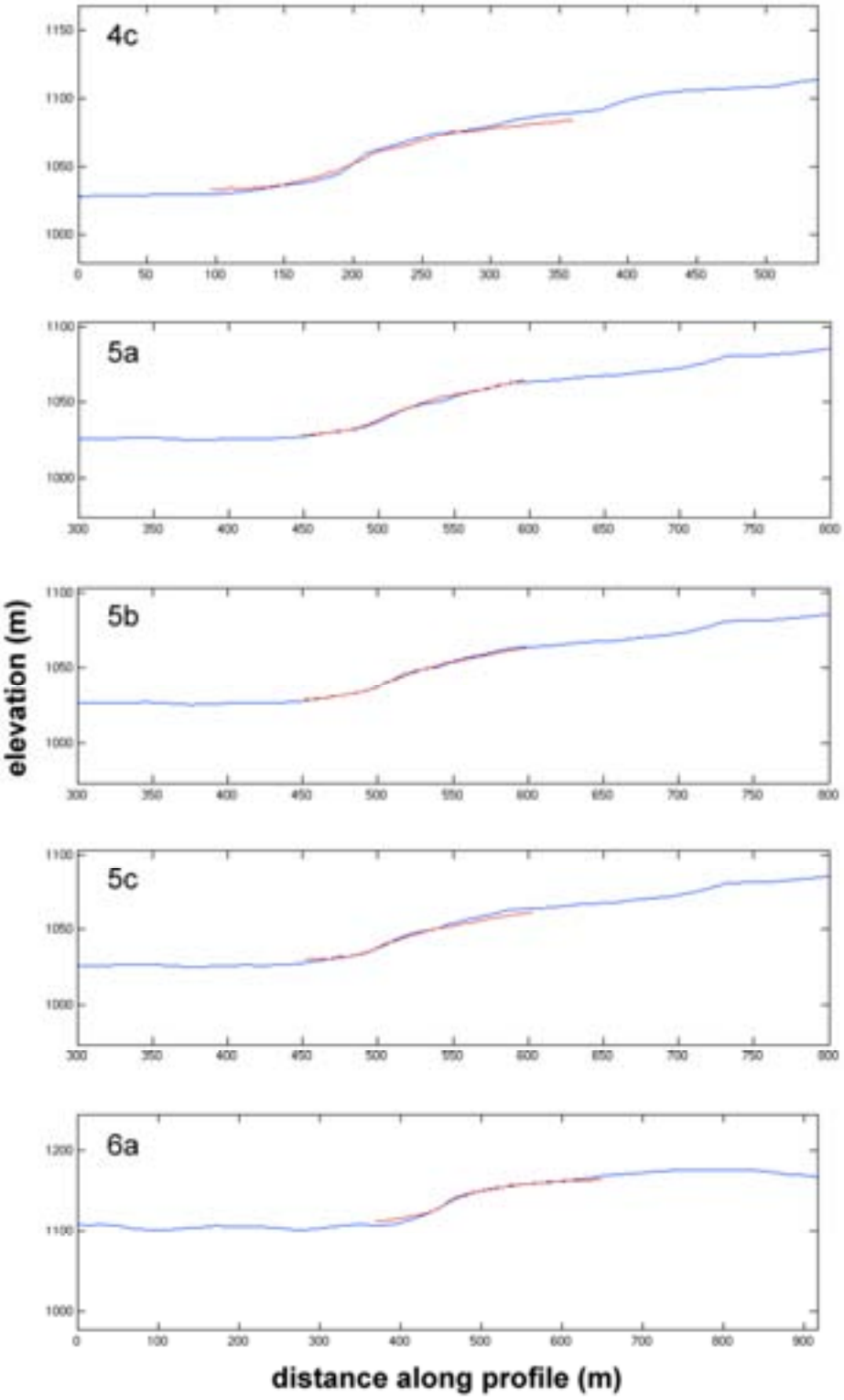

Figure 4.4 (Continued)

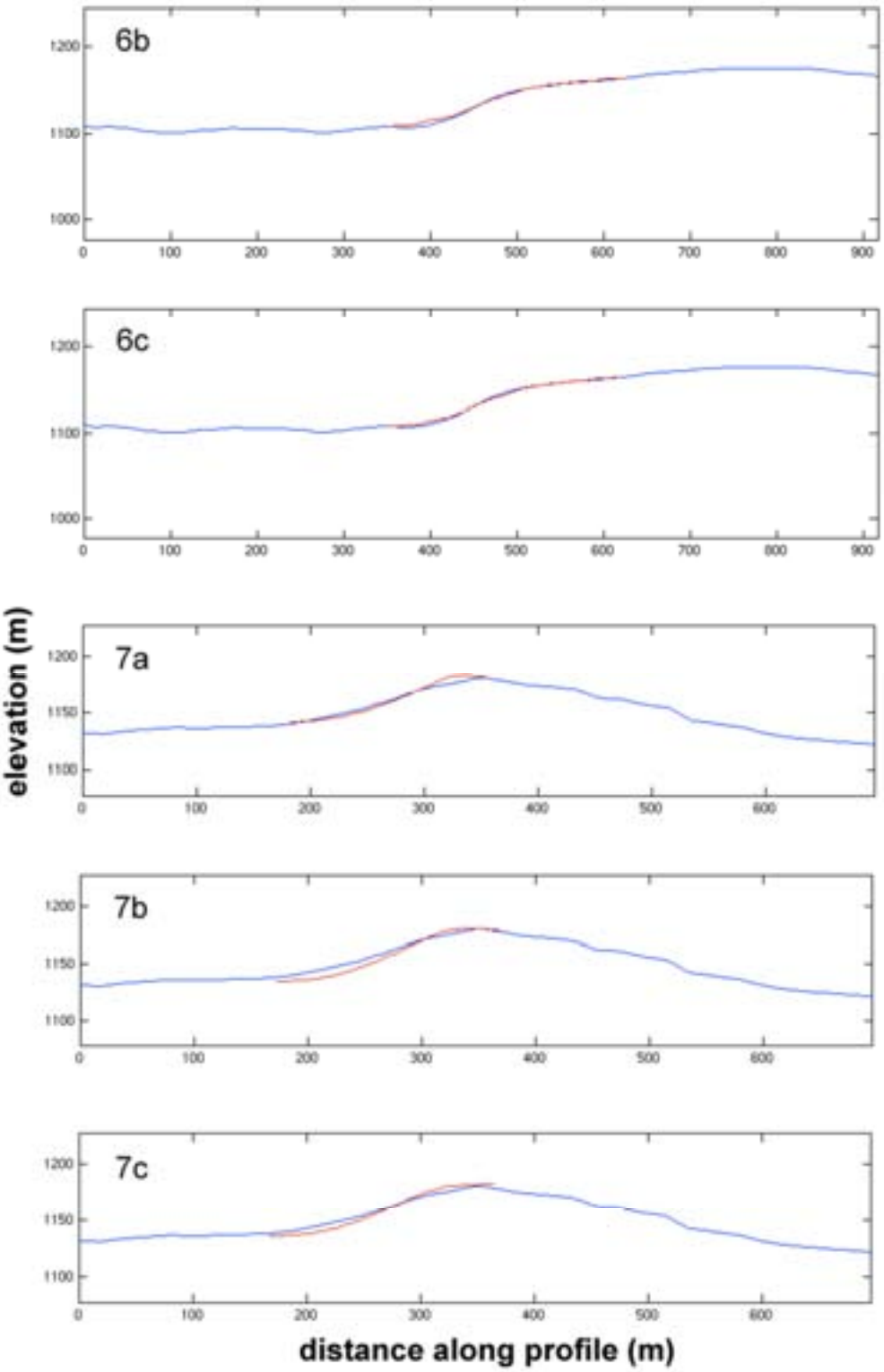

Figure 4.4 (Continued)

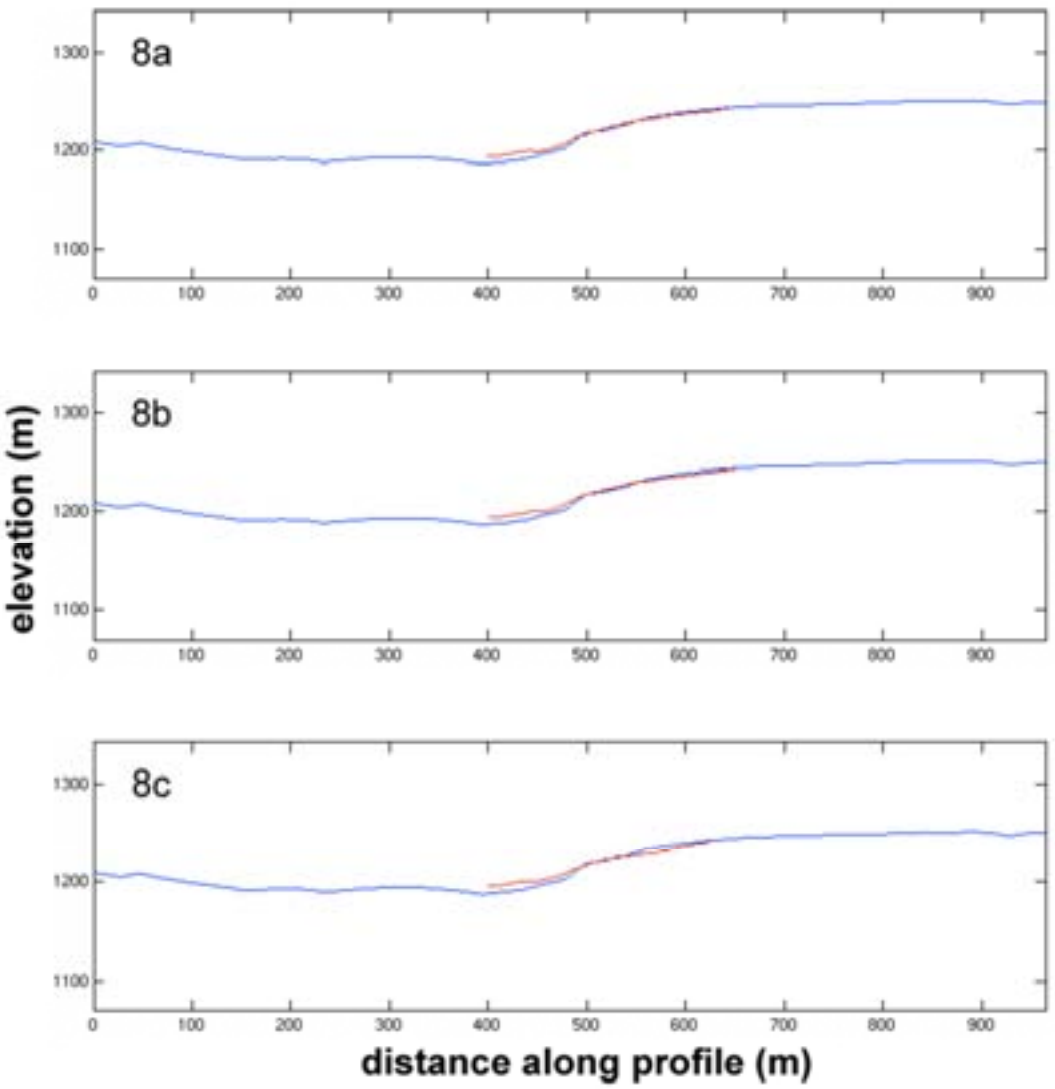

DEM matching of regional slopes inconclusive. The last scarp profiled was scarp 9 south of Antofagasta. The offset on this face was less than 1 meter and could not be resolved in the DEM.

The field profiles were plotted against their corresponding DEM profiles with an emphasis on aligning the scarp faces. To quantify the agreement between the ground measurements and the DEM, we calculated the mean difference (DEM minus field profile) and standard deviation for each pair. These values are listed in Table 4.2.

Table 4.2 Comparison of DEM to Field Profiles

Profile	Mean μ (m)	Standard Deviation σ (m)
3a	-2.5	3.3
3b	-1.6	3.4
3c	0.9	4.1
4a	-1.5	2.7
4b	-1.2	2.7
4c	-1.1	2.7
5a	-0.7	0.7
5b	0.3	0.7
5c	0.9	1.5
6a	-0.9	2.4
6b	-0.9	1.8
6c	-0.3	1.6
7a	-0.2	2.5
7b	-0.5	3.7
7c	0.2	3.4
8a	-2.2	3.2
8b	-1.8	3.4
8c	-1.4	4.3

Ultimately the agreement between the profiles and the DEM is good considering the relative vertical accuracy of the DEM is 2-3 meters. The mean

difference was as small as 0.2 and -0.2 meters on profiles 7c and 7a respectively, and was highest on profile 3a at -2.5 meters. The range of σ in Table 4.2 is from 0.7 to 4.3 meters. Typical deviations between the DEM and the field measurements are consistent with the relative vertical uncertainty in the DEM. These numbers suggest it is statistically reasonable to extract profiles from the DEM to represent the shape of scarps with offsets greater than ten meters.

Many of the smaller wavelength details recorded in the field profiles did not appear in the DEM profiles. This was not unexpected for a dataset with 20-meter horizontal postings and a relative vertical resolution of 2-3 meters. The main shortcoming of the field profiles was the limited extent of the far-field slopes. Additionally, the lateral spacing between parallel profiles in a single location was on the order of one to two pixels on the DEM. A single representative transect was extracted from the DEM and compared to all members of the field profile set.

4.4 *Inverse Diffusion Scarp Modeling*

Some of the earliest publications on scarp evolution and morphology began with Davis (1899) who claimed that erosion attenuates the topographic signal of a hillslope, and Penck (1924) who argued that rates of uplift determined the shape of a hillslope. In essence, both were correct, but incomplete. Landscape evolution results from the combination of constructional and erosional processes at work on the Earth's surface. A common constructional process occurs when a fault ruptures the surface during an earthquake and

creates a topographic discontinuity. Erosion of that discontinuity can result from diffusional processes such as rain splash and creep, or advective processes such as fluvial incision, fluvial transport, eolian transport, and landsliding.

Wallace (1977) was the first to give detailed temporal observations on the evolution of scarp morphology. Researchers have determined that a linear diffusion model is a good approximation for simplified down-slope creep on a scarp in non-cohesive materials in semi-arid and arid climates (Arrowsmith et al., 1996; Hanks and Wallace, 1985; Hanks et al., 1984; Nash, 1980, 1984).

4.4.1 *The Diffusion Equation*

An elevation profile *u(x,t)* [m] subject to a diffusive process with mass diffusivity *k* [m^2/yr] must obey the diffusion equation:

$$\frac{\partial u}{\partial t} = k \frac{\partial^2 u}{\partial x^2}. \tag{1}$$

The solution to this equation is

$$u(x,t) = a \cdot erf\left(\frac{x}{2\sqrt{kt}}\right) + bx + C. \tag{2}$$

2a is the scarp offset, *b* is the regional slope, *kt* is related to the amount of material that has been diffused at time *t*, *C* is a constant elevation offset, and *erf* is the error function (Hanks, 2000). If we consider a fault scarp to be a topographic step function (see Figure 4.5), and allow diffusion to act on it over

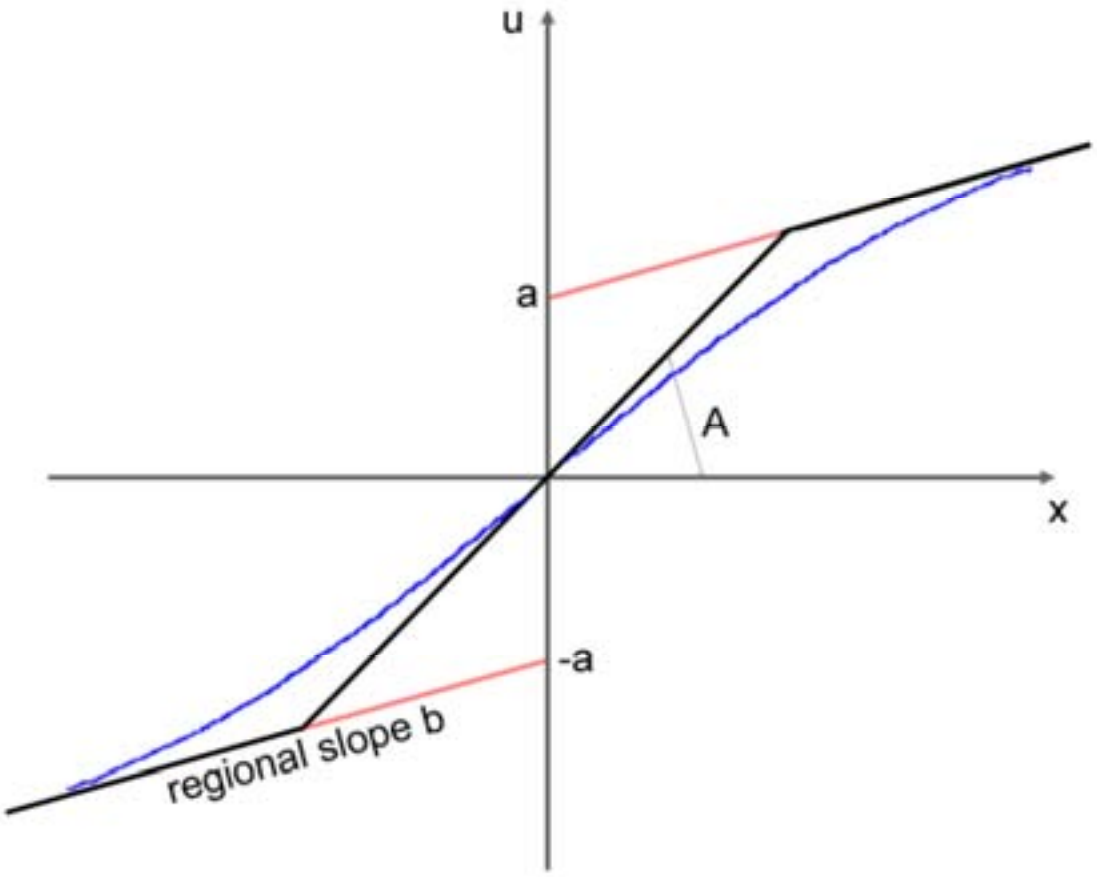

Figure 4.5 Fault scarp schematic. The black line represents the initial scarp profile. The blue line represents a degraded scarp profile. *A* is the maximum slope of the scarp face.

time, then material from the top of the scarp will be transported to the base of the scarp. The process dampens the topographic signal and smoothing of the profile resembles the error function.

4.4.2 *The Gaussian Slope Distribution*

The derivative of the profile across the scarp at fixed *t* will thus be Gaussian:

$$\frac{\partial u}{\partial x} = \frac{a}{\sqrt{\pi kt}} e^{\frac{-x^2}{4kt}} + b \,. \tag{3}$$

This is simply the slope of the profile. Gaussian curves can be fit to the finite difference slope distributions of field profiles to extract characteristic parameters that define the shape of the corresponding error functions. The amplitude of the Gaussian, *A* is measured from the base to the peak of the curve. It is the maximum slope on the scarp and is related to scarp height *2a* by:

$$A = \frac{a}{\sqrt{\pi kt}} \,. \tag{4}$$

Full width half max (*fwhm*) is the width of the curve at half the maximum value from base to peak:

$$fwhm = 2.35\sqrt{2kt} \,. \tag{5}$$

The offset from the base of the Gaussian to the x-axis is the regional slope on the scarp *b.* On the Gaussian curve, the mean is located at the peak. This corresponds to the inflection point on the error function, or the scarp face.

Figure 4.6 shows how the various parameters relate to characteristics of the scarp profile and how the Gaussian slope distribution spatially corresponds to the scarp profile.

4.4.3 *Single-Event and Cumulative Scarps*

Avouac and Peltzer (1993) applied a Gaussian model from Avouac (1993) to profiles of single-event scarps in unconsolidated fanglomerates in the southwestern Tarim basin to make mass diffusivity estimates for the area. The climate there is arid and the scarps were approximately 4-8 meters in height. Their model only considered surface processes that locally conserve mass, so they eliminated the effects of fluvial transport or eolian erosion and/or deposition. This is a good approximation of the environment we observed in northern Chile. However, we are unable to identify single-event scarps with any confidence in the DEM. As a result, all of the scarps in this study are likely to be cumulative, multiple-event fault scarps.

The majority of scarp diffusion modeling studies address single-event ruptures of relatively young age (< 100 ka). The majority of fault scarps however, are a result of multiple earthquakes. Diffusion modeling of cumulative or composite fault scarps introduces additional complexity and uncertainty in age or diffusivity estimation (Avouac, 1993; Andrews and Hanks, 1985; Mayer, 1984). Treatment of composite scarps as large single-event structures results in larger morphology-derived age estimate errors (Mayer, 1984). Andrews and Hanks (1985) propose it is a viable dating technique if parameters such as the time for a free face to evolve into angle of repose and variation of diffusivity

Figure 4.6 Parameter relationship between Gaussian and Error Function.

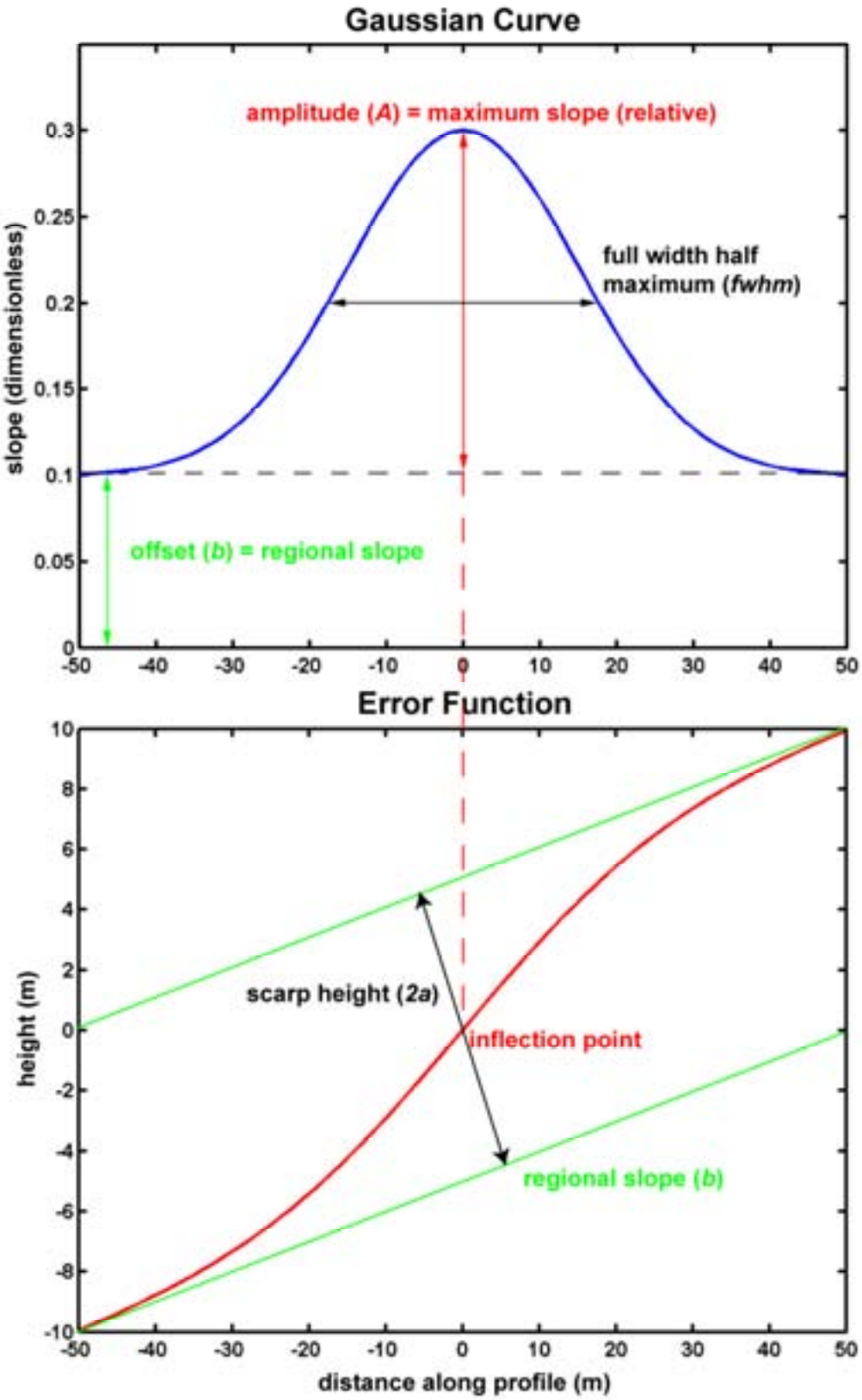
Gaussian Curve
amplitude (A) = maximum slope (relative)
full width half maximum (fwhm)
offset (b) = regional slope
slope (dimensionless)
0.3
0.25
0.2
0.15
0.1
0.05
0
-50
-40
-30
-20
-10
0
10
20
30
40
50
Error Function
scarp height (2a)
inflection point
regional slope (b)
height (m)
10
8
6
4
2
0
-2
-4
-6
-8
-10
distance along profile (m)

with climate and material could be determined. Carretier et al. (2002) show that only with sub-meter sampling of scarp profiles is it possible to deconstruct the multiple discrete offset events. We were unable to identify single events on the scarps in this study, so we do not attempt to determine their absolute age or diffusion rates. Instead, we adopt a simplified treatment of all structures as single-event scarps assuming the climate (Hoke, 2006) and the bedrock material (Allmendinger and González, 2009) is consistent throughout the study region in the Coastal Cordillera. We conduct a comparative study of scarp morphology and apply inverse diffusion modeling to quantify scarp profiles and identify distinct populations in the sample.

4.5 *Results*

All of the parameters for the Gaussian fits of the finite difference slopes of the field profiles and their corresponding error function fits with the field and DEM profiles were calculated. The results were typically good, although there were some notable discrepancies for some profiles. Figure 4.7 shows examples of the range of quality in our matches. Profile 6c is representative of the best fits. Profile 3b is an example of an average fit, and among the worst fits is profile 4c. Despite being the worst fit, 4c still shows a reasonable agreement with the error function. Based on our confidence in the DEM to give a representative profile of a scarp face, we collected 35 additional profiles of 35 scarps from the DEM. The locations of these scarps and the original 8 from the field (excluding scarp 9 in Antofagasta) are mapped in Figure 4.8. The scarps we measured in the field were renamed A-H (1-8) and the new DEM profiles are numbered 1-35.

Figure 4.7 Gaussian slope distribution fits and corresponding error function profiles: a) shows a best-fit case, profile 6c; b) shows an average quality fit, profile 3b; c) shows the worst fit, profile 4c.

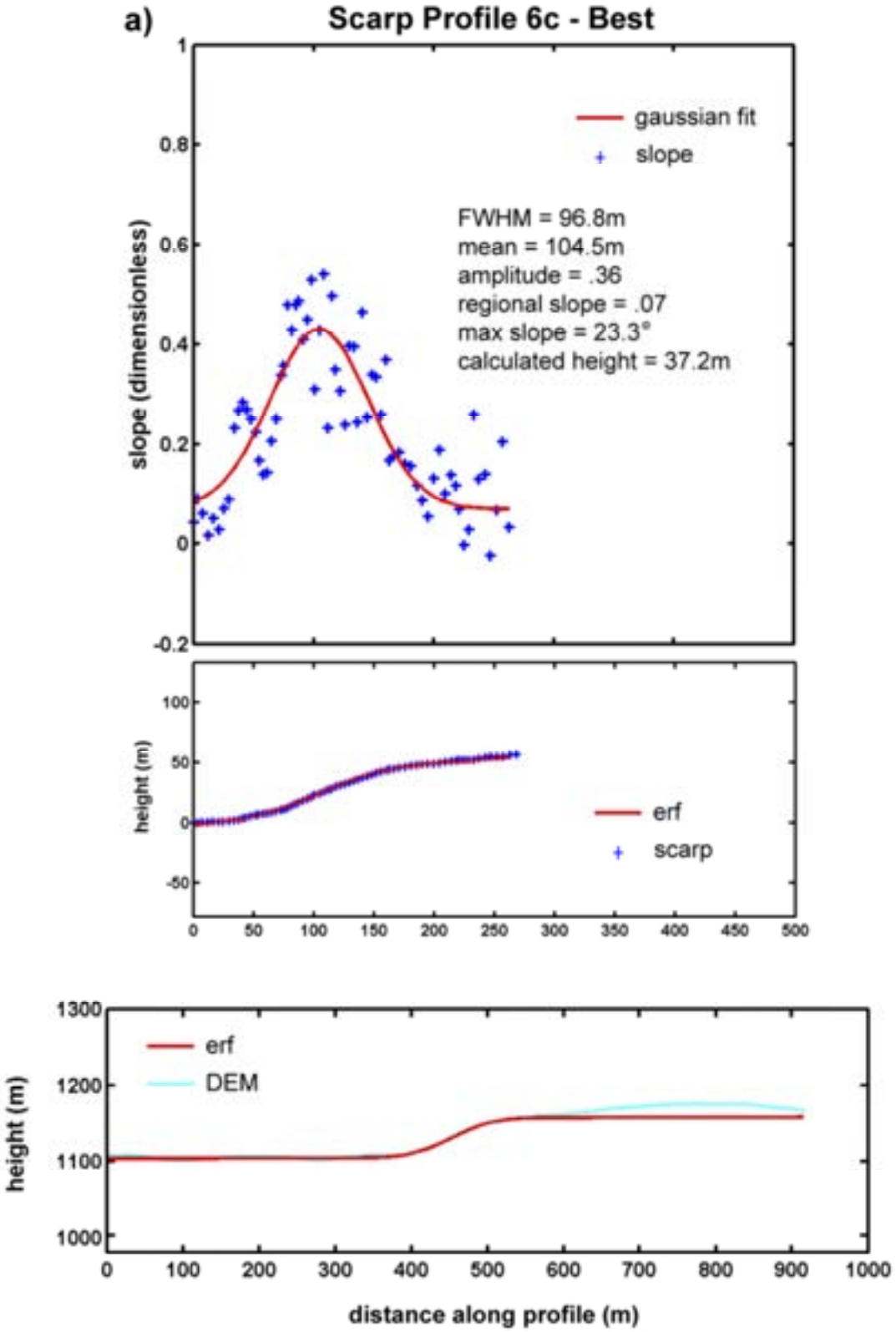
a)
Scarp Profile 6c - Best
gaussian fit
slope
FWHM = 96.8m
mean = 104.5m
amplitude = .36
regional slope = .07
max slope = 23.3°
calculated height = 37.2m
slope (dimensionless)
height (m)
erf
scarp
erf
DEM
height (m)
distance along profile (m)

Figure 4.7 (Continued)

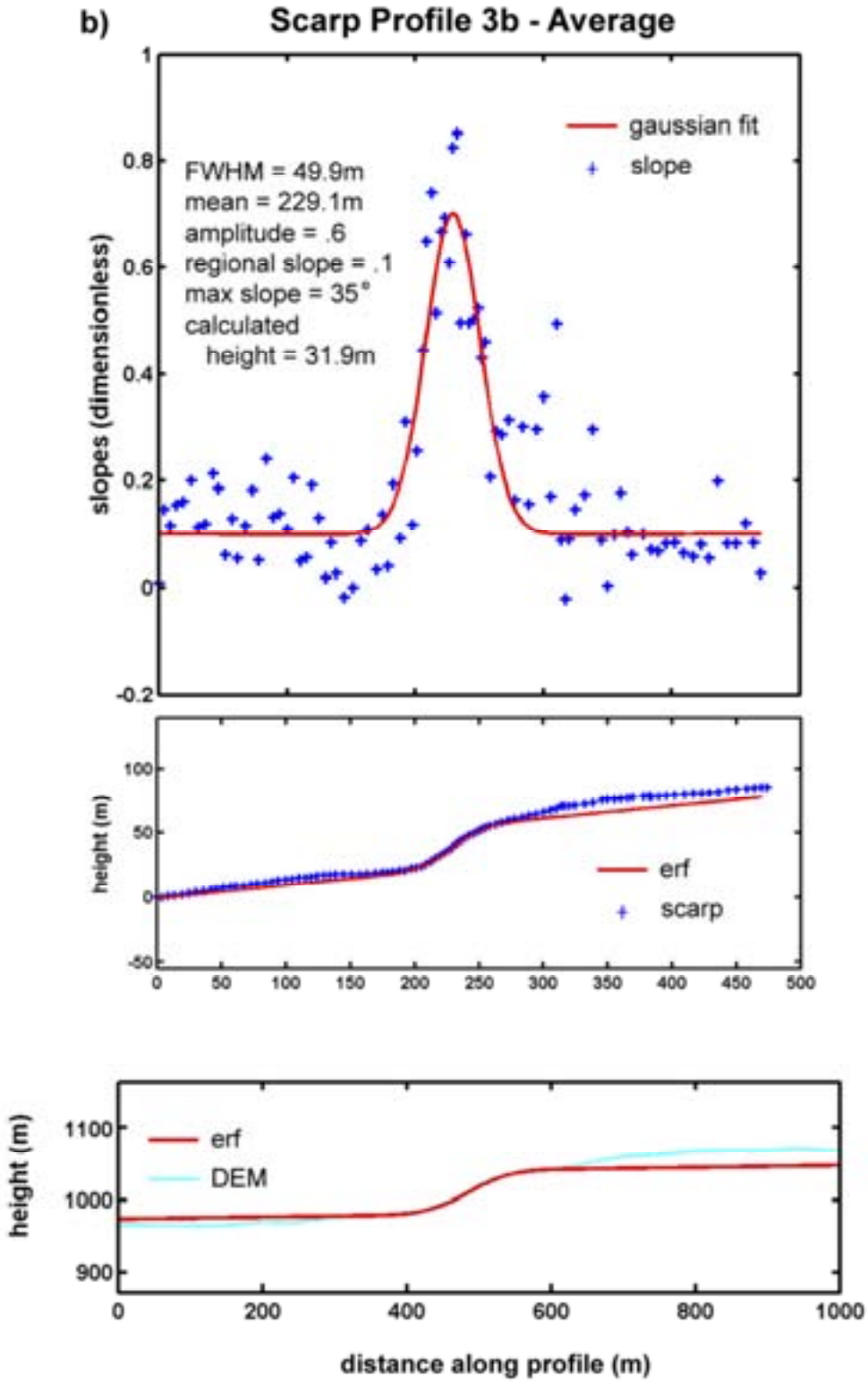

Figure 4.7 (Continued)

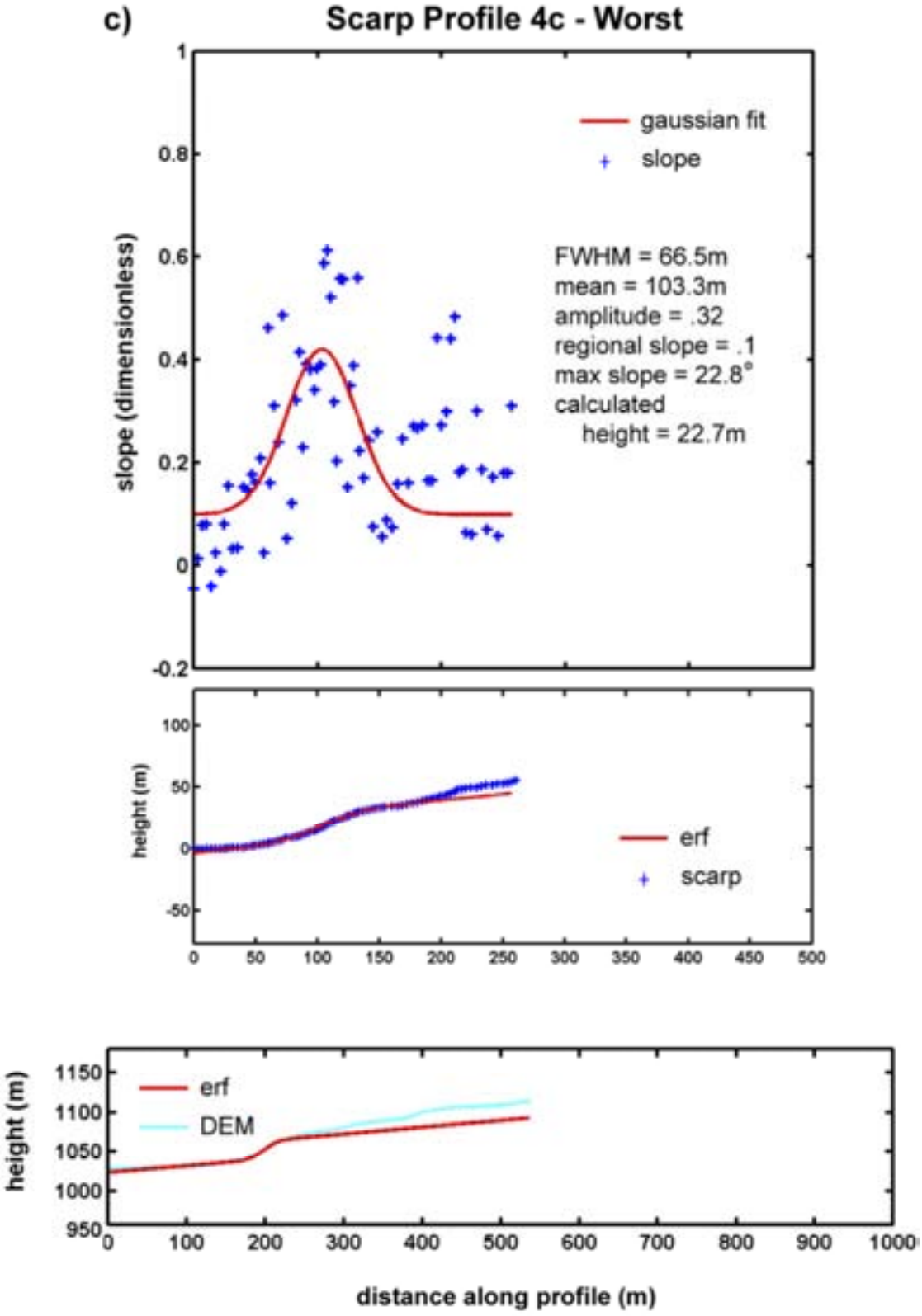

Figure 4.8 Location map for field-measured and DEM-extracted profiles. Field profiles are renamed A-H (corresponding to field profiles 1-8) and DEM-only profiles are numbered 1-35.

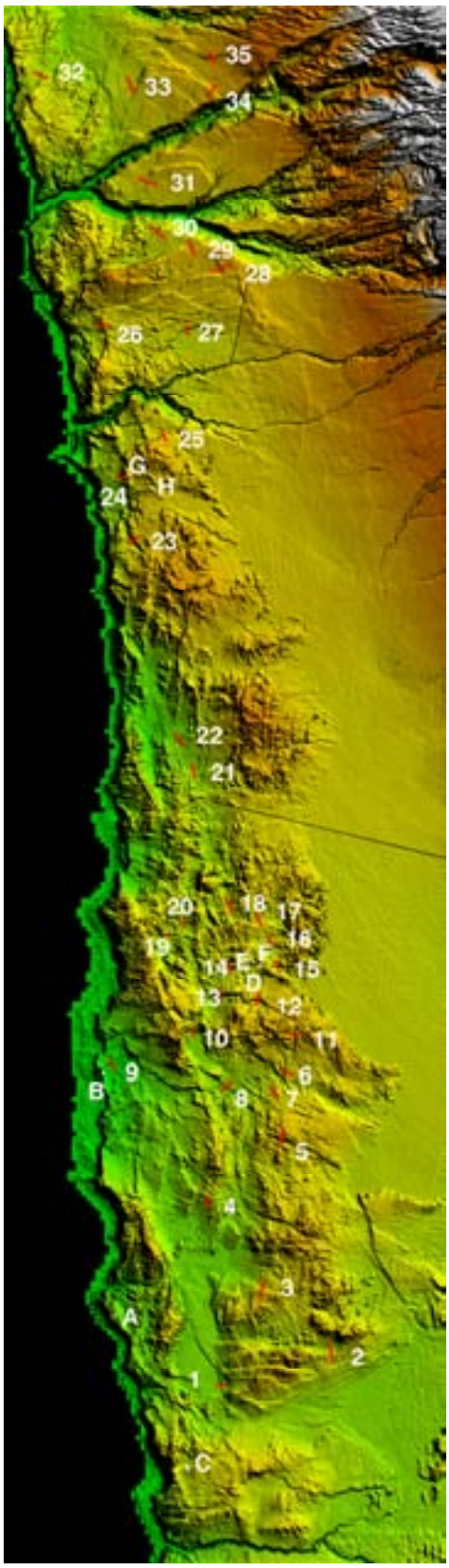
35
32
33
34
31
30
29
28
26
27
25
G
H
24
23
22
21
20
18
17
16
19
14
E
F
15
D
13
12
10
11
9
6
B
8
7
5
4
3
A
2
1
C

We included the 35 DEM profiles in our computations. The motivation for performing this analysis on the scarps is to extract *a* and *fwhm* parameters, which characterize each profile. We plot *a* against *fwhm* to determine if there is a relationship between the scarp height and the erosional state of the scarp (how much material has diffused). The scarp morphology essentially gives us a relative scarp age because the shape of the scarp profile only varies with time if we assume a constant diffusivity *k* for the region. This is reasonable considering climate does not vary with latitude in the study area (Hoke, 2006) and the profiles lie within the Coastal Cordillera. Therefore we can compare relative scarp morphology within our sample. Table 4.3 lists all of the parameters determined for each profile, its corresponding DEM profile, and the additional 35 DEM profiles.

On the plot of scarp height (*2a*) versus *fwhm* (Figure 4.9) there is one distinct trend at 19º (solid line) and another tentative trend at 30º (dashed line) that describe two possible groups of maximum scarp slopes within the profile sampling. Scarps of a given height that fall on the solid line will have a wider scarp profile than scarps of the same height that plot on the dashed line. This could mean that the solid line scarps are older, less active, or compositionally different, although the last possibility is the least likely given the spatial distribution of the sampled scarps. It is interesting to note that there are few scarps above the dashed line and many below the solid line. The angle of repose for unconsolidated colluvium is generally between 30º and 35º (Carson and Kirby, 1972), which explains the scarcity of points above the dashed line. The population of points below the solid line represents scarps that all lie in the eastern part of the Coastal Cordillera, or at least, not near the coast.

Table 4.3 Parameters *fwhm*, relative maximum slope *A*, height, and regional slope *b*, are listed for field profiles 3-9 (renamed C-I), their corresponding DEM profile if available, and the additional 35 DEM profiles (numbered 1-35).

Table 4.3 Gaussian Parameters for Field and DEM Profiles

Profile	fwhm (m)	Max Slope Relative A (º)	Height (m)	Regional Slope b (º)
3a (C)	52.1	30.5	32.8	5.1
3b (C)	49.9	31.0	31.9	5.7
3c (C)	55	31.8	36.4	5.7
4a (D)	78.7	17.7	26.9	5.7
4b (D)	53.2	18.3	18.7	6.8
4c (D)	66.5	17.7	22.7	5.7
5a (E)	42.1	16.7	13.5	8.5
5b (E)	39.2	16.7	12.5	8.5
5c (E)	32.8	17.2	10.8	6.8
6a (F)	40.9	29.7	24.9	5.1
6b (F)	98.2	19.8	37.7	4.0
6c (F)	96.8	19.8	37.2	4.0
7a (G)	87	26.6	46.4	-2.3
7b (G)	87.9	27.5	48.8	-1.1
7c (G)	91.3	23.3	41.9	1.7
8a (H)	35.3	17.7	12.0	9.1
8b (H)	35.7	18.3	12.6	8.0
8c (H)	55.1	17.7	18.8	4.6
9a (I)	6.9	14.0	1.8	5.1
9b (I)	9.2	10.2	1.8	5.1
DEM Profile				
3 (C)	108.3	27.6	60.3	0.8
4 (D)	33.75	32.3	22.7	5.0
5 (E)	99.78	17.6	33.8	1.8
6 (F)	101.2	26.1	52.8	0.1
7 (G)	113.2	19.3	42.3	0.4
8 (H)	112	22.0	48.4	0.9
DEM-Only Profile				
1	246.7	9.2	42.6	0.1
2	434.8	30.4	271.8	-4.2
3	556.7	17.0	181.1	0.4
4	160.3	15.2	46.5	0.0
5	168.7	19.3	63.0	0.8
6	301.5	11.4	64.6	-0.1
7	335.7	14.6	93.1	0.1
8	133.1	33.7	94.8	0.2
9	172.3	17.5	57.9	-0.3
10	303.3	14.6	84.4	2.3
11	117.2	24.3	56.4	0.2
12	318.6	17.8	109.4	-2.1
13	480.6	17.6	163.0	-2.3
14	421.9	16.5	133.2	-1.9
15	165.4	11.7	36.5	0.1
16	197.1	20.1	76.9	-0.2
17	617.9	12.7	148.3	-1.4
18	211.9	19.0	77.8	0.1

Table 4.3 (Continued)

Profile	fwhm (m)	Max Slope Relative A (º)	Height (m)	Regional Slope b (º)
19	109.5	24.4	52.9	0.9
20	161.7	15.4	47.4	0.6
21	283.5	10.7	57.2	-0.7
22	231	15.1	66.5	1.3
23	311.5	28.4	179.8	1.3
24	241.9	32.2	162.6	3.2
25	514.6	19.4	193.8	-1.1
26	143.2	27.1	78.1	3.0
27	282.9	13.7	73.6	0.1
28	244.7	9.6	44.1	0.5
29	492.1	19.4	185.3	0.3
30	315.3	12.2	72.6	0.0
31	470.4	3.8	33.6	0.1
32	79.65	24.6	38.8	-0.1
33	232.6	11.3	49.4	0.5
34	226	11.5	49.2	-0.1
35	416	8.2	63.9	-0.1

Figure 4.9 Scarp height versus width. Height is plotted against *fwhm* for all scarps in the study. The solid gray line represents scarp face slopes of 19° and the dashed gray line has a slope of 30°.

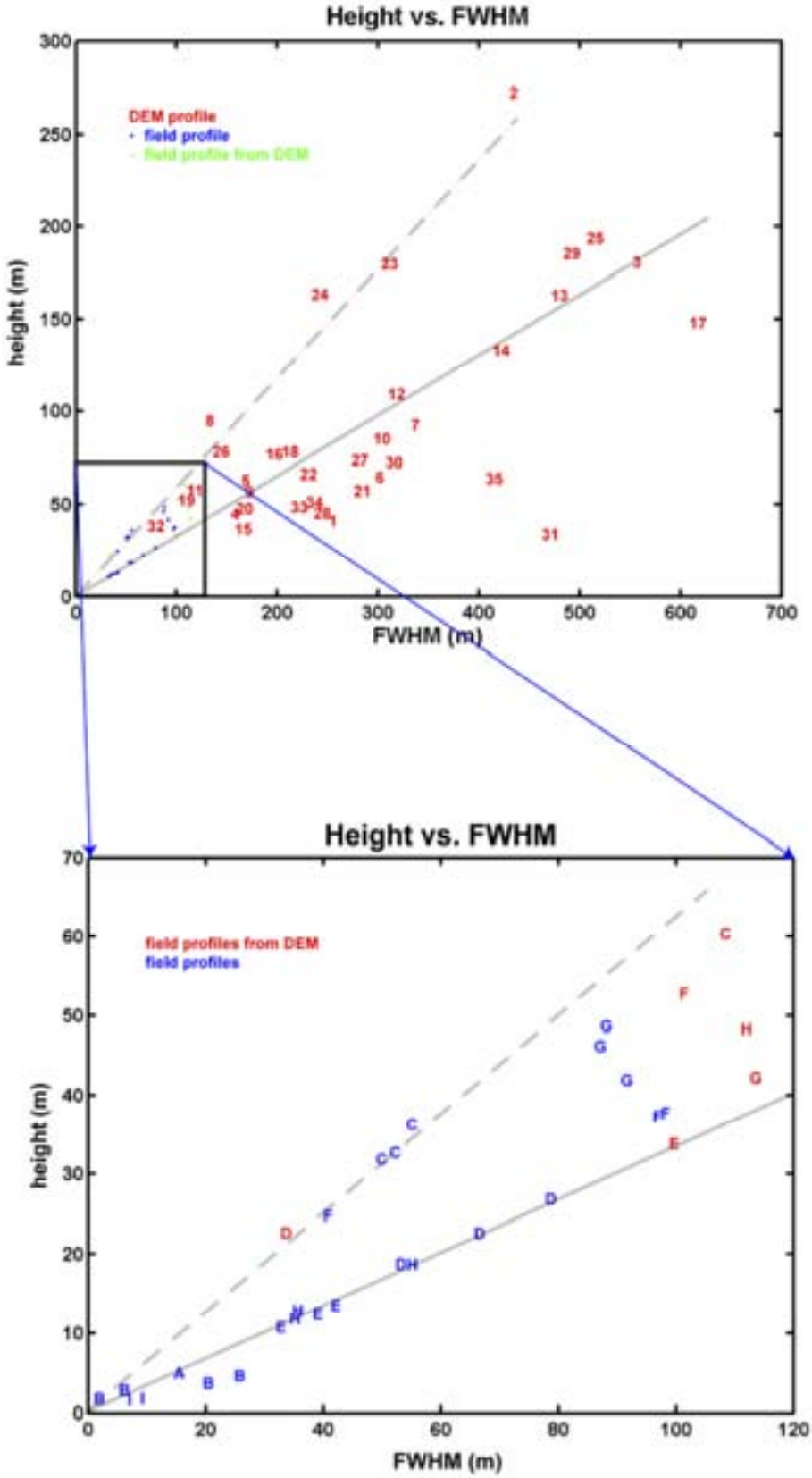
Height vs. FWHM
DEM profile
field profile
field profile from DEM
height (m)
FWHM (m)
Height vs. FWHM
field profiles from DEM
field profiles
height (m)
FWHM (m)

Those points on or near the dashed line are mostly near the coast, but not all (most notably DEM scarp 2).

One could infer that the scarps near the coast are younger than the inland scarps, but recall the gypcrete encountered in the field. Loveless et al. (2005) describe it as a ubiquitous layer near the Salar Grande region (near DEM scarp 1), which has preserved tens of thousands of cracks in the surface. It is possible that a scarp near the coast is approximately the same age as its inland counterpart, but its surface was preserved by the formation of gypcrete after the initial collapse of the scarp's free face. The competent and cohesive gypcrete layer will certainly degrade much slower than the typical unconsolidated colluvium draping the scarps to the east, thus affecting the diffusivity *k* of the scarp face. This could account for the two populations of fault scarps in Figure 4.9 if all other factors are equal.

We have measurements for *kt* (based on *fwhm*), but no constraints on either *k* or *t* for our scarps, thus *k* and *t* are degenerate. Loveless et al. (2005) point out the diffusion constants for the Atacama Desert are unknown. The ages of the scarps in this study are poorly constrained, although field work by Allemendinger and González (2009) and Allmendinger et al. (2005) on major E-W reverse faults in the north Chilean forearc supports activity on these structures since at least 6 Ma to present. On the Salar del Carmen segment of the Atacama Fault System, González et al. (2006) determined late Pleistocene activity in fault scarps that disrupt alluvial fan sediments. It is possible that continued progress in determination of *t* on fault scarps in the

forearc could constrain *k* and give us a first-order approximation for diffusivity in the Atacama Desert.

4.6 *Conclusions*

Our comparison of field measurements of scarp profiles in the north Chilean forearc with corresponding DEM profiles validates the relative vertical accuracy of the DEM at 2-3 meters. Disagreement between the field measurements and the DEM increased along the far-field slopes, which could result from the lack of longer profile sampling, a possible regional tilt in the DEM from inaccurate spatial baseline calculations, or error propagation from the data collection method in the field. It is statistically reasonable, based on the good agreement at the scarp face, that extraction of scarp profiles greater than 10 meters in offset from the DEM for our analysis is valid. We applied an inverse diffusion model to our scarp sample in order to measure diffusion parameters that completely define the scarp morphology. We found that there are two populations of fault scarp morphologies that correlate to the proximity of a scarp to the coast. The more degraded scarps were located inland from the coast and the steeper scarps mostly bordered the coast on the western front of the Coastal Cordillera. Scarps near the coast are subject to inundation by a thick coastal fog, which delivers moisture to the area and forms gypcrete layers on the surface. The gypcrete preserves scarp faces and degrades much slower than the typical colluvium that mantles most of the scarps in the study area. Although our analysis of scarps from the DEM could not provide information on the age of the faulting, it was able to discern these two settings for scarp diffusion in the Coastal Cordillera of northern Chile. This illustrates

the utility of the DEM for morphological analysis over a large region at a 10-meter vertical scale. Researchers have constrained ages of displacement on other fault scarps in the region which could lead to a determination of a diffusivity constant for the Atacama Desert.

REFERENCES

Allmendinger, R. W., González, G., Yu, J., Hoke, G., Isacks, B., 2005, Trench-parallel shortening in the Northern Chilean Forearc: Tectonic and climatic implications, Geological Society of America Bulletin, 117, 89-104.

Allmendinger, R. W., and González, G., 2009, Neogene to Quaternary tectonics of the coastal Cordillera, northern Chile, Tectonophysics, doi:10.1016/j.tecto.2009.04.019

Andrews, D. J., and Hanks, T. C., 1985, Scarp degraded by linear diffusion: Inverse solution for age.: Journal of Geophysical Research, v. 90, 10,193–10,208.

Arrowsmith, J.R., Pollard, D.D., Rhodes, D.D., 1996, Hillslope development in areas of active tectonics.: Journal of Geophysical Research, v. 101, 6255-6275.

Avouac, J.-P., 1993, Analysis of Scarp Profiles: Evaluation of Errors in Morphologic Dating.: Journal of Geophysical Research, v. 98, 6745-6754.

Avouac, J.-P., and Peltzer, G., 1993, Active tectonics in southern Xingiang, China: Analysis of terrace riser and normal fault scarp degradation along the Hotan-Qira fault system.: Journal of Geophysical Research, v. 98, 21773-21807.

Carretier, S., Ritz, J.-F., Jackson, J., and Bayasgalan, A., 2002, Morphological dating of cumulative reverse fault scarps: examples from the Gurvan Bogd fault system, Mongolia.: Geophysical Journal International, v. 148, 256-277.

Carson, M.A., and Kirby, M.J., 1972, Hillslope, Form and Process, Cambridge, pp. 475.

Davis, W.M., 1899, The geographical cycle, Geographical Journal, v. 14, 481-504.

González, G., Dunai, T., Carrizo, D., Allmendinger, R., 2006, Young displacements on the Atacama Fault System, northern Chile from field observations and cosmogenic 21Ne concentrations. Tectonics 25, TC3006 10.1029/2005TC001846.

Hanks, T.C., 2000, The Age of Scarplike Landforms From Diffusion-Equation Analysis, Noller, J.S., Sowers, J.M., and Lettis, W.R., eds., Quaternary geochronology: Methods and applications.: Washington D.C., American Geophysical Union, 313-338.

Hanks, T.C., Bucknam, R.C., Lajoie, K.R., and Wallace, R.E., 1984, Modification of wave-cut and faulting-controlled landforms, Journal of Geophysical Research, v. 89, 5771-5790.

Hanks, T.C., and Wallace, R.E., 1985, Morphological analysis of the lake Lahontan shoreline and beachfront fault scarps, Persching County, Nevada, Bulletin of the Seismological Society of America, v. 75, 835-846.

Hoke, G.D., 2006, The Influence of Climate and Tectonics on the Geomorphology of the Western Slope of the Central Andes, Chile and Peru, pp. 296, Ph.D. dissertation, Cornell University, Ithaca, New York.

Loveless, J.P., Hoke, G.D., Allmendinger, R.W., González, G., Isacks, B.L., and Carrizo, D.A., 2005, Pervasive cracking of the northern Chilean Coastal Cordillera: New evidence for forearc extension, Geology, v. 33, 973-976.

Mayer, L., 1984, Dating quaternary fault scarps formed in alluvium using morphologic parameters, Quaternary Research, v. 22, 300-313.

Nash, D.B., 1980, Morphological dating of degraded normal fault scarps, Journal of Geology, v. 88, 353-360.

—, 1984, Morphological dating of fluvial terrace scarps and fault scarps near West Yellowstone, Montana, Geological Society of America Bulletin, v. 95, 1413-1424.

Penck, W., 1924, Morphological Analysis of Landforms (translated by Ezech and Boswell in 1953). London, MacMillian, pp. 429.

Rech, J.A., Quade, J., and Hart, W.S., 2003, Isotopic evidence for the source of Ca and S in soil gypsum, anhydrite and calcite in the Atacama Desert, Chile, Geochimica et Cosmochimica Acta, v. 67, 575-586.

Wallace, R.E., 1977, Profiles and ages of young fault scarps, north-central Nevada, Geological Society of America Bulletin, v. 88, 1267-1281.

CHAPTER 5

CONCLUSIONS

The 20-meter INSAR-derived DEM of the north Chilean forearc is the main contribution of this dissertation. It is a high-resolution, comprehensive (99.1% complete) digital topographic dataset that provides an overview of the regional morphology *and* detail enough to examine the morphology down to 2-3 meters vertical resolution. We mapped the conspicuous patterns of faulting on the DEM leading to ground-truth measurements of scarp profiles in the field. Agreement between the field profiles and the DEM profiles were surprisingly good. This helps to validate the utility of the DEM as a reliable topographic representation of the forearc.

We found a regional difference in scarp morphologies based on profiles extracted from the DEM which we attribute to the presence of gypcrete armoring the scarps nearest the coast. The dataset has been employed by a variety of other researchers for atmospheric modeling, gravity anomaly modeling, and basin evolution modeling.

Since the DEM was first generated, other high-resolution dataset have been released. The co-registration and ground-truthing of the northern Chile DEM could be further improved with the newer Landsat ETM and NASA SRTM DEM to better constrain the horizontal and vertical accuracies as well as improve mosaicking across radar scenes.